

**Perovskite Oxide Combined With Nitrogen-Doped Carbon Nanotubes As  
Bifunctional Catalyst for Rechargeable Zinc-Air Batteries**

by

Vugar Ismayilov

A thesis

presented to the University of Waterloo

in fulfillment of the

thesis requirement for the degree of

Master of Applied Science

in

Chemical Engineering - Nanotechnology

Waterloo, Ontario, Canada, 2014

© Vugar Ismayilov 2014

## **Author's Declaration**

I hereby declare that I am the sole author of this thesis. This is a true copy of the thesis, including any required final revisions, as accepted by my examiners.

I understand that my thesis may be made electronically available to the public.

## Abstract

Zinc air batteries are among the most promising energy storage devices due to their high energy density, low cost and environmental friendliness. The low mass and cost of zinc air batteries is a result of traditional active materials replacement with a thin gas diffusion layer which allows the battery to use the oxygen directly from the air. Despite the environmental and electronic advantages offered by this system, challenges related to drying the electrolyte and catalyst, determining a high activity bifunctional catalyst, and ensuring durability of the gas diffusion layer need to be optimized during the fabrication of rechargeable zinc-air batteries. To date, platinum on carbon (Pt/C) provides the best electrochemical catalytic activity in acidic and alkaline electrolytes. However, the difficult acquisition and high cost of this catalyst mandates investigation into a new composition or synthesis of a bifunctional catalyst. A number of non-precious metal catalyst have been introduced for zinc-air batteries. Nevertheless, their catalytic activities and durability are still too low for commercial rechargeable zinc-air batteries. Thus, it is very important to synthesize a highly active bifunctional catalyst with good durability for long term charge and discharge use. In this study, it is proposed that a manganese-based perovskite oxide nanoparticle combined with nitrogen doped carbon nanotubes will show promising electrochemical activity with remarkable cycle stability as a bifunctional catalyst for zinc-air batteries.

In the first part of this work, nano-sized  $\text{LaMnO}_3$  and  $\text{LaMn}_{0.9}\text{Co}_{0.1}\text{O}_3$  were prepared to research the effectiveness of Co doping into  $\text{LaMnO}_3$  and its effect on electrochemical catalytic activities. To prepare  $\text{LaMnO}_3$  and  $\text{LaMn}_{0.9}\text{Co}_{0.1}\text{O}_3$ , a hydrothermal reaction method was applied to synthesize nanoparticles which can increase the activity of perovskite type oxides. The result shows that while perovskite oxides replacing 10 wt. % of Mn doped with Co metal did not

change its crystalline structure, the oxygen evolution reaction (OER) performance was increased by 600%.

In the second part, a core-corona structured bifunctional catalyst (CCBC) was synthesized by combining  $\text{LaMn}_{0.9}\text{Co}_{0.1}\text{O}_3$  nanoparticles with nitrogen doped carbon nanotubes (NCNT). NCNT was chosen because of its large surface area and high catalytic activity for ORR. SEM and TEM analysis show that metal oxide nanoparticles were surrounded with nanotubes. Based on the electrochemical performances, ORR and OER activity is attributed to NCNT and the metal oxide core, respectively, complementing the activities of each other. Furthermore, its unique morphology introduces synergetic activity especially for OER. Electrochemical test results show that the onset potential was enhanced from -0.2 V (in  $\text{LaMnO}_3$  and  $\text{LaMn}_{0.9}\text{Co}_{0.1}\text{O}_3$ ) to -0.09 V (in CCBC) and the half wave potential was improved from -0.38 V to -0.19 V.

In the third part, a single cell zinc-air battery test was performed using CCBC as the bifunctional catalyst for the air electrode. These results were compared with battery performance against a high-performance and expensive Pt/C based air catalyst. The results show that the battery containing catalytic CCBC consumes less energy during charge/discharge. The single cell long-term durability performance was compared, further proving that CCBC provides a more suitable catalyst for zinc-air battery than Pt/C.

## **Acknowledgements**

The author would like to thank Dr. Zhongwei Chen for his wonderful mentorship, guidance, and remarkable support during the Master's study.

Thanks to, Fathy Hassan, Rasim Batmaz, Dong Un Lee, Drew Higgins, AbdulRahman Ghannoum, Hadis Zarrin, Pouyan Zamani, Jared Lenos, Ja-Yeon Choi, Dr. Rongyue Wang, Mohammed Ariful Hoque, Raihan Ahmed, Abdel Rahman Elsayed, Gregory Lui, Victor Chabot for their support and assistance. Very special thanks to Hey Woong Park for being always understanding and supportive.

Furthermore, the author would like to acknowledge reviewers including Dr. Zhongwei Chen, Dr. Aiping Yu, and Dr. Michael Fowler.

I would like to signify special thanks to my family. Words can't express how grateful I am to my father, mother sister and brother for all of the sacrifices that you have made on my behalf. At the last but not the least I would like express appreciation to my beloved Anna Bondarenko, who was always my support in the moments when there was no one to answer my queries.

## **Dedication**

I would like to dedicate this work to my parents.

## Table of Contents

List of Figures .....	x
List of Tables .....	xiii
List of Abbreviations, Figures and Nomenclatures .....	xiv
1.0 Introduction.....	1
2.0 Background.....	3
2.1 Metal-Air Battery .....	3
2.1.1 Operational Principle of Zinc-Air Battery.....	5
2.1.1.1 Anode: Zinc Electrode .....	7
2.1.1.2 Electrolyte and separator.....	9
2.1.1.3 Cathode: Air Electrode .....	10
2.1.2 Technical Challenges.....	11
2.2 Electrochemical Catalyst.....	14
2.2.1 Perovskite Structure.....	18
2.2.3 Carbon Nanotubes .....	24
2.2.3.1 CNT Synthesis .....	27
2.3 Material Characterization.....	30
2.3.1 Scanning Electron Microscope (SEM).....	30
2.3.2 X-Ray Diffraction (XRD).....	31
2.3.3 Transmission Electron Microscopy (TEM).....	32

2.3.4 Energy Dispersive X-ray Spectroscopy (EDS, EDX) .....	35
2.3.5 X-ray Photoelectron Spectroscopy (XPS) .....	35
2.3.6 Thermogravimetric Analysis (TGA) .....	39
2.3.7 Half-Cell Electrochemical Evaluation .....	40
2.3.8 Zinc-Air Battery Performance .....	44
3.0 Effect of Co Doping in to the $\text{LaMnO}_3$ .....	46
3.1 Introduction .....	46
3.2 Experimental .....	47
3.2.1 Synthesis .....	47
3.2.2 Material characterization .....	49
3.2.3 Half-cell test .....	49
3.3 Results and Discussion of $\text{LaMnO}_3$ and $\text{LaMn}_{0.9}\text{Co}_{0.1}\text{O}_3$ .....	50
3.3.1 SEM and TEM.....	50
3.3.2 EDAX .....	53
3.3.3 XRD.....	54
3.3.4 Half-cell test .....	56
3.4 Conclusion.....	65
4.0 Combining Co Doped Oxides with NCNT .....	67
4.1 Introduction .....	67
4.2 Experimental for Synthesis of CCBC bifunctional catalyst.....	68



4.2.1 Synthesis.....	68
4.2.2 Material characterization.....	69
4.2.3 Half-cell test.....	69
4.3 Results and Discussion.....	70
4.3.1 SEM and TEM.....	70
4.3.2 EDAX.....	71
4.3.3 X-ray photoelectron spectroscopy (XPS) analysis.....	72
4.3.4 TGA.....	74
4.3.5 Half-cell test.....	75
4.4 Conclusion.....	81
5.0 Zinc Air Cell Performance.....	82
5.1 Introduction.....	82
5.2 Preparation to Test.....	82
5.3 Battery Performance.....	82
5.4 Conclusion.....	85
6.0 Summary and Future Directions.....	86
References.....	88

## List of Figures

<b>Figure 1.</b> Energy density of different metal-air batteries. ....	4
<b>Figure 3.</b> Schematic polarization curves of zinc-air cell.....	7
<b>Figure 4.</b> Different morphology zinc metal for anode .....	8
<b>Figure 5.</b> Spinel-type of metal oxides.....	17
<b>Figure 6.</b> Pyrochlore-type metal oxide.....	18
<b>Figure 7.</b> Perovskite-type metal oxides.....	19
<b>Figure 8.</b> Different planes for perovskite-type metal oxides .....	21
<b>Figure 9.</b> Carbon nanotubes. (a) single-walled nanotube (SWNT), (b) double-walled nanotube (DWNT) and (c) multi-walled nanotube (MWNT). ....	25
<b>Figure 10.</b> Rolling directions for graphene sheet during synthesis of SWNT. ....	26
<b>Figure 11.</b> Different conductivity for SWNT depending on rolling. ....	26
<b>Figure 12.</b> TEM images of N-doped CNTS grown at 850 and 950 °C .....	29
<b>Figure 13.</b> Principle of SEM operation .....	31
<b>Figure 14.</b> Principle of XRD operation.....	32
<b>Figure 15.</b> Principle of TEM operation.....	34
<b>Figure 16.</b> Principle of XPS operation. ....	36
<b>Figure 17.</b> Surface and depth analysis by XPS. ....	37
<b>Figure 18.</b> Affect of electron binding energy on chemical shifts.....	38
<b>Figure 19.</b> Schematic view of thermogravimetric analysis.....	39

<b>Figure 20.</b> Schematic view of rotating disc electrode and working electrode. ....	41
<b>Figure 21.</b> ORR polarization of an active catalyst. ....	43
<b>Figure 22.</b> Schematic view single cell zinc-air battery setup.....	45
<b>Figure 23.</b> Synthesis of $\text{LaMnO}_3$ .....	48
<b>Figure 24.</b> Synthesis of $\text{LaM}_{0.9}\text{Co}_{0.1}\text{O}_3$ .....	49
<b>Figure 25.</b> SEM images of $\text{LaMnO}_3$ a) before calcination and b) after calcination .....	51
<b>Figure 26.</b> SEM images of $\text{LaMn}_{0.9}\text{Co}_{0.1}\text{O}_3$ a) before calcination and b) after calcination .....	52
<b>Figure 27.</b> TEM analyses for a) $\text{LaMnO}_3$ and b) $\text{LaMn}_{0.9}\text{Co}_{0.1}\text{O}_3$ .....	53
<b>Figure 28.</b> EDX analyses for $\text{LaMnO}_3$ .....	54
<b>Figure 29.</b> EDX analyses for $\text{LaMn}_{0.9}\text{Co}_{0.1}\text{O}_3$ .....	54
<b>Figure 30.</b> XRD analyses for $\text{LaMnO}_3$ .....	55
<b>Figure 31.</b> XRD analyses for $\text{LaMn}_{0.9}\text{Co}_{0.1}\text{O}_3$ .....	56
<b>Figure 32.</b> ORR performance for $\text{LaMnO}_3$ .....	58
<b>Figure 33.</b> Koutecky - Levich plot for $\text{LaMnO}_3$ .....	59
<b>Figure 34.</b> OER performance for $\text{LaMnO}_3$ .....	60
<b>Figure 35.</b> ORR performance for $\text{LaMn}_{0.9}\text{Co}_{0.1}\text{O}_3$ .....	61
<b>Figure 36.</b> Koutecky - Levich plot for $\text{LaMn}_{0.9}\text{Co}_{0.1}\text{O}_3$ .....	62
<b>Figure 37.</b> OER performance for $\text{LaMn}_{0.9}\text{Co}_{0.1}\text{O}_3$ .....	63
<b>Figure 38.</b> ORR performance of $\text{LaMnO}_3$ vs. $\text{LaMn}_{0.9}\text{Co}_{0.1}\text{O}_3$ at 900 rpm.....	64
<b>Figure 39.</b> OER performance of $\text{LaMnO}_3$ vs. $\text{LaMn}_{0.9}\text{Co}_{0.1}\text{O}_3$ .....	65

<b>Figure 40.</b> Synthesis of CCBC.....	69
<b>Figure 41.</b> a) SEM image for CCBC, b) TEM image for CCBC.....	71
<b>Figure 42.</b> EDX analyses for CCBC .....	72
<b>Figure 43.</b> XPS analyses for nitrogen species in the CCBC .....	73
<b>Figure 44.</b> TGE analyses CCBC .....	75
<b>Figure 45.</b> ORR performance for CCBC .....	77
<b>Figure 46.</b> Koutecky - Levich plot for CCBC.....	78
<b>Figure 47.</b> ORR performance of $\text{LaMnO}_3$ vs. $\text{LaMn}_{0.9}\text{Co}_{0.1}\text{O}_3$ vs. CCBC at 900 rpm .....	79
<b>Figure 48.</b> OER performance for CCBC.....	80
<b>Figure 49.</b> OER performance of $\text{LaMn}_{0.9}\text{Co}_{0.1}\text{O}_3$ vs. CCBC .....	81
<b>Figure 50.</b> Charge/discharge rate for Pt/C vs. CCBC .....	83
<b>Figure 51.</b> Durability test for Pt/C vs. CCBC .....	85

## List of Tables

**Table 1.** Performance degradation factors for metal-air batteries ..... 12

**Table 2.** The binding energy and relative percentage of the surface nitrogen groups ..... 73

## List of Abbreviations, Figures and Nomenclatures

CCBC	Core-corona structured bifunctional catalyst
ORR	Oxygen reduction reaction
OER	Oxygen evolution reaction
Pt/C	Carbon supported platinum
NPMC	Non-precious metal catalyst
NCM	Nitrogen-doped carbon material
NCNT	Nitrogen-doped carbon nanotube
TPB	Triple phase boundary
CNT	Carbon nanotube
SWNT	Single-walled carbon nanotube
DWNT	Double-walled carbon nanotube
MWNT	multi-walled carbon nanotube
CVD	Chemical vapour deposition
SEM	Scanning electron microscopy/microscope
TEM	Transmission electron microscopy/microscope
EDX	Energy dispersive X-ray spectroscopy
HR-TEM	High resolution TEM
XRD	X-ray diffraction
XPS	X-ray photoelectrone spectroscopy
HR-XPS	High resolution XPS
TGA	Thermogravimetric analysis
LSV	Linear scan voltammetry

K-L	Koutecky-Levich
CV	Cyclic voltammetry
EDA	Ethylenediamine
Fc	Ferrocene
HWP	Half wave potential
EIS	Electrochemical impedance spectroscopy

## 1.0 Introduction

One of the main challenges of the 21st century is a lack of efficient energy storage devices in an increasingly technological society. Traditional batteries lack the energy density compared to petroleum and gasoline (1,2). For example, lithium-ion battery have specific energy of 100 - 200 Whkg<sup>-1</sup> whereas gasoline has 1700 Whkg<sup>-1</sup> (3-6). Growing safety and environmental concerns are preventing usage of certain batteries commercially. A case would be the challenge to use lithium ion batteries for large vehicles due to risk of explosion. Also, the electrolyte and certain other chemicals in the battery are toxic and expensive to recycle. To address this issue, there has been a global interested in researching novel energy storage technologies (7,8).

Between different battery types metal-air batteries become more attractive because they can overcome the challenges that lithium-ion batteries faced. Among metal-air battery materials, zinc and lithium-based batteries have theoretical specific energy densities of 1312 Whkg<sup>-1</sup> and 13124 Whkg<sup>-1</sup>, respectively. The biggest obstacle in metal-air batteries which determines the electrochemical performance and life time of the battery is air electrode. Oxygen evolution reactions (OER) and oxygen reduction reactions (OER) at the air electrode are the most important processes to the operation of the battery. Therefore catalysts are used to boost the reaction rates to get better battery performance.

Among the metal-air batteries, zinc-air battery is one of the most promising as a future energy storage device (9,10). Zinc-air batteries have higher energy density and specific energy than other types of battery because atmospheric air is one of the battery reactants. Comparing with silver oxide or alkaline cells, the same size zinc-air battery shows higher capacity , 200 mAh and 620 mAh respectively. Moreover, zinc-air battery should be given high privilege because of the



low price and environmental friendliness (11-13). The main issue with the making rechargeable zinc-air battery is having the right bifunctional catalyst.

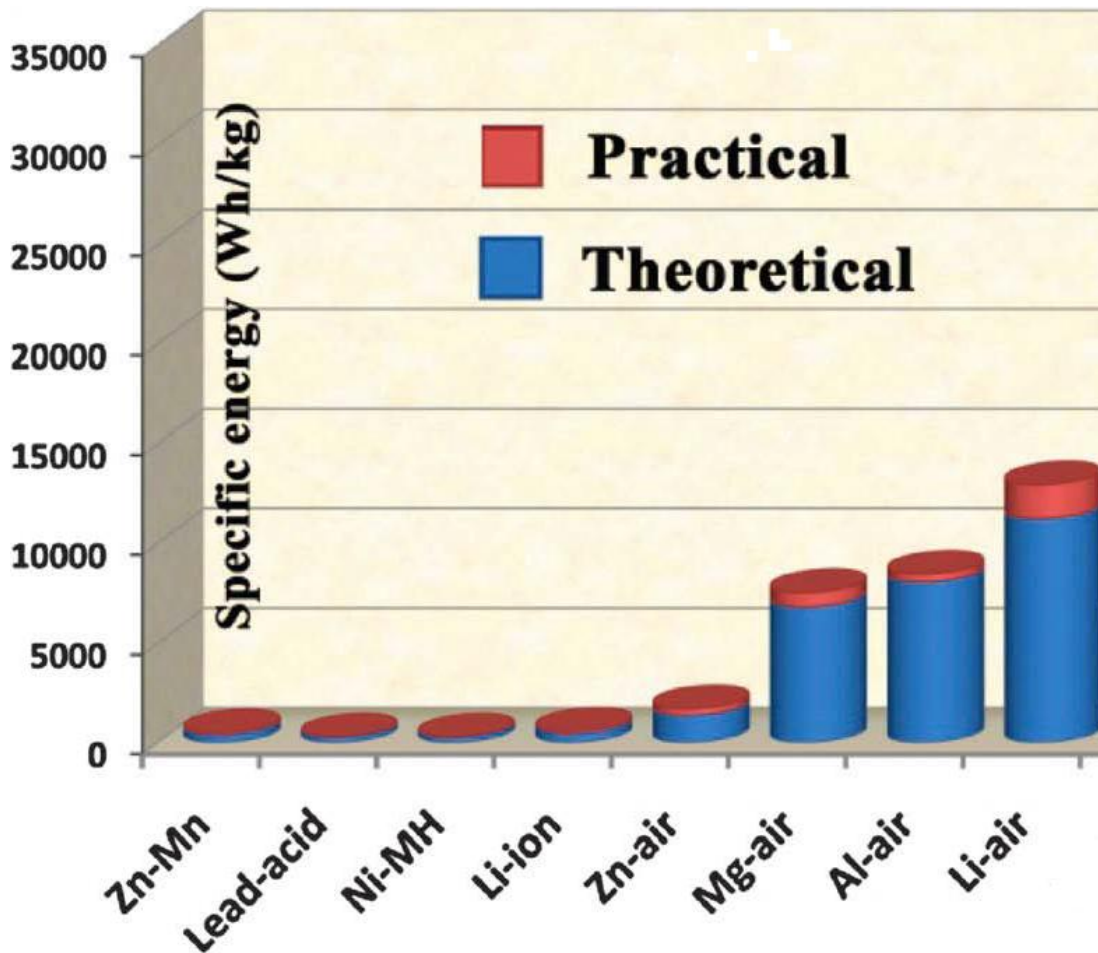
Different catalysts had been developed for metal-air batteries and the commercialized catalyst is carbon supported platinum (Pt/C). This catalyst is used for none rechargeable zinc-air batteries. However, for rechargeable batteries electrochemical performance and durability of Pt/C is not enough. Thus, developing the right bifunctional catalyst for rechargeable zinc-air batteries is very important. Right bifunctional catalyst have to be stable in electrolyte and keep the chemical composition through several cycle charge and discharge processes.

## 2.0 Background

### 2.1 Metal-Air Battery

For the first time, in 1868 Leclanche introduced metal-air battery in which the air electrode was made of manganese dioxide on carbon support. Since then many studies were performed on the development of metal-air batteries with different designs and compositions, showing that the energy density of metal-air batteries is much higher than that of other electrochemical energy storage devices (Figure 1). The high energy density of this cost-effective and environmental friendly systems is due to their open system structure, where oxygen can be provided from the air. Lithium based metal-air batteries show the highest energy density, around  $12,000 \text{ Whkg}^{-1}$  which is much higher than all well-known liquid or gasoline systems.

One of the most important aspects while designing metal-air batteries is the choice of more appropriate type of metal working as anode. For example, in Li-air battery Lithium metal is used for anode, where due to its high activity and the abundance of oxygen in air, high performance can be achieved. However, there are different challenges which are required to be overcome in order to commercialize Li-air batteries. Lithium can easily form lithium hydroxide (LiOH) during the electrochemical reaction, which corrodes the Li metal causing performance drop and the degradation of Li-air battery. Moreover, operational cost and safety issues during the production should be considered during the commercialization. Among all other metals which can be used as anode for metal air batteries zinc is the most suitable one.

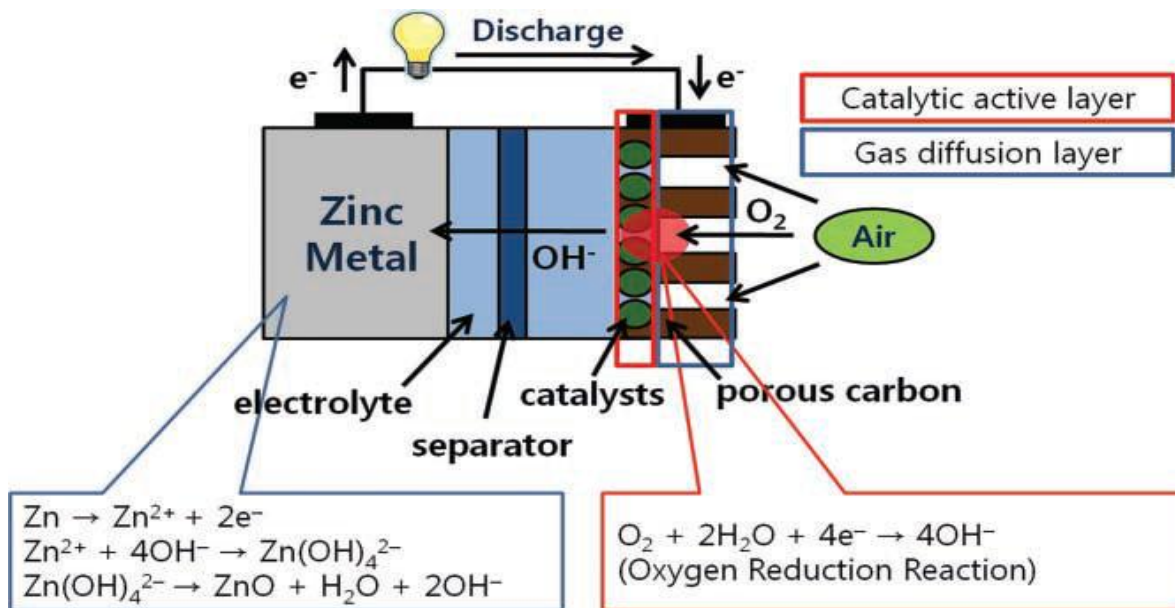


**Figure 1.** Energy density of different metal-air batteries. (14)

Electropositivity and stability in different electrolytes makes zinc most favourable for this role. Electrolyte is an environment, either alkaline or neutral, in which during the electrochemical reaction oxidized metal is transferred from anode to cathode. Other advantages of applying zinc metal in anode are: low cost, electrochemical stability, corrosion resistant, reusability, easy handling, and safety. All these advantages make zinc air very promising metal as anode for metal-air batteries. However, before using zinc-air batteries as a power source for small (cell phone) and big (vehicles) devices, it is important to overcome some issues including undesired dendrite formation, uneven dissolution, and insufficient air electrode performance.

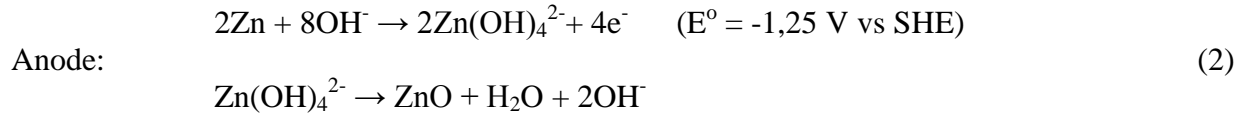
## 2.1.1 Operational Principle of Zinc-Air Battery

Zinc-air batteries have the following main constituents: zinc anode, cathode (air electrode) and separator (catalytic active layer) as represented in Figure 2. Due to low oxygen solubility at atmospheric pressure, it is used in the gas phase instead of liquid one (15,16). The operation of zinc-air battery starts from the diffusion of atmospheric oxygen into the porous carbon electrode facilitated by the difference in pressure of oxygen between the outside and inside of the cell. In Figure 2 the red circle shows the path of the oxygen molecules from air towards the electrolyte. After the diffusion occurred the catalyst aids the reduction of atmospheric oxygen to hydroxyl ions in the alkaline electrolyte with the generation of electrons from zinc metal oxidation as the anode reaction side. The process described above is a three-phase reaction because of the presence of solid catalyst, liquid electrolyte, and oxygen gas.



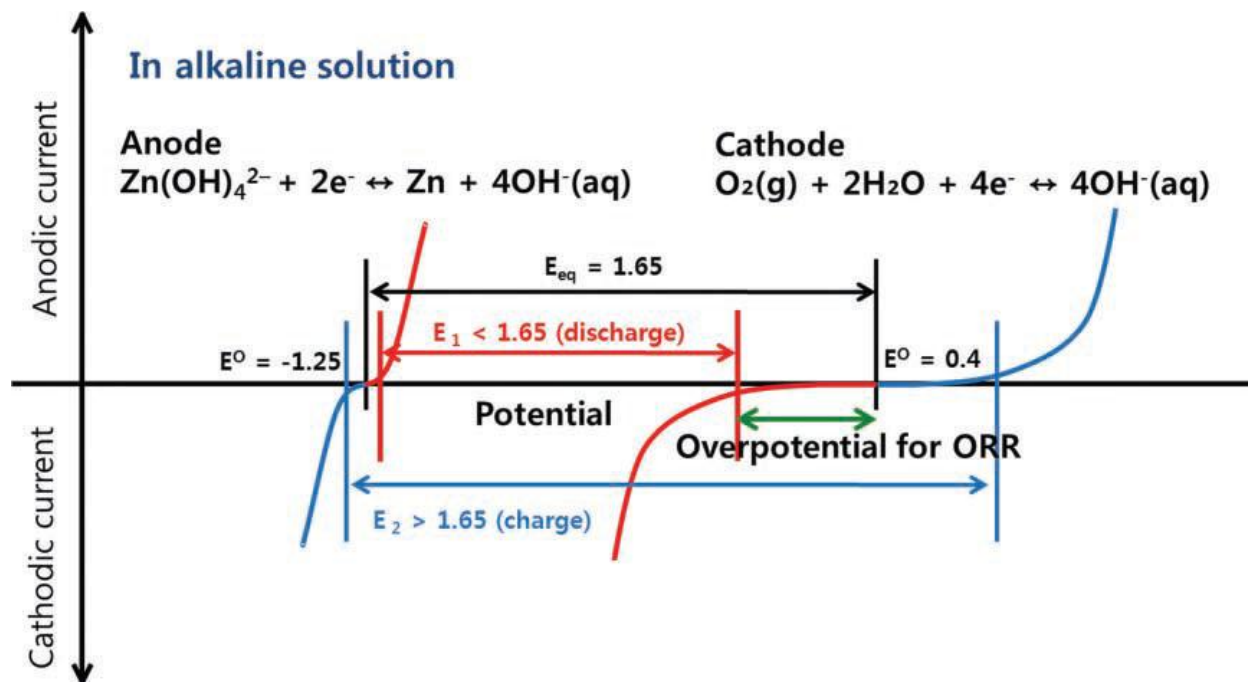
**Figure 2.** Working Principle of Zinc-Air Battery. (15)

Generated hydroxyl ions migrate from air cathode to the zinc anode to complete the overall cell reaction. This complete process can be described by the electrochemical reactions of anode and cathode in alkaline solution as follows:



As shown from the equations the equilibrium potential of zinc-air battery is 1.65 V, however, this value is somewhat lower in practice due to the internal losses of the cell due to the activation, ohmic and concentration losses (17).

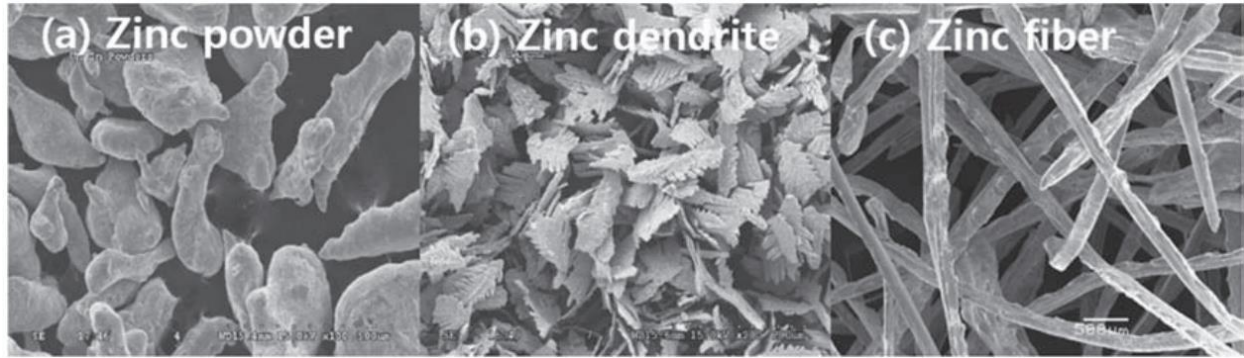
Schematic polarization curve of anode and cathode reactions can facilitate to understand the working process of zinc-air battery in greater details. Figure 3 helps to understand the major origin of potential loss in zinc-air cells using oxygen. As the Scheme implies during the discharge of Zinc-air battery (red line), cathodic and anodic currents occur at the air (cathode) and zinc (anode) electrodes, respectively, and upon charging process each current direction is reversed (blue line). It is also important to note that the overpotential at the zinc anode is relatively smaller than that at the air electrode. It also can be seen from the scheme that the large overpotential (green line on the Figure 3) is necessary to generate hydroxyl ions by oxygen reduction reaction. That is why the working voltage of the actual zinc-air batter is lower than the value of 1.65 V ( $E_{\text{eq}}$ ). If one considers the oxygen evolution reaction (OER), a larger potential is needed for charging (blue line). ORR has both positive and negative effects on zinc-air cells. From the positive point the cell is able to have large energy density because of the lack of oxygen active material in the cell.



**Figure 3.** Schematic polarization curves of zinc-air cell. (18)

### 2.1.1.1 Anode: Zinc Electrode

Pure zinc metal is used as anode for zinc-air batteries. During the discharge zinc metal oxidizes and this is the only reaction which happens on anode. Thus there is not many ways to develop anode electrochemical performance. The main way to improve the anode performance is increase the surface area for zinc metal so that it can react with electrolyte more efficiently. Different morphologies of zinc metal (shown in Figure 4) were reported as anode, whereby increasing the surface area the performance becomes higher..



**Figure 4.** Different morphology zinc metal for anode. (19)

To control the surface area of zinc electrode it is possible to press the zinc powder. Researches show that during pressing zinc powder it is possible to add some metals to this powder which will increase the electrochemical performance. One of the reported metals is mercury, which increases the conductivity between zinc particles and the current collectors. However it is very important to remove the mercury from the anode because of the environmental issues. This resulted in the decrease of electrochemical performance by increasing leaking shock resistance. On the other hand during the electrochemical reaction corrosion of zinc metal decreases the performance. During the corrosion of zinc metal hydrogen gas is generated (hydrogen evolution reaction (HER))



To prevent this corrosion different ways were developed, like adding metals like nickel, indium, cadmium and palladium. Moreover, coating the surface of zinc metal can increase resistance to corrosion. Cho et al. suggested to coat the surface of anode with  $\text{Li}_2\text{O} - 2\text{B}_2\text{O}_3$  which will help to increase the capacity of the zinc-air battery and decrease the HER. It is believed that the coated

layer acts like a blocking wall, preventing zinc from having a direct contact with electrolyte and decrease the possibility of side reactions.

### **2.1.1.2 Electrolyte and separator**

Separator is one of the main parts of metal-air batteries and separates air electrode from zinc electrode. Thus, there are some requirements for separator: stability in alkaline solution, suitable porosity and pore size, electrical insulator and high ionic conductivity. For zinc-air batteries separators are made of polyethylene, polyvinyl alcohol and polyolefin because in this batteries transport ions are hydroxyls and not protons,  $H^+$ . Unfortunately, the pore size makes it possible for zinc ions to travel to cathode side which results in the decrease of battery capacity. This challenge can be overcome by adding inorganic materials to microporous membrane. Moreover, Wu et al. reported that sulfonation of separator membrane can increase anionic transport till 0.89 in 1 M KOH electrolyte. While comparing two sulfonated and non-sulfonated separator membranes, sulfonated one gives better results. All requirements shown above are the basic ones, however there are some additional requirements like: the separator should be resistant to oxidation and keep its morphology and composition during charge and discharge processes. Moreover, the separator should show high adsorption capacity to electrolyte and retain it in its pores during the charge and discharge processes.

The common used electrolyte for zinc-air batteries is in an alkaline solution such as potassium hydroxide, sodium hydroxide and lithium hydroxide. Among those, KOH is widely used as electrolyte for zinc-air batteries because of its high conductivity ( $K^+$   $73.50 \Omega^{-1} \text{ cm}^2/\text{equiv}$ ). By changing the concentration of the KOH it is possible to change the resistance. Increasing the concentration of KOH can decrease the resistance; however it comes with some limitations. High concentration of electrolyte leads to increasing the viscosity and formation of ZnO.



Zinc-air battery is an open system, thus electrolyte can easily expose to the air and adsorb  $\text{CO}_2$  from the air forming carbonates. This is the natural reaction which decreases the amount of  $\text{OH}^-$  groups and as a result the capacity of the battery decreases.

### **2.1.1.3 Cathode: Air Electrode**

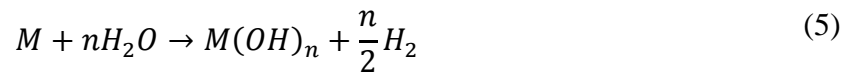
The cathode, also called the air electrode, for metal air batteries requires an effective catalyst for oxygen reduction reaction (ORR). The properties of an effective cathode electrode include: a porous structure, durability (corrosion resistant, binds well to support, etc), resistance to side reactions, and low cost. Catalyst is needed to release the activation energy for ORR. The morphology is very important factor which needs to be considered because air electrode acts like a substrate where ORR reaction happens. The only reactant for this reaction is oxygen provided endlessly by air electrode. The porosity of air electrode is very important because it makes the path for oxygen and large surface area for catalyst. Carbon based materials like activated carbon and carbon nanotubes (CNT) can be used as substrate for air electrode because of their high porosity. The air electrode consists of two layers: gas diffusion layer and catalytic active layer. Gas diffusion layer is carbon based materials which is combined with hydrophobic binder. Using hydrophobic binder helps to make gas diffusion layer penetrable to air not to water. The catalytic active layer where the ORR takes place is combination of catalyst, carbon material and a binder. All above mentioned parts and components of air electrode are very critical because their morphology and the amount of chemical components can affect the battery performance. To make a secondary zinc-air battery a proper bifunctional catalyst must be for which it is important to take the oxidation of the surface and the carbon substrate into account.

Oxygen reduction process is very complex and still it is not clear the right mechanism for it. The literature details two possible mechanisms for ORR reaction. The first one is a four-electron

pathway where oxygen directly reduces to OH<sup>-</sup>. The second mechanism is peroxide two-electron pathway where oxygen reduces to OH<sup>-</sup> via HO<sup>-2</sup>.

### 2.1.2 Technical Challenges

The performance and commercialization of Zn-air batteries depends on the design and material properties detailed in the earlier sections. Unfortunately, there are many challenges preventing secondary Zn-air batteries from being commercialized. One of the major challenges related to the metal electrode is thermodynamic stability of the metal in aqueous electrolyte. The reaction shown below allows for the formation of metal hydroxides and hydrogen gas,



This reaction is known as the parasitic corrosion reaction. Some sources name it the self-discharge reaction, which greatly degrades the coulombic efficiency of the anode. Another factor which results in decreasing the zinc air battery capacity is the migration of zinc(II) ions from the anode to the cathode. Thus, it is important to control the pore size of the separator to improve the electrochemical performance of the battery. Another source which can decrease the capacity of the battery is the hydrogen evolution reaction (HER). The morphology of the zinc metal can affect the electrochemical behavior of the battery based on how many zinc atoms are available to participate in the reaction. To make a secondary Zn-air battery, many challenges have been overcome by using different methods for coating, alloying and utilizing other additives to the electrolyte. Most of the difficulties will be overcome when we have fully understood the chemistry of zincate ion in alkaline solution (18).

The use of potassium hydroxide as an electrolyte shows high ionic conductivity. However, the main challenge is related with flaccid ORR kinetics in compound with the large activation energy of the air cathode. This problem can be overcome by using the appropriate catalyst. Making the ideal catalyst becomes difficult because of the number of elements involved in ORR and the steps for achieving full battery performance. The production of hydroperoxide, which is followed by reduction or chemical decomposition, is the result of two electron reaction tracks (20).



The possible decomposition of the chemical can decrease the total energy, which can be produced from the reaction. Moreover, the hydroxperoxide which produced during the reaction affects the performance of the catalyst negatively. The loss of capacity in any of the electrodes, air or metal, will eventually reduce the performance of the battery. Some of the factors causing the loss of performance are shown in Table 1.

**Table 1.** Performance degradation factors for metal-air batteries

Performance degradation	Description
Polarization	Large decrease in voltage with increasing current Limits battery to low- to mid-power requirement applications
Electrolyte carbonation	Carbon dioxide in air reacts with electrolyte forming carbonate Crystallization of carbonates leads to: Blockage in porous air electrode

	<p>Mechanical damage to battery</p> <p>Decrease in electrolyte conductivity</p>
Water Transport	<p>Water loss leads to a dry battery and premature failure</p> <p>Excess water leads to dilution of electrolyte and pore flooding</p>

Another main issue is related to the electrolyte, since zinc-air batteries operate in an open system. The electrolyte is always in contact with air and carbon dioxide (CO<sub>2</sub>) is absorbed by electrolyte forming carbonate ions. The presence of carbonate causes the crystallization of the electrolyte by the following reaction:

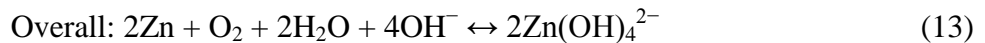


This crystallization brings out two subsequent problems: firstly, the crystallized carbonate becomes a barrier between the air and the electrolyte by depriving the electrolyte of oxygen. Secondly, the battery performance deteriorates because of the mechanical damage of the carbonate. However, comparing all the challenges that zinc-air batteries face, the difficulties faced by the air cathode are the main factors hampering this type of battery from being commercialized. 30-50% of the cost of zinc-air batteries is in the air electrode. From this percentage, precious metal catalysts like silver, silver oxide and platinum are associated with about 80% of the cost. This demonstrates the significant effect of the catalyst on the cost of zinc-air batteries, which is about 20-40%.

Moreover, during the ORR reaction, different types of radicals, such as hydroperoxides or superoxide radicals, are created. These radicals can lead to the degradation of the catalyst and impact the overall life time of the zinc-air battery.

## 2.2 Electrochemical Catalyst

Among the all challenges which are mention above, the difficulties with air cathode is the most serious one which researches are faced now. This challenge is faced in oxygen reduction reaction (ORR) during the discharge process and oxygen evolution reaction (OER) during the charge process. As a result of this challenges during ORR and OER in metal air batteries the efficiency of the air battery becomes low (2). For a rechargeable battery it is important to control both ORR and OER reaction. Thus, it is very important to use bifunctional catalyst. The most promising bifunctional catalysts are the oxides containing surface reaction  $M^{m+}-O^{2-} \rightarrow M^{(m-1)+}-O^-$ . For zinc-air battery, oxygen is reduced to hydroxyl ions nad zinc ions from the anode combine with the hydroxyl ions to form zincate ions ( $Zn(OH)_4^{2-}$ ). And future zincate ion decomposes to produce ZnO. In overall the battery reaction can be described as follows:



It is challenging to make an secondary zinc–air battery because, the reversibility of the zinc anode is difficult. In the charge–discharge cycling process, mold changes happens with zinc metal, such as the formation of dendrites. The stability of zincate ions  $Zn(OH)_4^{2-}$ (aq) in alkaline solution is a basic requirement for developing a secondary zinc electrode. However, zincate ions stats to decomposed as ZnO, as soon as  $Zn(OH)_4^{2-}$ (aq) will reach a saturation point in the hydroxide electrolyte during discharge. ZnO is a white solid powder that acts as an insulator and this makes difficult to recharge the battery. The reaction involved is:  $Zn(OH)_4^{2+} \rightarrow ZnO + H_2O +$

$2\text{OH}^-$ . To achieve good rechargeable battery performance, the main point is to understand the behavior of the zincate ion in an alkaline electrolyte. This knowledge can help to prevent the formation of ZnO and decrease the effect of other challenges on battery performance.

The need for effective electrochemical catalysts for metal air batteries opened a big research area. A number of electrochemical catalysts had been developed and all these electrocatalysts can be roughly classified into the following seven categories:

- 1) transition metal oxides, containing single-metal oxides and mixed-metal oxides;
- 2) functional carbon materials, including nanostructured carbons and doped carbons;
- 3) metal oxide–nanocarbon hybrid materials;
- 4) metal–nitrogen complex, including non-pyrolyzed and pyrolyzed;
- 5) transition metal nitrides;
- 6) conductive polymers; and,
- 7) noble metals, alloys and oxides, for example, Pt, Ag, Pt, Au, and  $\text{RuO}_2$ .

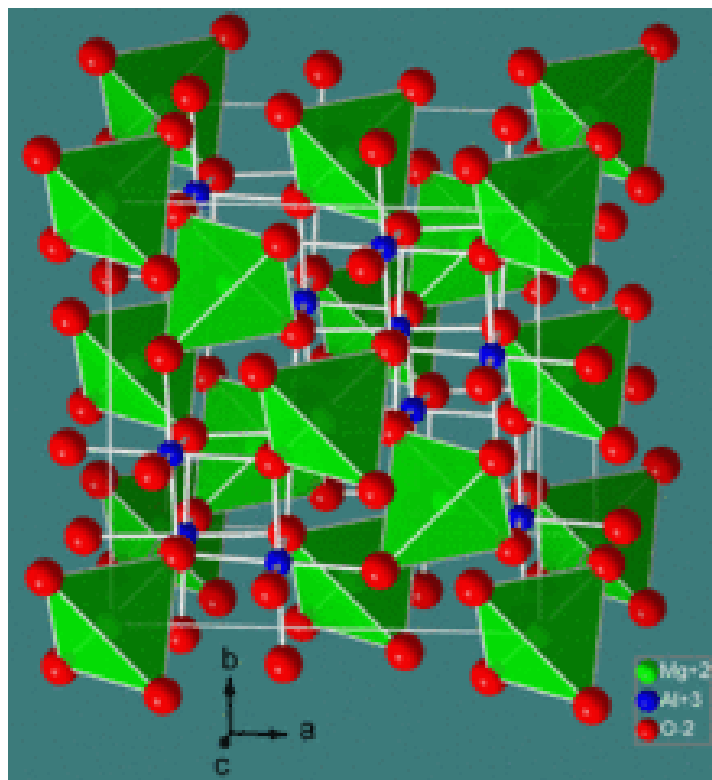
The first group of catalysts are represented by a large family of transition-metal oxides. As an alternative to noble metals, transition-metal oxides have many advantages such as high abundance, low-cost, easy of preparation, environmental friendliness and so on. Transition metal elements possess multiple valences, resulting in a variety of oxides with different crystal structures. This group has its own subgroups like Single-metal oxides and Mixed-metal oxides.

The most effective electrochemical catalysts developed in the current state of technology are platinum (Pt) based catalyst, such as Pt, Pt-Au, Pt-Pd, and Pt/C.<sup>10-12</sup>. Where platinum acts as oxygen reduction catalyst while other metal oxides as oxygen evolution catalyst. However, this solution wasn't the best because of the cost, performance and lifetime of the catalysts. Moreover

these catalysts are poisoning and very harmful for environment and the ability to effectively catalyse OER is very low.

One of the main members of this group is manganese oxides it can simultaneously serve in catalytic ORR and OER reactions. Thus making them attractive as bifunctional catalysts for secondary metal air batteries. Since 1970s many research works have been promoted to quantify and increase the catalytic performance of  $\text{MnO}_x$  based catalysts. The chemical composition, texture, morphology, oxidation state, and crystalline structure have been examined as functions of the electrocatalytic properties. The results showed that the electrochemical performance of  $\text{MnO}_x$  based catalysts are strongly affected by the crystallographic structure of  $\text{MnO}_2$  in the following order  $\alpha$ - >  $\beta$ - >  $\gamma$ . Moreover, the morphology is another strong factor that controls the catalyst properties.

Mixed-metal oxides in 3 different structure are largely used for ORR and OER performance: spinel, perovskite and pyrochlore. Spinels-type of oxides with the formula  $\text{AB}_2\text{O}_4$ , where A is a divalent metal ion (such as Mg, Fe, Co, Ni, Mn, or Zn) and B is a trivalent metal ion (such as Al, Fe, Co, Cr, or Mn). Because of the hopping processes between the cations of different valences the activation energy becomes low. Thus, mixed valences exhibit electrical conductivity or semiconductivity and show good performances in oxygen evolution and reduction. Based on the cations used as A and B, the ratio can be varied to adjust the catalysis performance. However, this is just one of the factors that can affect the electrochemical performance.



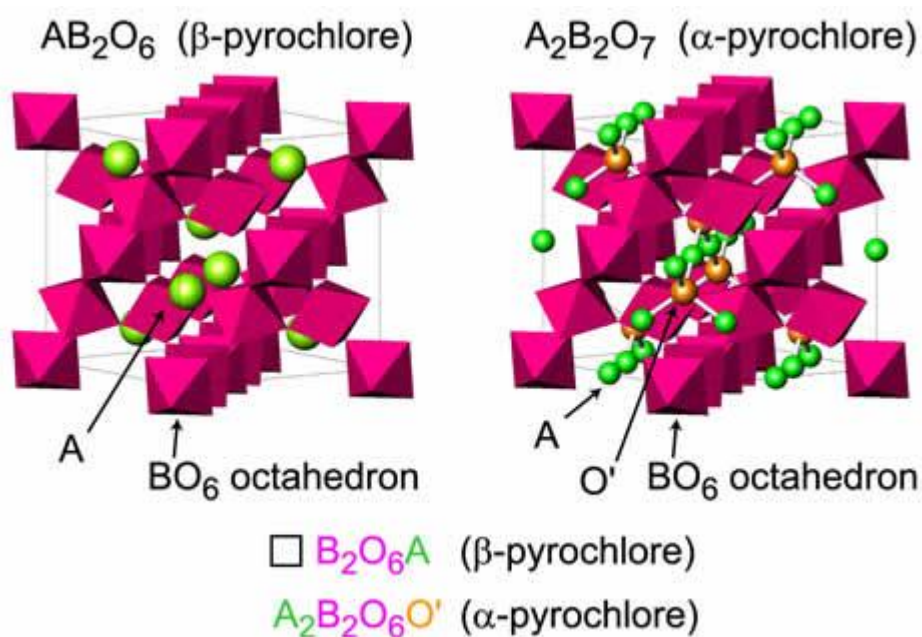
**Figure 5.** Spinel-type of metal oxides. (21)

The nanostructure of the catalysts is also greatly influenced by the activity. Wu and co-workers reported self-standing mesoporous  $\text{Ni}_x\text{Co}_{3-x}\text{O}_4$  nanowire arrays and their electrocatalytic performance in the OER. This catalyst shows better catalytic activity which can be explained with two structural advantages: first, there is a big open space between the nanowires. Thus, it is easy for each nanowire to participate in electrochemical reaction; secondly, large surface area of mesoporous nanowires increases the reaction speed by providing better diffusion for active species. As a result, at the same overpotential,  $\text{NiCo}_2\text{O}_4$  nanowire shows an approximately six times larger current density than pure  $\text{Co}_3\text{O}_4$  powder.

Pyrochlore-type oxides have a general formula  $\text{A}_2\text{B}_2\text{O}_6\text{O}'_{1-\delta}$ , where A is Pb or Bi, B is Ru or Ir. The structure of this type of oxides is made by corner-shared metal-oxygen octahedra ( $\text{BO}_6$ ). This octahedra generates the main framework which provides conduction part. At the same time the A



element is linearly connected with special oxygen atom (O'). This oxygen atom creates corner-shared tetrahedra. The main privilege for this type oxides is their extremely flexible stoichiometry and structure. First of all the special oxygen which creates tetrahedra can be partially or completely absent, resulting in up to 7% oxygen vacancies in the lattice when  $\delta = 0.5$ ; or vice-versa, the lattice can be filled with oxygen to give the composition  $A_2B_2O_7$ . The conductivity of single crystals for this oxides at room temperature is  $4.3 \times 10^3 \text{ S cm}^{-1}$ . Based on stoichiometric flexibility of this type oxides, the catalytic properties can be controlled by changing the doping concentration of A metal verses to B.

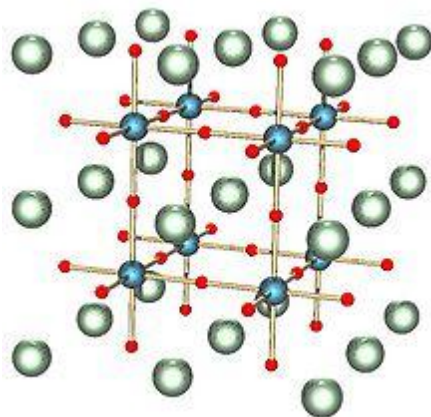


**Figure 6.** Pyrochlore-type metal oxide. (21)

### 2.2.1 Perovskite Structure

The last member of mixed-metal oxides group is perovskite-type oxides with the general formula  $ABO_3$ . Unlike the previous types, perovskite-type oxides attracted more interest as bifunctional catalysts for air batteries because of the possibility to use wide range of cations to replace A and

B. The cubic perovskite crystal lattice is a durable host for a number of mixed transition metal oxides. Substituted perovskites can generally be described by the formula  $A_{1-x}A'_x B_{1-y}B'_y O_3$ , where A or A' is a rare-earth or alkaline-earth metal and B or B' is a transition metal. The activity of the transition metal oxide catalysts can be explained with the ability of the cations to adopt different valence states, especially when these oxides form redox couples at the potential of oxygen reduction and oxygen evolution reaction. Therefore, different perovskite-type oxides with various replacements have been conducted as bifunctional catalysts.



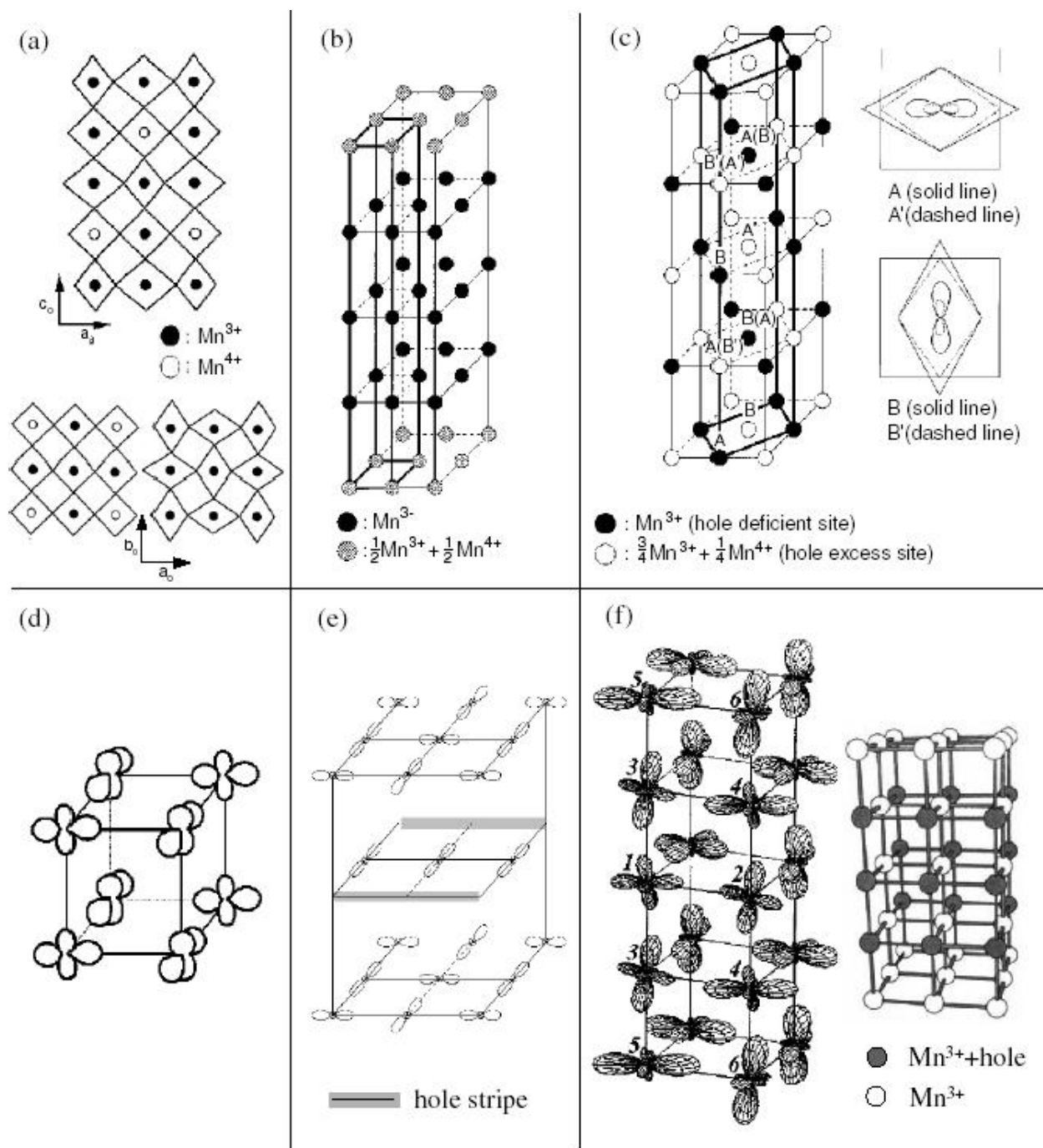
**Figure 7.** Perovskite-type metal oxides. (22)

The ideal structure of perovskite is a cubic lattice. However, in nature is very rare to find this structure, usually oxides have slightly distorted variants with lower symmetry like hexagonal or orthorhombic. In the ideal structure, the distance is different for A-O and B-O where the atoms are touching one another. The B-O distance is equal to  $a/2$  ( $a$  is the cubic unit cell parameter) while the A-O distance is  $(a/\sqrt{2})$  and the following relationship between the ionic radii holds:  $r_A + r_O = \sqrt{2}(r_B + r_O)$ . However, it was found that, even if this equation is not obeyed for  $ABO_3$  compounds, it still keeps the cubic structure. Goldschmidt introduced a tolerance factor ( $t$ ), defined by the equation:

$$t = (r_A + r_O)/\sqrt{2}(r_B + r_O) \quad (14)$$

which is applicable at room temperature to the empirical ionic radii. Although for an ideal perovskite this is unity, this structure is also found for lower  $t$ -values ( $0.75 < t < 1.0$ ). When the  $t$ -value is close to high temperatures the structure is ideal cubic, but usually a different perovskite structure appears. All these structures can be modified by controlling B and B' type doping consecration.

The crystal structure of perovskite oxides had been investigated by XRD analysis technique and the diffraction peaks for this type of oxide at  $2\theta$  angles appeared in the order of  $23^\circ$ ,  $32.5^\circ$ ,  $41^\circ$ ,  $47^\circ$ ,  $58.5^\circ$  and  $68.65^\circ$  and they can be assigned to scattering from the (1 1 0), (1 1 2), (0 2 2), (2 2 0), (3 1 2) and (4 0 0) planes of the perovskite type crystal lattice, respectively (23). Because of the charge and orbital ordering different peaks and planes occur. Based on experimental as well as theoretical studies different possible planes had been proposed. The resonant x-ray scattering (RXS) study shows that the angle between orbital of the same and different atoms plays a great role in the formation of these planes (24-26). Some of these planes are shown in Figure 8. They are listed as follows: (a) charge and polaron ordering. Undoped  $\text{MnO}_2$  -planes alternate with quarter doped planes (27). (b) Segregation into half doped and undoped planes (28). (c) Checkerboard-like charge ordering accompanied by static orbital waves along the  $c$ -axis (29). (d) Orbital ordering without charge order (30). (e)  $\text{MnO}_2$  -planes containing hole stripes alternate with undoped planes (31). (f) Long-range orbital-ordered phase with three-line hole stripes. Hole rich planes are separated by undoped planes (32).



**Figure 8.** Different planes for perovskite-type metal oxides. (21)

One of the main properties studied for finding better perovskite catalysts is oxygen adsorption because of the importance of these compounds as oxidation-reduction catalysts. The results of different works show that the crystal structure and the temperature play a great role in oxygen

adsorption. Thus surface area and the surface charge are very important for the speed of adsorption. These goals can be achieved based on the preparation of the oxides.

Perovskite-type oxides of the composition  $\text{La}_{1-x}\text{Ca}_x\text{MO}_3$  ( $M = \text{Ni, Mn, Co}$ ) have attracted considerable attention because of their reasonable electrocatalytic activities and corrosion resistance, especially when  $x$  is equal to 0.4. This composition can easily replace noble metals because of its good ORR and OER catalytic activity and made this oxide one of the most promising bifunctional catalysts. Interestingly, the electrocatalytic properties can be tuned by changing the oxidation state of cobalt and additionally, by the increase of phase purity and decrease of crystallite size. Further work showed that depending on the A' and B' type doping the catalytic activity of oxide can be improved. For example, Sr-substitution showed better performance at oxygen evolution, whereas, the Ca substituted material showed slightly better performance upon oxygen reduction.

Particularly, perovskite oxides have been suggested as promising candidates for bi-functional catalysts for efficient ORR and OER because they are well-known to exhibit good cation ordering, which can provide disorder-free channels of oxygen vacancies to enhance the mobility of oxygen ions. The auspicious approach to improve the performance of the metal oxides is shrinking their size to nano-scale which increases their surface area and hence supplying more active sites to oxygen related reactions. Insufficient catalytic activity for ORR of the metal oxides needs to be improved to render a commercially viable bi-functional catalyst as an effective electrode material for metal-air batteries.

In this work perovskite oxides synthesised as a bifunctional catalyst and the performance was improved by combining this oxide with nitrogen doped carbon nanotubes. Different synthesis of oxide and nitrogen doped carbon nanotubes are discussed in this chapter as well as the

advantages and disadvantages of these techniques. Also, methods of physical characterization of the synthesized material are discussed in detail in order to provide understanding of the materials and their properties. These characterizations include Scanning Electron Microscopy (SEM), Transmission Electron Microscopy (TEM), X-Ray Diffraction (XRD). The performance as electrochemical catalysts was evaluated through three-electrode half-cell testing.

Oxide nanoparticles can exhibit unique chemical and physical properties due to their nano size, high density and surface area. Particle size is one of the main factors that can influence the properties of oxides and in general these properties can be divided into three groups. The first parameters affected by particle size are lattice symmetry and cell parameters (33). Nanoparticles are usually stable systems with well defined crystallographic structures. However, the growing importance of surface free energy and stress with decreasing particle size must be considered: changes in thermodynamic stability associated with size can induce modification of cell parameters and/or structural transformations (34,35). In order to display mechanical or structural stability, a nanoparticle must have a low surface free energy. As a consequence of this requirement, phases that have a low stability in bulk materials can become very stable in nanostructures. This structural phenomenon has been detected in  $\text{TiO}_2$ ,  $\text{VO}_x$ ,  $\text{Al}_2\text{O}_3$  or  $\text{MoO}_x$  oxides (35,36).

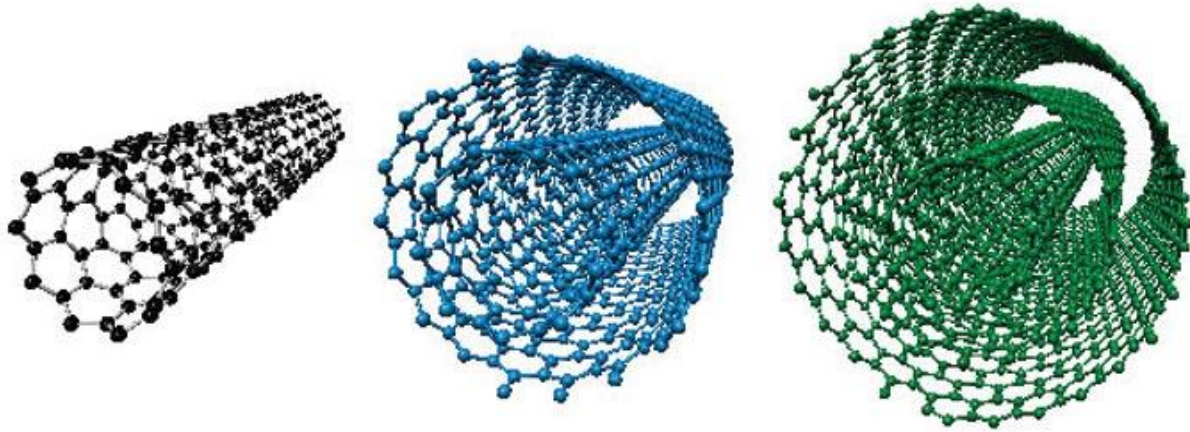
The second important effect of size is on electronic properties. The nanostructure produces the so-called quantum size or confinement effects which essentially arise from the presence of discrete, atom-like electronic states. From a solid-state point of view, these states can be considered as being a superposition of bulk-like states with a concomitant increase in oscillator strength (37). The main factor influences to electronic properties is long range bulk oxide surface Madelung field. This will be presented in nanostructured oxides too. Theoretical studies of oxides show that

while going from large periodic structure to small, redistribution of charge is relatively small for ionic but significantly high for covalent ones (38-40). The third group of properties influenced by particle size is a band gap. In their bulk state, many oxides have wide band gaps and a low reactivity (41). Changes in particle size do in fact change the magnitude of the band gap as a result the chemical activity and conductivity changes greatly (42).

One of the areas of fundamental importance to the understanding and development of nanoscale materials is the development of synthetic methods, which allow scientists control over such parameters as particle size, shape, size distribution, and composition. A number of different synthesis methods for metal oxide nanoparticles have been developed with combined control over all these parameters. In generally these methods can be divided in to 2 groups: liquid-solid (21) and gas-solid (21).

### **2.2.3 Carbon Nanotubes**

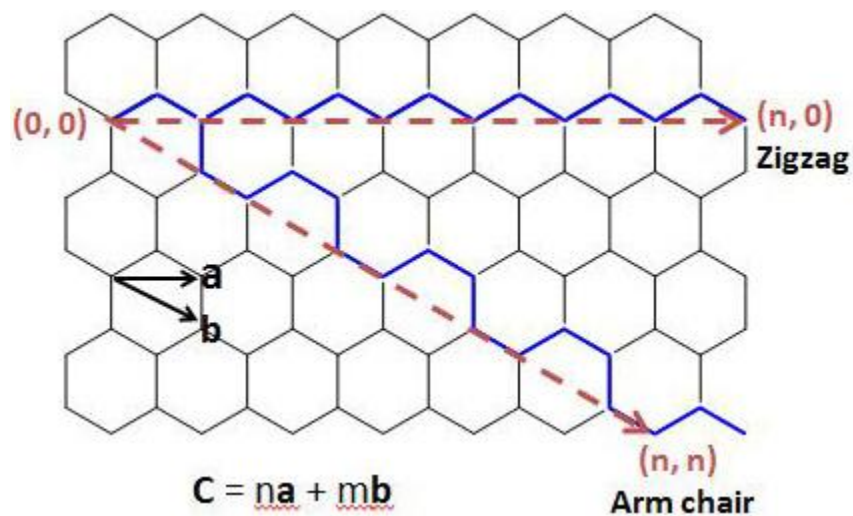
Nanostructured carbons (NSC) can be in different forms like nanofibers or nanotubes and they show great potential as catalysts or catalyst support materials (43,44). Carbon nanotubes (CNT) have drawn attention since 1991 after the discovery of Bucky balls ( $C_{60}$ ) or fullerene (45). Atomic composition of CNT is very simple, however it show very good performance in mechanical(46), chemical (47) and electrical (48) properties. Carbon nanotubes have the same structure like graphene however for CNT the difference is that the sheets are rolled up in a hollow cylindrical structure. Based on the number of the layers rolled together CNT can be divided in 3 different groups: single-walled nanotube (SWNT), double-walled nanotube (DWNT) and multi-walled nanotube (MWNT).



**Figure 9.** Carbon nanotubes. (a) single-walled nanotube (SWNT), (b) double-walled nanotube (DWNT) and (c) multi-walled nanotube (MWNT). (46)

Nanotubes have been constructed with length-to-diameter and the diameter for these 3 groups will vary not just because of the number of atoms rolled together, but also because of the number of layers. As the number of layers increase the size and the density will increase which results in a big gap in performance between SWNT and MWNT.


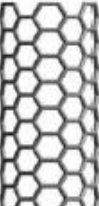

Moreover, depending on how the graphene sheet is rolled the band gap can vary and this will give different electrical conductivity. Let's look at this phenomena on the SWNT example.





**Figure 10.** Rolling directions for graphene sheet during synthesis of SWNT. (46)

They have unique electronic properties which can change significantly with the chiral vector,  $C = (n, m)$ , the parameter that indicates how the graphene sheet is rolled to form a carbon nanotube. Thus, based on the way of rolling for SWNT band gap can vary from 0 to 2 eV and electrical conductivity can show metallic or semiconducting behavior(49).

$(n, m)$	Form of SWNTs	Electrical Conductivity
$(n, 0)$	 Zigzag	Metallic when $n$ is the multiple of 3, otherwise, semiconducting
$(n, n)$	 Armchair	Metallic
$(n, m)$ when $m \neq 0$ , and $n$	 Chiral	Metallic when $(2n+m)/3$ is an integer, otherwise, semiconducting

**Figure 11.** Different conductivity for SWNT depending on rolling. (49)

One of the main advantages of CNT is its electrical properties, where it shows extremely high current density far beyond some metals (48). Moreover, CNT can keep its performance as a catalyst for ORR in both aqueous and alkaline conditions. The reason for such performance is

stable  $sp^2$  hybridized covalent bonds. The electronic properties of SWCNTs depend strongly on size and chirality, the parameters which can't be controlled during the experiment. However, electrochemical activity can be controlled by heterogeneous dopants. Unfortunately, it is not always energetically favorable for most of the impurity atoms to reside in the hexagonal network of carbon network due to their unique one-dimensional structure related to quantum confinement and curvature. The process of replacing C atoms by impurity atoms in the walls is known as sidewall functionalization or substitutional functionalization. The natural choices of these dopants are mostly boron (B) or nitrogen (N), due to three mainly reasons. First, B and N are the nearest neighbors of C and by replacing C with B or N will not affect the total number of the electrons in the system. Secondly, both B and N have atomic radii similar to C. Thirdly, B and N doped CNT can be either p-type or n-type and be used in semi-conductors. Moreover, comparing with other carbon based materials like graphene, carbon films or diamond, the surface to volume ratio of CNT is very large. This is the key property in the reactions because, increasing the ratio of CNT means that more atoms can be involved in the reaction at the same time (50). By changing the amount of the doping different performance was achieved. After all electrochemical analyses it proved that the N doped CNT shows better electrochemical performance (51-53).

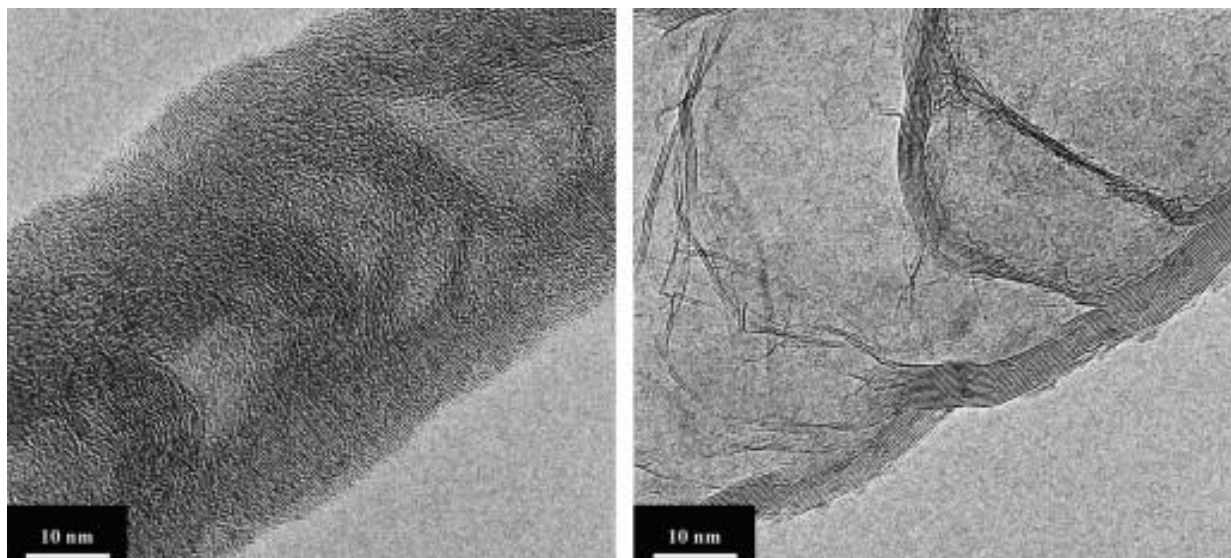
### **2.2.3.1 CNT Synthesis**

The synthesis methodology is very important for producing good quality nitrogen doped carbon nanotubes (NCNT). Because, the temperature plays a great role in formation of nanotubes and in dispersion of N. Based on this there are two routes for synthesis: High temperature and low temperature synthesis. High temperature synthesis is usually around 1300 K and has two main approaches: post synthesis modification of CNT with nitrogen containing organic molecules (54-

56) or incorporation of nitrogen during synthesis of the CNT (57,58). The main drawback for the first method is complexity and the number of the steps needed for synthesis. For the second method, nitrogen incorporation during the synthesis is easier and different sources like laser ablation 22 or arc discharge can be used. Low temperature synthesis is usually between 900 K and 1100 K and good examples for this method can be pyrolysis of N-containing organo-metallic compounds sometimes in the presence of an additional C/N source (58-60) or chemical vapour deposition (CVD) of N-containing organic compounds over a supported transition metal based catalyst. The main challenge for synthesis NCNT is to incorporate a high quantity of nitrogen into the graphene layers of the CNT to obtaining a high N/C ratio. With high temperature techniques like laser ablation the highest concentration for N which can be achieved is 33 w% (61) whereas for low temperature techniques, such as CVD, it can be 20 w% (62).

CVD is the most widely used technique because of its simple steps and respectively easy control of substance flow rate. The synthesis depends on the substrate and the chemical composition which provides carbon and nitrogen gas mixture. The substrate can be metals like Nickel (Ni) or Iron (Fe), or their oxides, or silicon coated with different metal compositions. The substrate is heated till 900 K – 1000 K and by inert gas flow (Ar) the C/N mixture reaches substrate. Formation of nanotubes starts at sublimation temperature. At this temperature substrate will form small droplets and carbon and nitrogen containing materials will precipitate on these droplets. Each droplet can support a limited amount of precursor, while the carbon will start to form hexagonal network. Thus, the synthesized nanotube will consists of nitrogen atoms disrupting the original hexagonal network of CNT due to its bonding properties. Bao at al. (63) investigated the morphology of the N-doped CNTs synthesised by CVD at different temperatures and they were characterized by TEM. The N-doped CNTs prepared at all temperatures exhibit bamboo-like,

corrugated structures. High-resolution TEM images of N-doped CNTS grown at 850 and 950 °C are shown in Fig (e) and (f), respectively. The N-doped CNTs synthesized at 850 °C contain ridged graphitic sheets over a large area, showing a lower degree of crystallinity than those synthesized at 950 °C. Therefore, the crystallinity of the CNTs is affected by the synthesis temperature. (63)



**Figure 12.** TEM images of N-doped CNTS grown at 850 and 950 °C. (64)

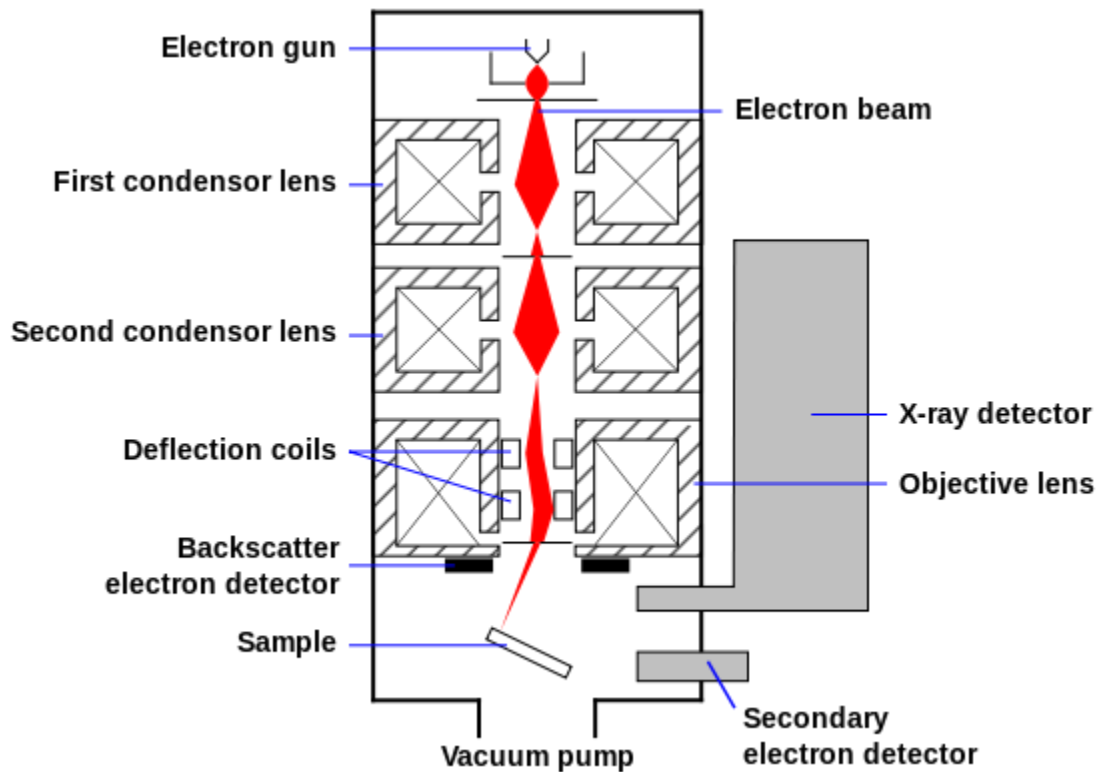
Another result reported by Kambiz et al (65) proves that the temperature is critical for synthesis of NCNT with high electrochemical activity. The N-CNTs were synthesized via a CVD method using a mixture of ethane, ammonia and argon. The synthesis temperature range was from 400 °C to 950 °C. The investigation of the results showed that the concentration of nitrogen in the NCNT decreased with increasing synthesis temperature. The synthesis temperature not only affected the nitrogen content of the N-CNTs, but also varied the type of nitrogen incorporation. The average diameter and length of N-CNTs were increased with increasing synthesis temperature. The highest aspect ratio of the N-CNTs was obtained for N-CNTs synthesized at

750 °C. TEM results revealed mainly bamboo-like structures for N-CNTs. Moreover, by increasing the synthesis time the mass and the length on NCNT were increased (65).

## 2.3 Material Characterization

### 2.3.1 Scanning Electron Microscope (SEM)

SEM is a type of electron microscope which uses focused beam of electrons to capture the picture. The surface of the sample is bombarded with electrons and as soon as they hit the surface, different types of signals produced. By using the detectors these signals are recorded and give information about the surface topography and composition. Because of the very narrow electron beam, SEM can produce extremity high-resolution images of sample surface details less than 1 nm in size. Moreover, by using back-scattered electrons it is possible to provide the information about the different elements in the sample. (66) (67) (68).



**Figure 13.** Principle of SEM operation. (67)

Sample preparation is minimal for the SEM and includes acquisition of a sample that will fit into the SEM chamber and some accommodation to prevent charge build-up on electrically insulating samples. Most electrically insulating samples are coated with a thin layer of conducting material, commonly carbon, gold or some other metal or alloy. Most SEM's are comparatively easy to operate, with user friendly interfaces. Many applications require minimal sample preparation and data acquisition is rapid. Almost all kind of samples could test, including non-conducting materials, and does not require electron transparent sample. In this work SEM was used to monitor formation of nanoparticles during the synthesis, nanoparticles size, size distribution and morphology.

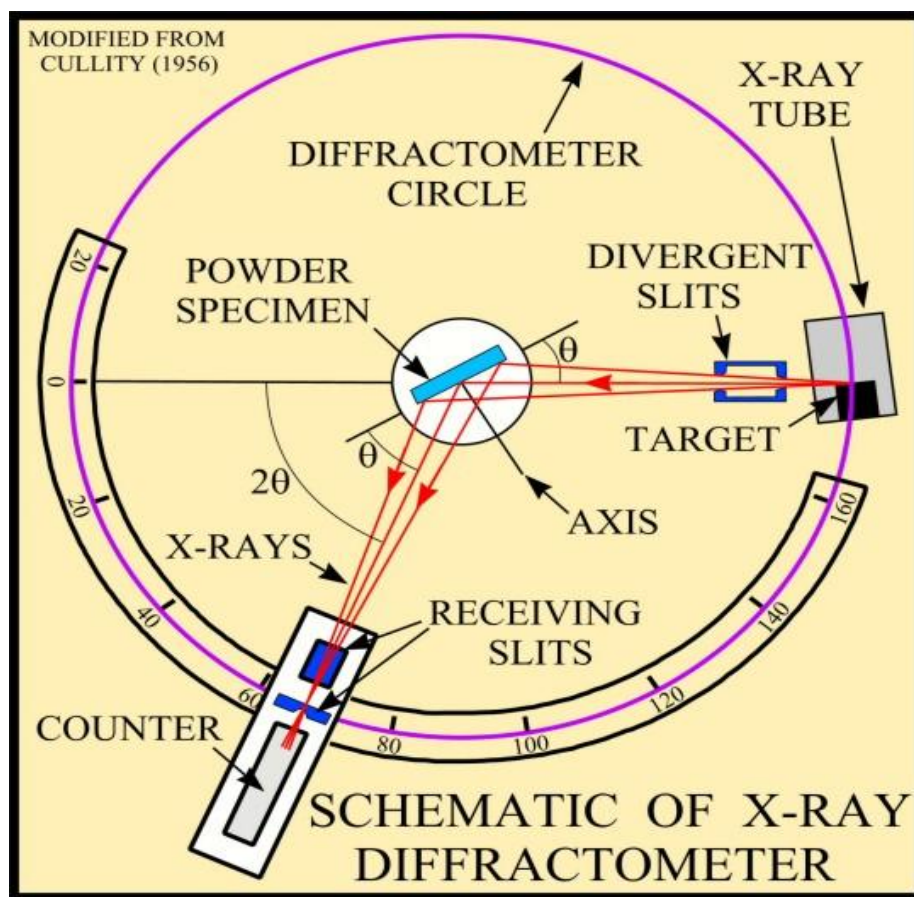
### **2.3.2 X-Ray Diffraction (XRD)**

That refined method for X-ray diffraction consists of an x-ray beam, typically from a copper  $K\alpha$  source, diffracted off of the sample to a detector. The angle and pattern of those diffractions, measured between the incident beam and the detected beam, are what show crystal structure. The principle of XRD obeys the well-known Bragg's law which is shown in equation:

$$2d \sin \theta = n\lambda \quad (15)$$

where  $n$ ,  $\lambda$ ,  $d$ , and  $\theta$  represent the order of the spectrum (any integer), the wavelength of the X-rays, the spacing between diffracting planes, and the incident angle, respectively. As a result, an XRD pattern, which is the intensity of diffracted X-ray versus the angle, is obtained. Miller Indices are a way in which to describe the orientation of a crystallographic plane within the crystal structure of the substance. These planes, however, vary in shape and size according to

the chemical composition of the substance in question. As a result of these variations, different substances and crystals reflect x-rays at differing angles. This variation of x-ray reflection angle allows analysts to determine not only the chemical composition of a given sample, but also the crystal structure. Due to the versatility of X-ray diffraction, the technique has become a mainstay of microstructure and micro-chemical analysis (19). X-ray with specific energy can be produced from a monochromatic source (69). In this work XRD analyses was used to show the crystal structure which was formed during the synthesis.



**Figure 14.** Principle of XRD operation. (70)

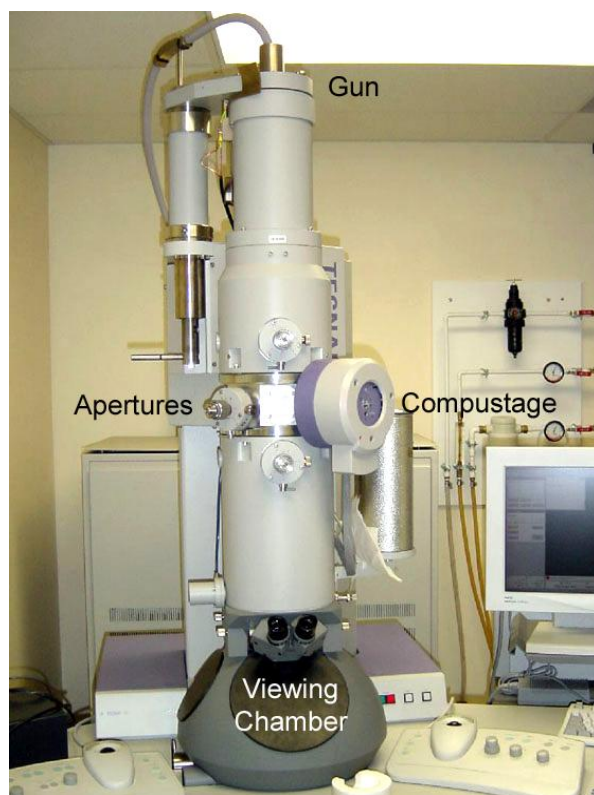
### 2.3.3 Transmission Electron Microscopy (TEM)

A TEM produces an image that is a projection of the entire object, including the surface and the internal structures. The incoming electron beam interacts with the sample as it passes through the entire thickness of the sample. Therefore, objects with different internal structures can be differentiated because they give different projections. In a sense, a transmission electron microscope works in much the same way as an optical microscope. At the top of the column, there is a high voltage electron emitter that generates a beam of electrons that travel down the column. These electrons pass through the sample and a series of magnifying magnetic lenses, to where they're ultimately focused at the viewing screen at the bottom of the column. Different lenses can be used to change the magnification and focal point of the image. Apertures along the column can be used to change the contrast and resolution of the image. The column itself is at a very high vacuum to minimize interactions between the electron beam and air molecules (71).

Following are the principal parts of a TEM:

.





**Figure 15.** Principle of TEM operation. (72)

Perhaps the most commonly used feature of TEM is the high resolution imaging where the resolution can reach 0.5 nm (72). High resolution TEM (HRTEM) allows the imaging of crystallographic information of the sample. Imaging in HRTEM mode is not based on electron amplitude contrast, rather it operates on the interference of the existing wave of the incident electron beams. Currently, the factor affecting the resolution of TEM is the spherical aberration. The limitation of TEM is the relatively more time consuming sample preparation and longer turnaround time (73). In this work TEM was used to monitor formation of nanoparticles during the synthesis, nanoparticles size, size distribution, growing of nanotubes on the metal oxide nanoparticles and morphology.

### **2.3.4 Energy Dispersive X-ray Spectroscopy (EDS, EDX)**

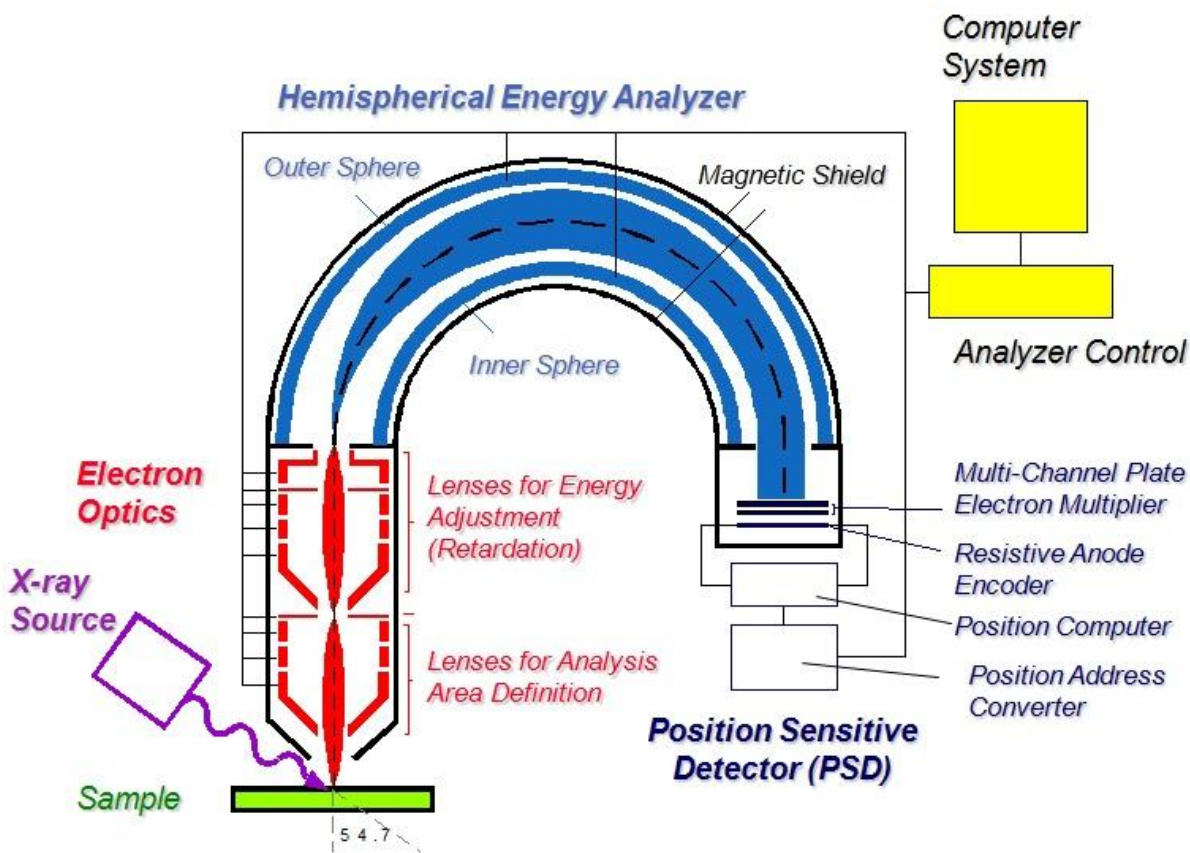
Energy Dispersive X-ray Spectroscopy is a qualitative and quantitative X-ray microanalytical technique that can provide information on the chemical composition of a sample for elements with atomic numbers greater than four. EDS systems are typically integrated into SEM instrument. EDS systems include a sensitive x-ray detector, a liquid nitrogen Dewar to limit thermal noise in the signal, and software to collect and analyze energy spectra.

An EDS detector generally contains a silicon crystal that absorbs the energy of incoming x-rays by ionization, yielding free electrons in the crystal that become conductive and produce an electrical charge bias. The x-ray absorption thus converts the energy of individual x-rays into electrical voltages of proportional size; the electrical pulses correspond to the characteristic x-rays of the element. Supporting software, including standardized material references, make it possible to readily identify peaks, which makes EDS a great survey tool to quickly identify unknown phases prior to quantitative analysis. The energy peak overlaps among different elements generated by emission from different energy level shells is the major drawback for EDS system.

### **2.3.5 X-ray Photoelectron Spectroscopy (XPS)**

The XPS technique is used to investigate the chemistry at the surface of a sample. The basic mechanism behind an XPS instrument is illustrated in below picture, where photons of a specific energy are used to excite the electronic states of atoms below the surface of the sample. Electrons ejected from the surface are energy filtered via a hemispherical analyzer (HSA) before the intensity for a defined energy is recorded by a detector. Since core level electrons in solid-state atoms are quantized, the resulting energy spectra exhibit resonance peaks characteristic of

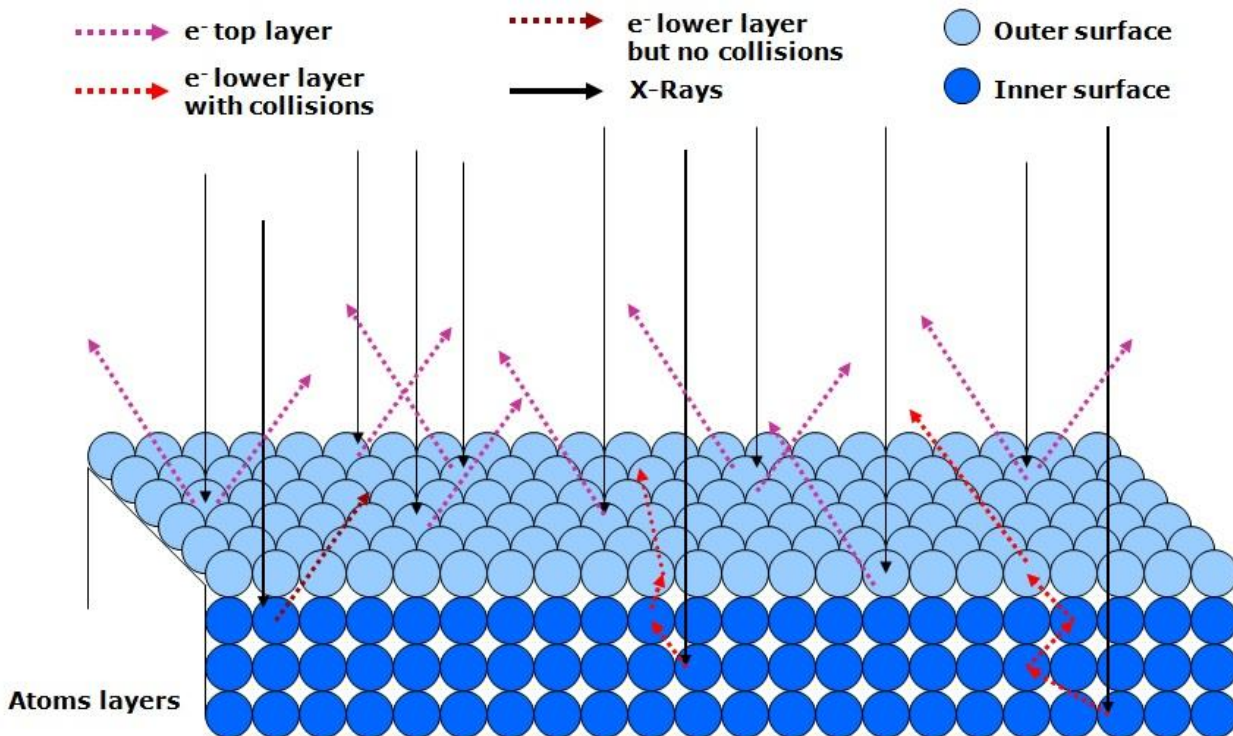
the electronic structure for atoms at the sample surface. While the x-rays may penetrate deep into the sample, the escape depth of the ejected electrons is limited. That is, for energies around 1400 eV, ejected electrons from depths greater than 10nm have a low probability of leaving the surface without undergoing an energy loss event, and therefore contribute to the background signal rather than well defined primary photoelectric peaks (74).



**Figure 16.** Principle of XPS operation. (66)

XPS is a quantitative technique in the sense that the number of electrons recorded for a given transition is proportional to the number of atoms at the surface. The chemical shifts seen in XPS data are a valuable source of information about the sample. Tilting the sample with respect to the

axis of the analyzer results in changing the sampling depth for a given transition and therefore data collected at different angles vary due to the differing composition with depth (70).

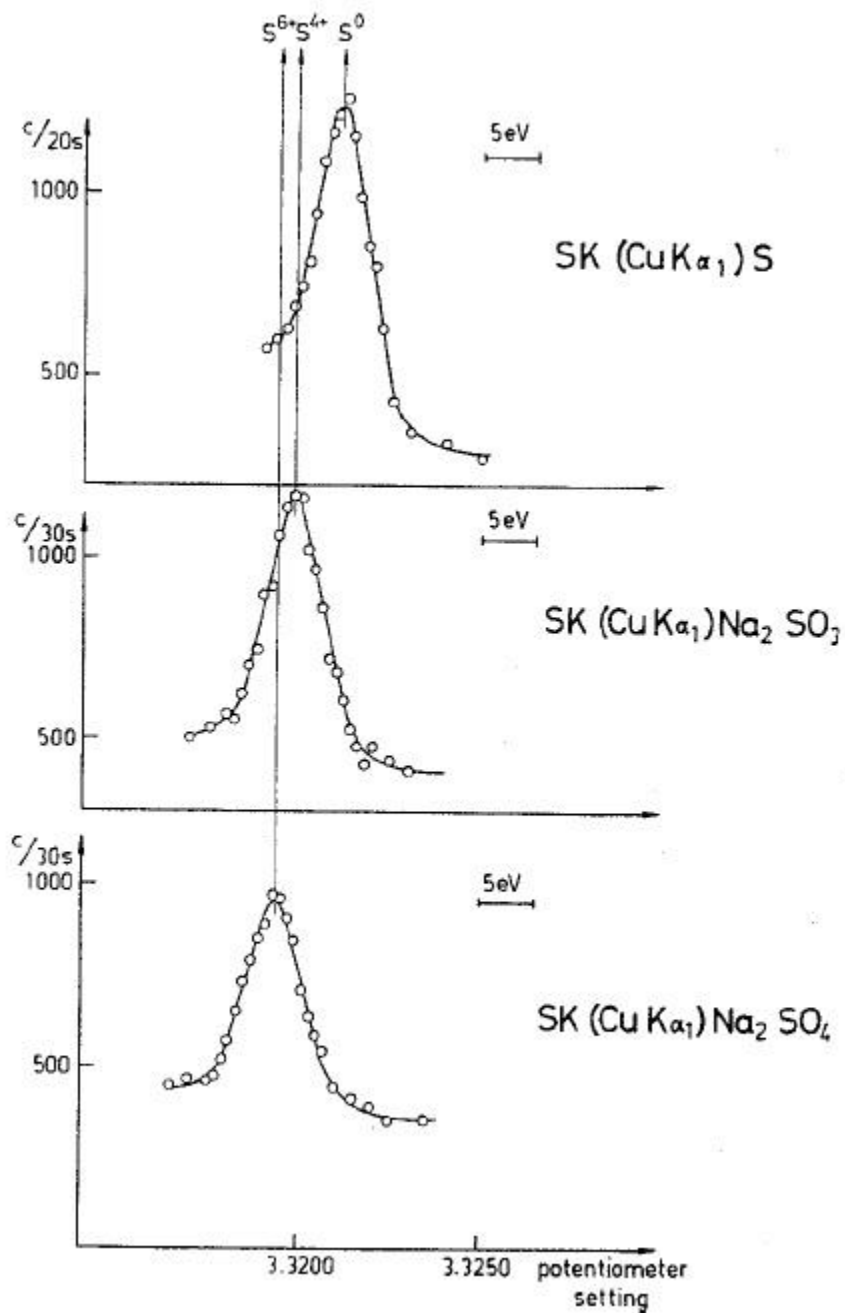


**Figure 17.** Surface and depth analysis by XPS. (74)

### Chemical shift in X-ray spectroscopy

The chemical shift reflects the influence of the chemical bonds with neighboring atoms. The chemical shift in the X-ray spectra is caused by changes in the electron binding energies. The more specific reason is as a result of the electro-negativity effect in the presence of another atom. For example, in the C-O bond, due to the electro-negativity of oxygen, C 2p electron in valence level will be attracted by atom O, and C 1s electron in core level will tend to be attracted by carbon nucleus so that the binding energy of C 1s electron will shift to higher binding energy.

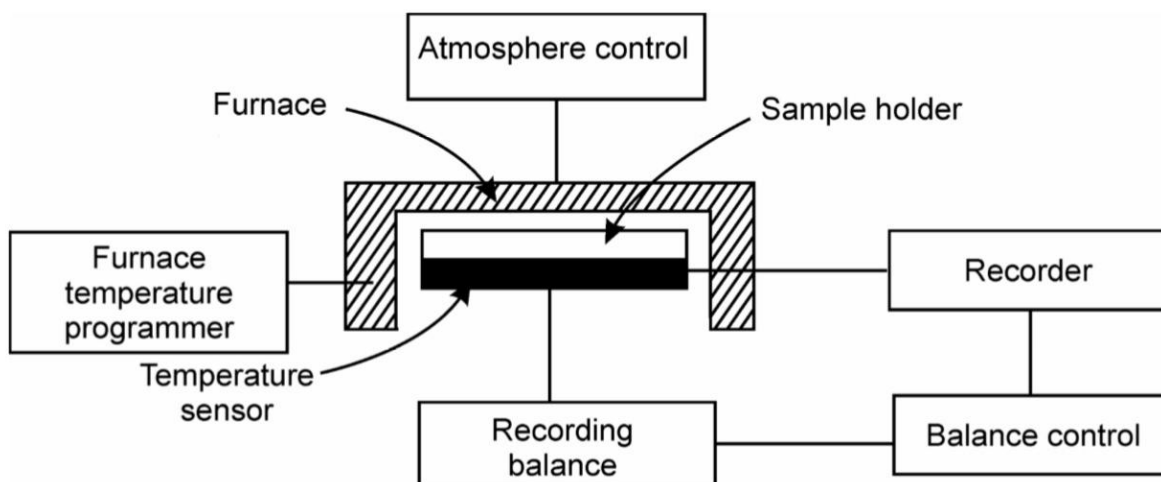
Therefore we shall here consider different ways of calculating the electron binding energy of an atom or a molecule, methods that can also be used to evaluate chemical shifts (75).



**Figure 18.** Affect of electron binding energy on chemical shifts. (66)

### 2.3.6 Thermogravimetric Analysis (TGA)

Thermogravimetric Analysis is a material characterization technique in which the mass of a substance is monitored as a function of temperature or time under controlled temperature and atmosphere. This analysis is carried out primarily to determine the composition of materials such as organic and inorganic content in the sample and to predict their thermal stability at high temperatures such as vaporization, sublimation, absorption, adsorption, desorption, chemisorption, reaction kinetics etc. A plot of mass change versus temperature, called thermogravimetric (TG) curve is plotted which helps in determining the extent of purity of analytical samples and the mode of their transformations within the specified temperature range.



**Figure 19.** Schematic view of thermogravimetric analysis

The furnace provides linear heating over a wide range of operating temperatures, room temperature up to 1000 °C depending on the requirement. Temperature measurement and regulation is done with the help of thermocouples. There are several factors that control the

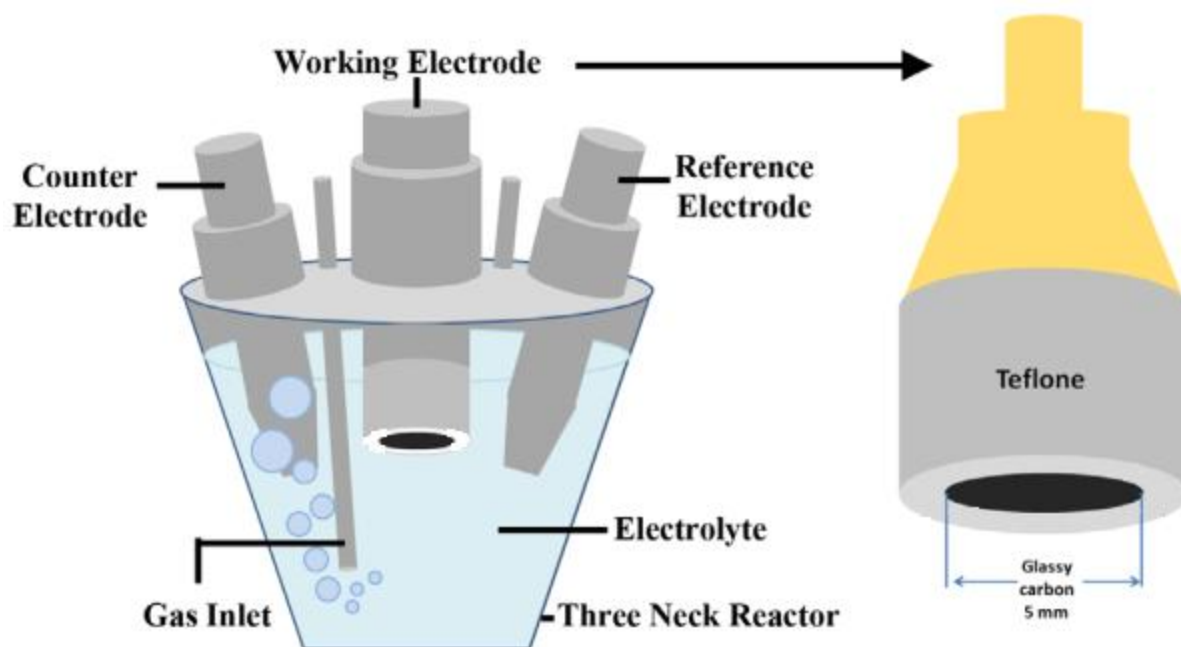
precision and accuracy of TG curves: heating rate, sensitivity of the sensors, amount of sample, particle size, heat of reaction etc.

All the above factors are to be taken into consideration and the instrument should be properly calibrated before performing experiments. It is a very efficient method in material characterization and is widely used in the analysis of polymers, plastics, composites, laminates, pharmaceuticals, rubber, petroleum, food, and adhesives. In this work TGA was used to analyse the composition of the organic and inorganic parts.

### **2.3.7 Half-Cell Electrochemical Evaluation**

Electrochemical performance of developed catalyst evaluated using half-cell electrochemical test. This test gives an easy and simple ways to assess the oxidation and reduction reaction. Thus, rotating disk electrode (RDE) measurements were used. In this case for reduction reaction linear sweep voltammeter and for oxygen evaluation cyclic voltammeter was used. The schematic view of the test is shown in Figure 888. During the test the reaction happens in electrolyte. This electrolyte is contained in three neck flask while the charges carried through it. Depending on the type of the voltammeter test oxygen (O<sub>2</sub>) or nitrogen (N<sub>2</sub>) gases are pumped into the electrolyte. The working electrode (RDE) is the main part of the half-cell test where the reactions happen. It consists of a glassy carbon which is held by teflon material. Teflon is very helpful for this use, because it is totally hydrophobic and helps during the coating ink. Rotating is very important for half-cell test, thus the working electrode is fixed with rotating electrode and the rotating speed is controlled during the test. To standardize the second half of the cell reference electrode is used with constant compound. There are many types of reference electrodes while some of them are more commonly used: standard hydrogen electrode (SHE), saturated calomel electrode (SCE), and silver-silver electrode (Ag/AgCl). At last, third important part for half-cell test is counter

electrode which is a pure platinum wire. This electrode creates RDE system which connected to potentiostat. Potentiostat adjusts voltage and at the same time reads and records current from working electrode. As it is mentioned, glass carbon on working electrode is covered with ink if testing sample. During the making ink it is very important to use hydrophobic binder with ethanol and sonicate the mixture to achieve good dispersion.

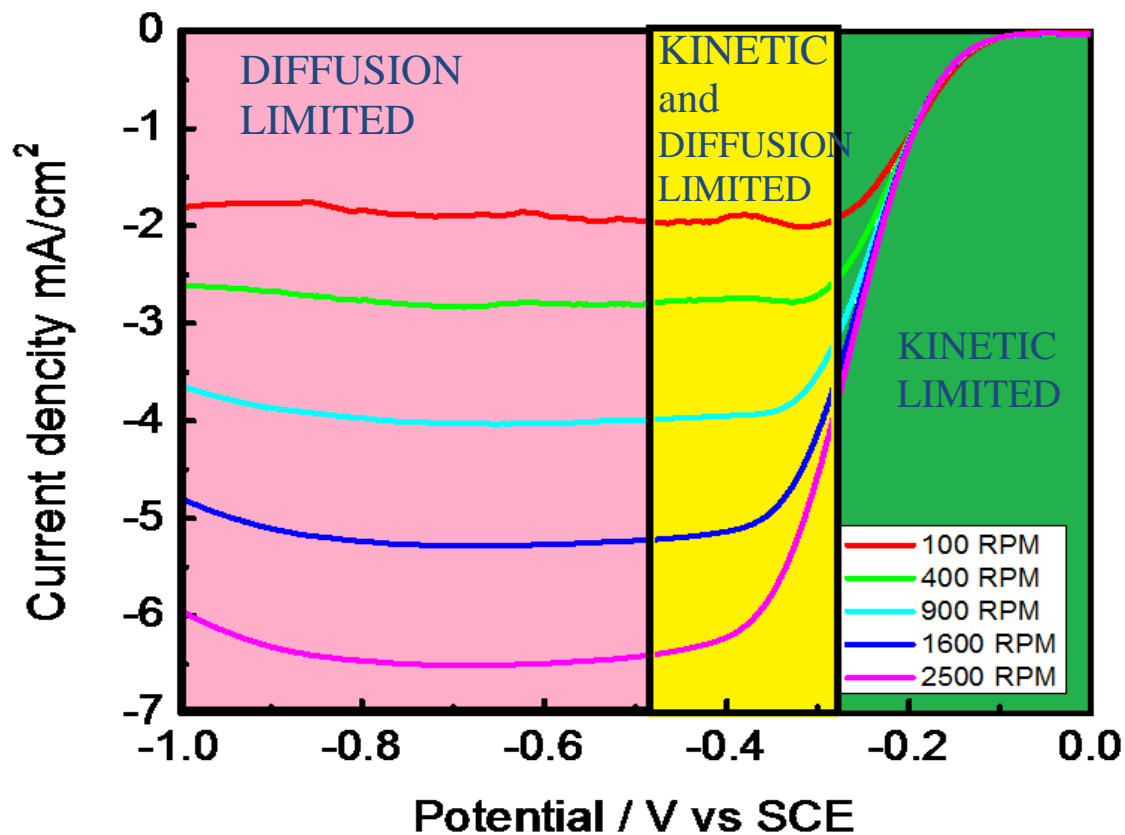


**Figure 20.** Schematic view of rotating disc electrode and working electrode. (73)

The RDE voltammetry test setup was followed as describe below. A 0.1 M KOH was used as alkaline electrolyte for half-cell electrochemical test . The test was done at room temperature and a Saturated Calomel Electrode (SCE) was used as reference electrode. A glassy carbon on working electrode was coated with 20  $\mu\text{L}$  of ink which made in 4 mg/mL concentration. For ink 4 mg of catalyst was sonicated with 1 mL of 0.3 wt. % Nafion in ethanol solvent. First electrochemical test is cyclic voltammetry (CV) which represents OER. By this method it is



possible to identify the capacity and the surface electrochemical kind of catalyst which had been coated on working electrode. These measurements are done at nitrogen flow, in 900 rpm, in a voltage range from 0 V to 1 V. The scan rate was 0.05 V/s and each test was done in 500 cycles. The second measurement is linear sweep voltammetry (LSV) which based on changing the potential over the time and recording the changes in current. For ORR test the scan rate was 0.01 V/s and the voltage interval was form 0.1 V to -1 V. During the test 5 different rotating speeds (100 rpm, 400 rpm, 900 rpm, 1600 rpm and 2500 rpm) were used. During the test the potential starts at positive and by time it goes down and during this process non-faradaic current at working electrode flows until it becomes similar to standard reduction potential. The reaction starts to happen when the potential gets closer to standard potential. Thus, the current will start to flow and this will be recorded by software. While the potential is dropping the concentration of oxygen at working electrode will decrease and the current will increase. As the potential continues to drop the potential moves far away from the standard potential, the concentration on the surface of the electrode becomes nearly zero and this means the maximum mass transformation of oxygen had been achieved. All this changes are shown in figure below.



**Figure 21.** ORR polarization of an active catalyst.

The data which is received from LSV is used for Koutecky-Levich (K-L) equation which is used to determine the number of electrons transferred at the surface of the electrocatalyst.

$$\frac{1}{j} = \frac{1}{j_k} + \frac{1}{j_L} \quad (16)$$

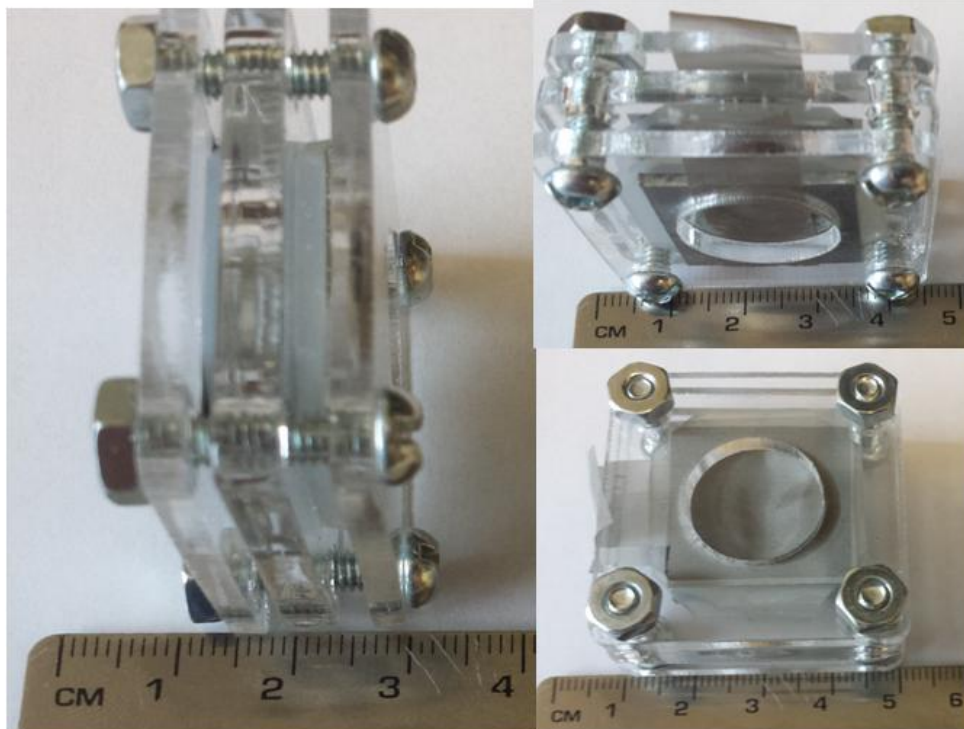
Where  $j$  is observed density,  $j_k$  is the kinetic current and  $j_L$  is limiting current density. The number of the electrons transferred is calculated per O<sub>2</sub> atom and it is shown with  $n$ :

$$j_L = 0.2nFD_0^{2/3}v^{-1/6}C_0\omega^{1/2} \quad (17)$$

Where,  $j_L$  is the limiting current density,  $F$  is the Faraday constant (96 485 C mol<sup>-1</sup>),  $D_0$  is the diffusion coefficient of O<sub>2</sub> (1.9 x 10<sup>-5</sup> cm<sup>2</sup> s<sup>-1</sup>) in 0.1 M KOH,  $\nu$  is the kinematic viscosity of 0.1 M KOH (0.01 cm<sup>2</sup> s<sup>-1</sup>), and  $C_0$  is the concentration of O<sub>2</sub> in the electrolyte (1.2 x 10<sup>-6</sup> mol cm<sup>-3</sup>). Parameter  $\omega$  represents different rotating speeds, as the result of this equation in the ideal conditions the number of transferred electrons need to be close to 4. Four electrons mean that during the reaction four-electron reduction of oxygen is happened.

### **2.3.8 Zinc-Air Battery Performance**

The electrochemical kinetic received from the half cell evolutions will be complimented by the CCBC catalyst zinc-air battery test. The battery test was performed using multichannel potentiostat with a lab designed battery. The schematic of the battery is shown below. Polished zinc metal is used as anode and for anode it is used catalyst coated gas diffusion layer (GDL). Microporous membrane was used as a separator and a 6M KOH as the electrolyte.



**Figure 22.** Schematic view single cell zinc-air battery setup.

### **3.0 Effect of Co Doping in to the LaMnO<sub>3</sub>**

#### **3.1 Introduction**

The performance of the battery depends on two types of reactions which are oxygen reduction reaction (ORR) and oxygen evolution reaction (OER), corresponding to discharge and charge process, respectively. Thus, for optimal battery performance it is important for each of these reactions to exhibit high performance. Good battery performance requires overcoming challenges related to the air cathode undergoing an sluggish ORR during charging and OER during discharging (76,77). These challenges can be solved through using highly active electrochemical catalysts. However, choosing the right catalyst is necessary as it will affect the cost, performance and lifetime of the battery.

A number of different electrochemical catalysts have been developed and tested for their application in fuel cell technology. The most effective catalyst in current technology stage are platinum (Pt) based catalysts, such as Pt, Pt-Au, Pt-Pd, and Pt/C (78-80). However there are several difficulties with this group of catalysts. First of all they are very expensive and easily degrade through platinum particle agglomeration, detachment and molecular poisoning, but also lack the ability to sufficiently catalyze an OER (81). All these challenges prevent rechargeable metal-air batteries from wide commercialization. It is clear that development of active, cheap and stable bi-functional catalyst is very important for wide commercialization of rechargeable metal-air batteries.

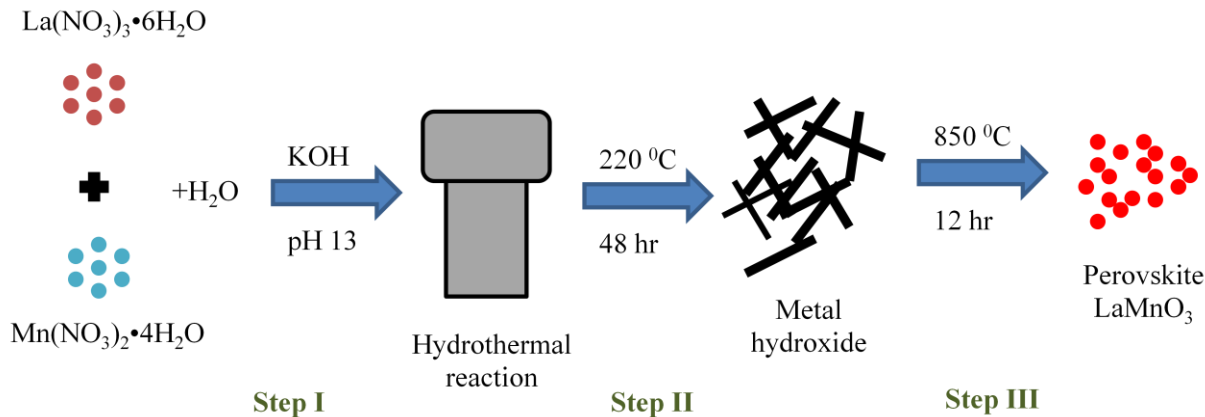
Different types of metal oxides have attracted much interest in past years because of their high electrochemical activity. Particularly, perovskite oxides have been suggested as promising candidates for bi-functional catalysts due to efficient ORR and OER reactions. Because of the first cation ordering, disorder-free channels are provided for oxygen vacancies to enhance the

mobility of oxygen ions (82-84). Among the perovskite oxides,  $\text{LaMnO}_3$  nanoparticle was prepared as a basic catalyst in this study due to its notable benefits such as low cost, environmental benignity, abundance and catalytic activity in aqueous electrolyte. Additionally, doping agents added to the perovskite catalyst materials in small amounts can improve their activity, selectivity and/or stability (85). Cobalt nanoparticles are expected to possess excellent magnetic, hardness and impact resistance properties. In addition, Co based nanocatalysts have attracted a great deal of attention in the past (86,87), where these nanocatalysts play important roles in the chemical industry. These improvements had been achieved in electrochemistry as well where doping different catalysts with Co shows better catalytic performance. Taking this knowledge as background we engendered to add Co to our catalyst.

## **3.2 Experimental**

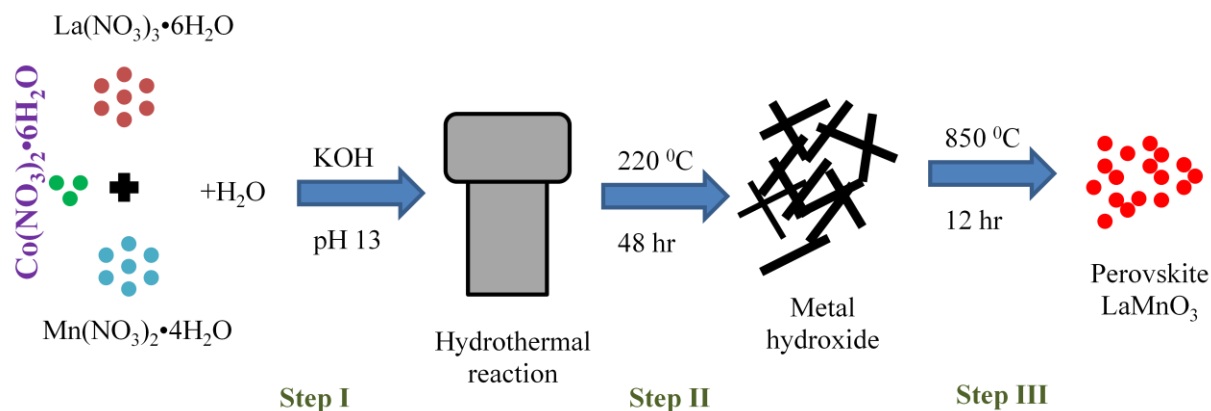
### **3.2.1 Synthesis**

Implementation of  $\text{LaMnO}_3$ : as described in Figure 23, the nano-sized perovskite lanthanum manganese oxide (ns- $\text{LaMnO}_3$ ) was synthesized using a hydrothermal method at 220 °C for 48 hr. 1 mmole of lanthanum nitrate hexahydrate ( $\text{La}(\text{NO}_3)_3 \cdot 6\text{H}_2\text{O}$ , Aldrich) and manganese nitrate hexahydrate ( $\text{Mn}(\text{NO}_3)_2 \cdot 6\text{H}_2\text{O}$ , Aldrich) was dissolved in 35 mL of de-ionized water. The pH of the mixture solution was adjusted to ~13 by the addition of 6.0 M potassium hydroxide (KOH, Aldrich). Then the solution was transferred into a Teflon-lined container in an autoclave. The autoclave was placed in a pre-heated oven at 220 °C and left for 48 hr. The resulting material was washed with de-ionized water and ethanol and collected by filtration followed by drying at 60 °C overnight. The product was ground and calcinated in air at 850°C for 12 hr. Lastly, ns- $\text{LaMnO}_3$  powder was obtained after further grinding.



**Figure 23.** Synthesis of  $\text{LaMnO}_3$

$\text{LaMn}_{0.9}\text{Co}_{0.1}\text{O}_3$ : the nano-sized perovskite lanthanum manganese oxide (ns-  $\text{LaMn}_{0.9}\text{Co}_{0.1}\text{O}_3$ ) was synthesized using a hydrothermal method at  $220\text{ }^\circ\text{C}$  for 48 hr. 1 mmole of lanthanum nitrate hexahydrate ( $\text{La}(\text{NO}_3)_3 \cdot 6\text{H}_2\text{O}$ , Aldrich), 0.9 mmole of manganese nitrate hexahydrate ( $\text{Mn}(\text{NO}_3)_2 \cdot 6\text{H}_2\text{O}$ , Aldrich) and 0.1 mmole Cobalt(II) nitrate hexahydrate ( $\text{Co}(\text{NO}_3)_2 \cdot 6\text{H}_2\text{O}$ ) was dissolved in 35 mL of de-ionized water. The pH of the mixture solution was adjusted to  $\sim 13$  by the addition of 6.0 M potassium hydroxide (KOH, Aldrich). Then, the solution was transferred into a Teflon-lined container in an autoclave. The autoclave was placed in a pre-heated oven at  $220\text{ }^\circ\text{C}$  and left for 48 hr. The resulting material was washed with de-ionized water and ethanol and collected by filtration followed by drying at  $60\text{ }^\circ\text{C}$  overnight. The product was ground and calcinated in air at  $850\text{ }^\circ\text{C}$  for 12 hr. Lastly, ns- $\text{LaMnO}_3$  powder was obtained after further grinding.



**Figure 24.** Synthesis of  $\text{LaMn}_{0.9}\text{Co}_{0.1}\text{O}_3$

### 3.2.2 Material characterization

Morphology and surface structure of  $\text{LaMnO}_3$  and  $\text{LaMn}_{0.9}\text{Co}_{0.1}\text{O}_3$  oxides were analysed by scanning electron microscopy (LEO FESEM 1530) and transmission electron microscopy (Philips CM300). The chemical composition of synthesized oxides was shown by an EDAX analyses technique. Crystal structure of oxides was examined by x-ray diffraction (Bruker AXS D8 Advance) in the range from  $5 - 70\ 2\theta$ .

### 3.2.3 Half-cell test

Rotating disk electrode (RDE) was used to evaluate the electrochemical performance of perovskite oxides which consist of a potentiostat (Pine Instrument Co, AFCBP - 1) and rotation speed controller (Pine Instrument Co, AFMSRCE). The working electrode in RDE consists of glassy carbon with a 5 mm outer diameter (OD). For this electrochemical test the catalyst must be coated on the working electrode. Thus before the test, 4 mg of catalyst was mixed with 0.3 w% of Nafion solution. The resulting mixture is called "catalyst ink" and was sonicated to

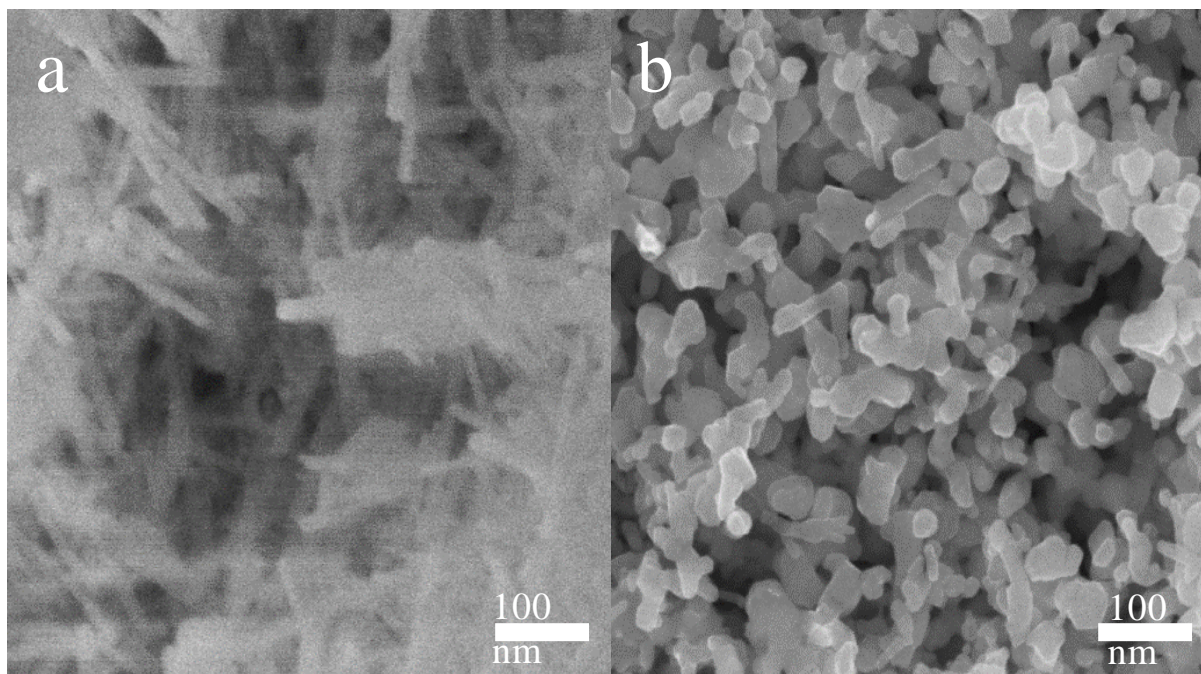


achieve excellent dispersion. For each test 20  $\mu\text{l}$  of ink was coated on to the working electrode, where the loading became  $0.408 \text{ mg/cm}^2$ . The resulting coat was inspected visually and then was immersed into 0.1 M KOH solution. KOH solution was used as the electrolyte environment. The reference and counter electrodes were submerged into the KOH solution too. Electrochemical activity towards the oxygen reduction reaction was evaluated from 0.2 V to -1 V vs Ag/AgCl. Before the ORR test the KOH electrolyte was saturated with  $\text{O}_2$ . Different rotating speeds at 100 rpm, 400 rpm, 900 rpm, and 1600 rpm were used at a scan rate of 10 mV/s. The stability of the catalysts was investigated by OER test in a voltage range 0 V to 1 V with a scan rate of 50 mV/s. Before the OER test a 900 rpm rotating speed was kept and the electrolyte was saturated with  $\text{N}_2$ .

### **3.3 Results and Discussion of $\text{LaMnO}_3$ and $\text{LaMn}_{0.9}\text{Co}_{0.1}\text{O}_3$**

#### **3.3.1 SEM and TEM**

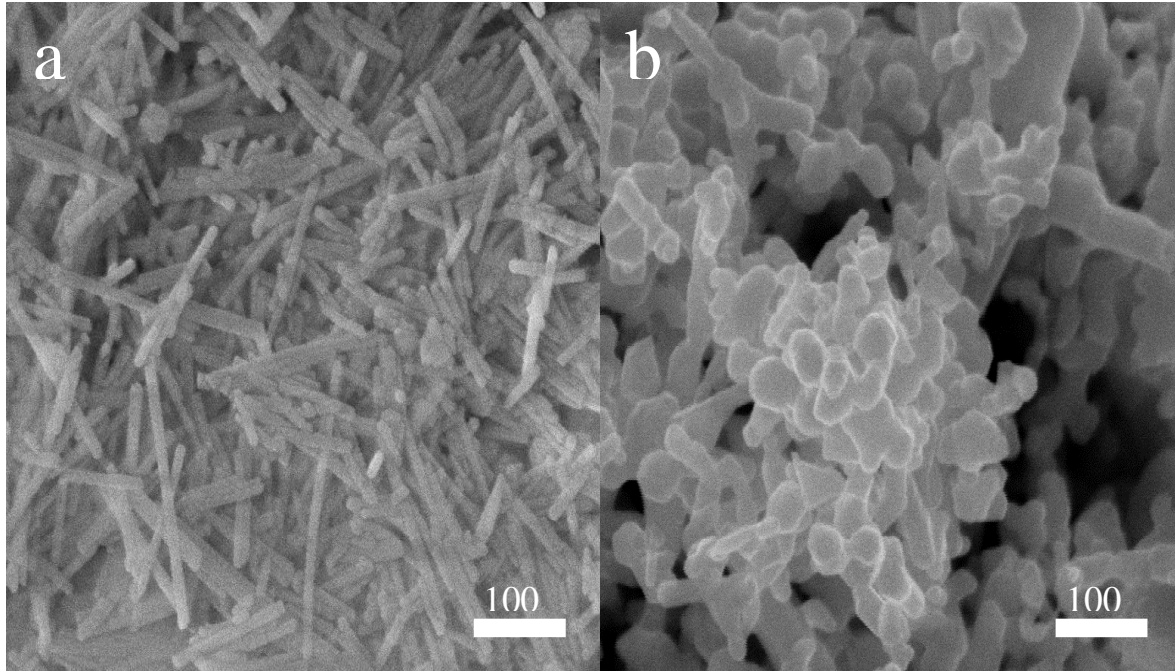
The morphology and crystallite phase of  $\text{LaMnO}_3$  and  $\text{LaMn}_{0.9}\text{Co}_{0.1}\text{O}_3$  collected powders after the hydrothermal reaction at  $220^\circ\text{C}$  for 48hr is examined by scanning electron microscope (SEM). In order to get a good quality image of  $\text{LaMnO}_3$  before calcination, gold sputtering was required due to the low conductivity of the uncalcined sample. The SEM image in Figure 25a shows the powders possess nano-rod shapes. It is assumed that this shape material consists of the metal hydroxides, the result of hydrothermal reaction before calcination. This technique is used to synthesise metal hydroxides with high surface area (88), typically rod-like shaped with sizes less than  $1 \mu\text{m}$ . From our observations, the size of rods are around 300-1000 nm in length with a diameter around 10-20 nm. SEM image was taken after calcination of powders at  $850^\circ\text{C}$  for 12 hours as shown in Figure 25b.



**Figure 25.** SEM images of  $\text{LaMnO}_3$  a) before calcination and b) after calcination

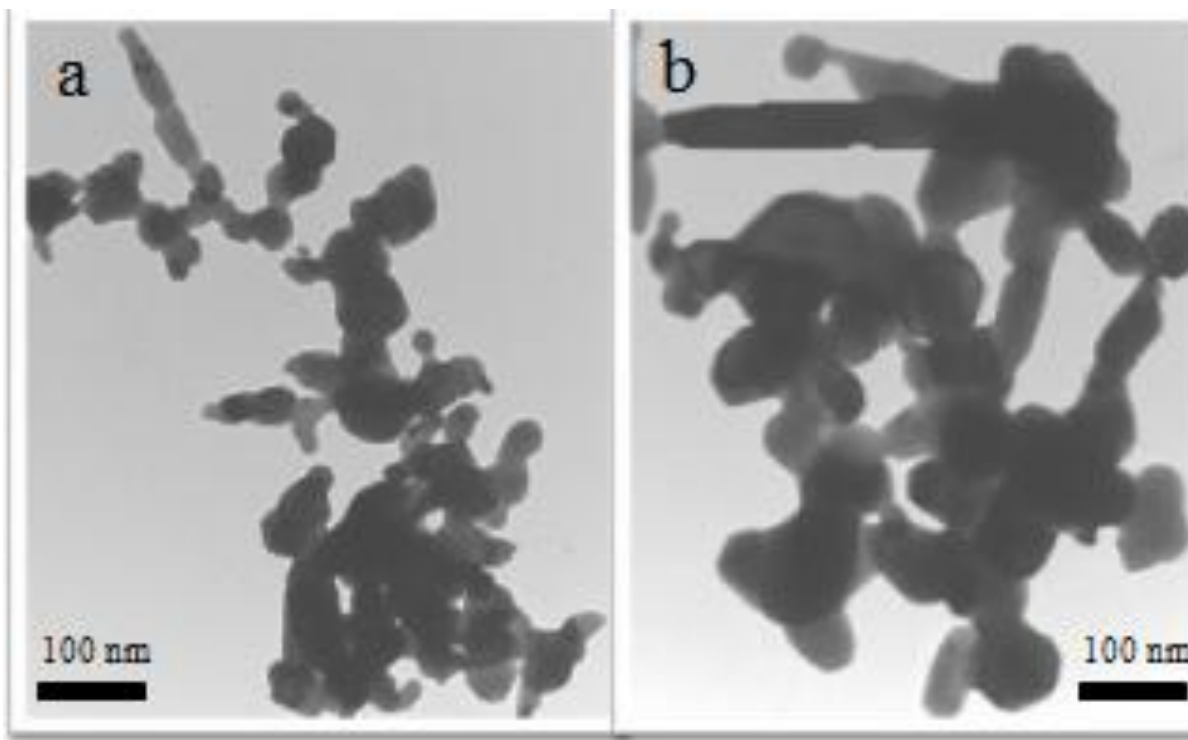
During the calcination at  $850\text{ }^{\circ}\text{C}$  La and Mn hydroxides react to form a stable composition. Specifically for La, Mn and O due to the composition's perovskite structure crystals sizes were in the range of 50-150 nm. This shows that through heat treatment the surface area of the material increases due to the decomposition of the metal hydroxide to metal oxide.

By using the same technique  $\text{LaMn}_{0.9}\text{Co}_{0.1}\text{O}_3$  was synthesized. SEM images as shown in Figure 26 were observed for the sample before and after calcination. The results were similar to those of  $\text{LaMnO}_3$ . The powder, which dried after hydrothermal reaction, shows a similar nano-rod shape. However, after calcination nano-crystals with a size range from 100-200 nm were observed. These are the perovskite type oxide particles where 10% of Mn was replaced with Co to increase electrochemical performance.



**Figure 26.** SEM images of  $\text{LaMn}_{0.9}\text{Co}_{0.1}\text{O}_3$  a) before calcination and b) after calcination

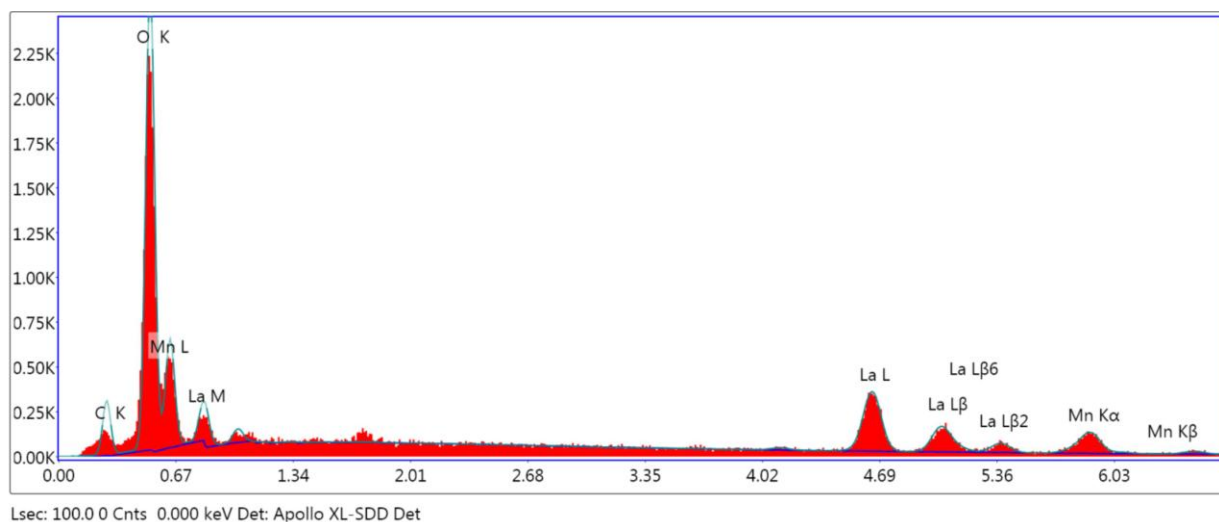
To observe the oxides crystal size and shape more precisely a TEM analyses technique was used. The results are shown in Figure 27. The results were similar with SEM images with a size ranging from 50-150 nm, but TEM images prove that a few particles are connected each other. These observations were a result of using high temperature for heat treatment to experience agglomeration of crystals.



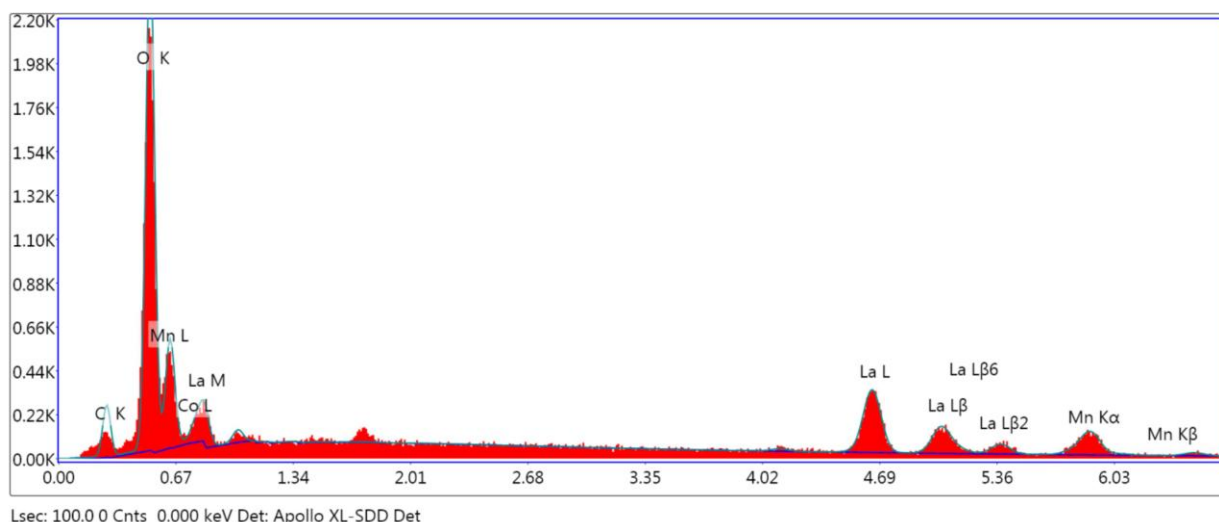
**Figure 27.** TEM analyses for a)  $\text{LaMnO}_3$  and b)  $\text{LaMn}_{0.9}\text{Co}_{0.1}\text{O}_3$ .

### 3.3.2 EDAX

The chemical composition of synthesized oxides were additionally analysed through EDAX.  $\text{LaMnO}_3$  results are shown in Figure 28. These results prove that the oxide consists of La, Mn and O elements. Following doping Co in the  $\text{LaMnO}_3$  composite, the synthesized  $\text{LaMn}_{0.9}\text{Co}_{0.1}\text{O}_3$  oxide was analysed by the same EDAX technique. These EDAX results are shown in figure 29. The same peaks as  $\text{LaMnO}_3$  are observed for the elements La, Mn and O. An extra peak for Co was also observed, however the peak for Co overlaps with La and thus is not visibly separate. Instead, the single La and Co peak combined forms a wider peak when comparing to the peak for La.



**Figure 28.** EDX analyses for  $\text{LaMnO}_3$

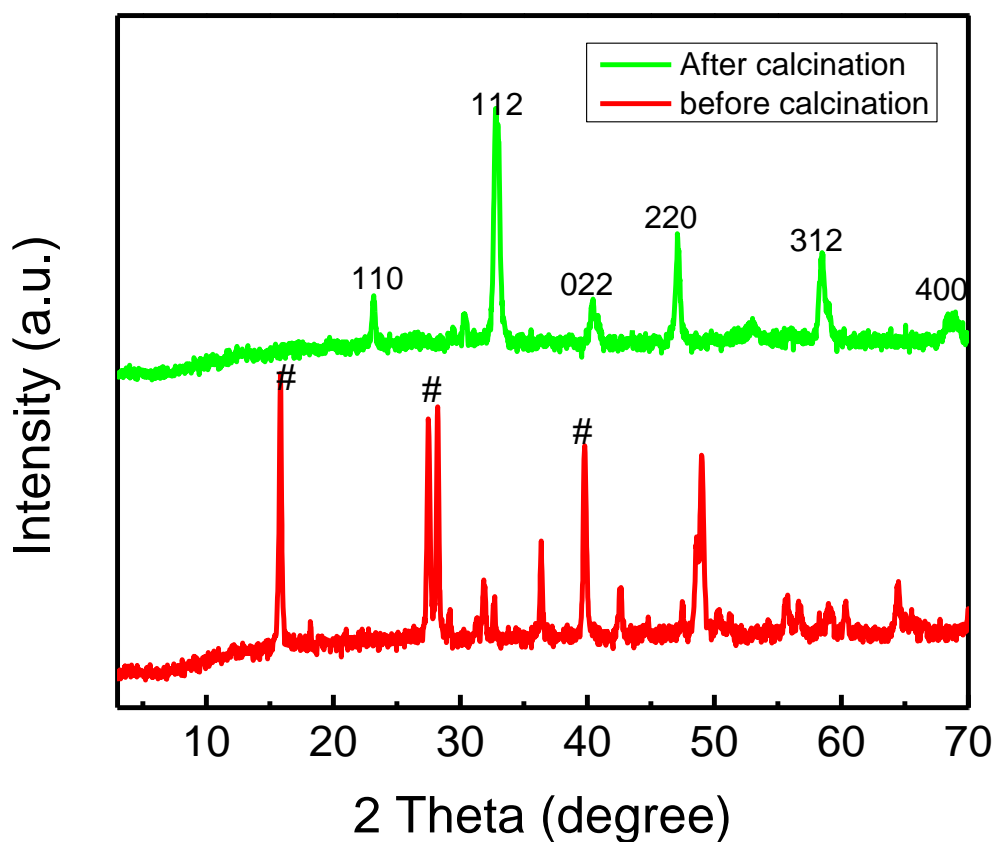


**Figure 29.** EDX analyses for  $\text{LaMn}_{0.9}\text{Co}_{0.1}\text{O}_3$

### 3.3.3 XRD

X-ray diffraction analysis was used to do crystallographic analyses of  $\text{LaMnO}_3$  and  $\text{LaMn}_{0.9}\text{Co}_{0.1}\text{O}_3$ . To make sure that the synthesized  $\text{LaMnO}_3$  had the crystalline perovskite oxide, the XRD analyses operated before and after calcination of the samples. In the first image an XRD pattern is shown for  $\text{LaMnO}_3$ . During the hydrothermal reaction metal nitrates were mixed

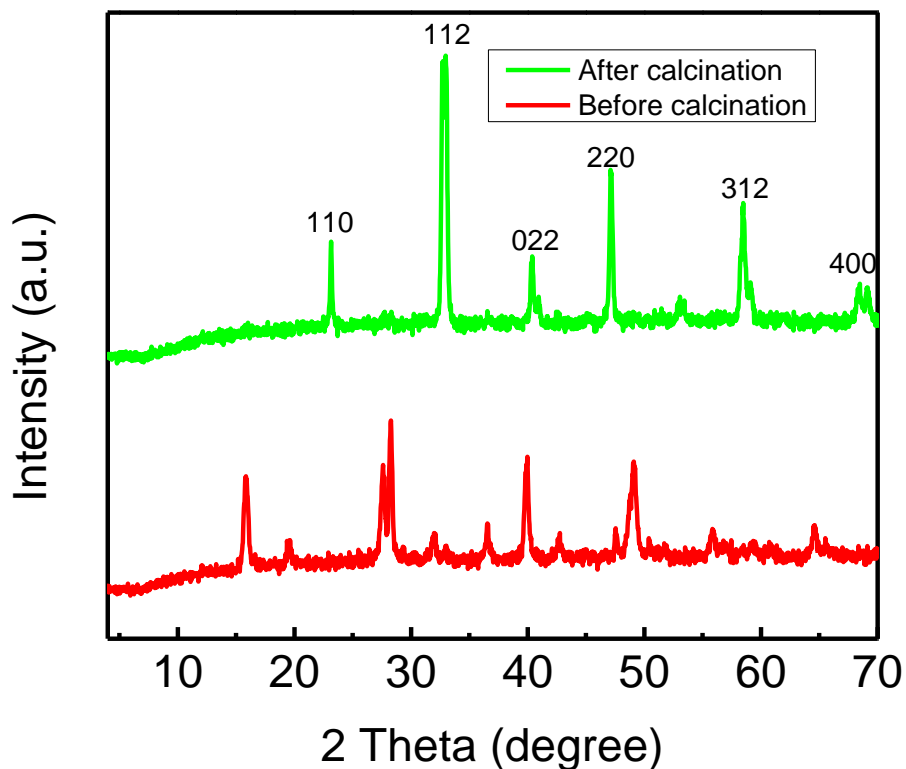
and the result sample contains La and Mn hydroxides. The peaks like 16, 28 and 39 degree shown in pattern for the sample before calcination are the degrees related to hydroxides in figure 30 (#). However, the results after calcination gave the same peaks which matches the peaks for perovskite oxides (23, 32.5, 41, 47, 58.5 and 68.65 degree). This proves that we have synthesised the  $\text{LaMnO}_3$  perovskite oxide.



**Figure 30.** XRD analyses for  $\text{LaMnO}_3$

Furthermore, the same synthesis method was used to dope  $\text{LaMnO}_3$  with Co. This composition is a perovskite oxide, thus it should display the same XRD pattern. Figure 31 shows XRD results

for  $\text{LaMn}_{0.9}\text{Co}_{0.1}\text{O}_3$  before and after calcination. Calcinated  $\text{LaMn}_{0.9}\text{Co}_{0.1}\text{O}_3$  oxide has the same XRD peaks as  $\text{LaMnO}_3$  which means that  $\text{LaMn}_{0.9}\text{Co}_{0.1}\text{O}_3$  oxide has perovskite structure.



**Figure 31.** XRD analyses for  $\text{LaMn}_{0.9}\text{Co}_{0.1}\text{O}_3$

### 3.3.4 Half-cell test

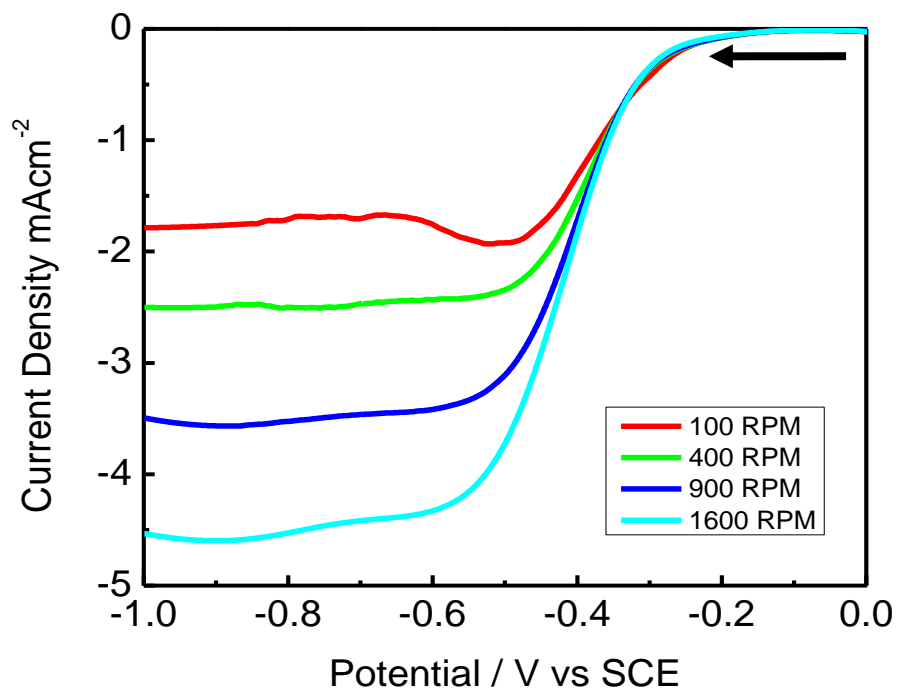
The electrocatalytic activity for ORR and OER of  $\text{LaMnO}_3$  and  $\text{LaMn}_{0.9}\text{Co}_{0.1}\text{O}_3$  was analysed by rotating disc electrode (RDE) voltammetry using potentiostat (CH Instrument 760D). During these tests, the rotating electrode speed was controlled by a Pine Instrument Co, AFMSRCE.

Before investigating the  $\text{LaMnO}_3$  catalyst's electrochemical performance it is imperative to prepare a proper ink solution. 4 mg of  $\text{LaMnO}_3$  powder was mixed with 0.3 w% of Nafion and the solvent was sonicated for 2 hours. It is very important that after sonication the catalyst was

well dispersed in Nafion as the dispersion affects the integrity of the coating of ink on the working electrode. 20  $\mu\text{L}$  of ink (loaded at  $0.408 \text{ mg cm}^{-2}$ ) was coated on the glassy carbon surface of the working electrode. When dried, the working electrode and ink coating were immersed into a 0.1 M KOH electrolyte with other two reference and counter electrodes.

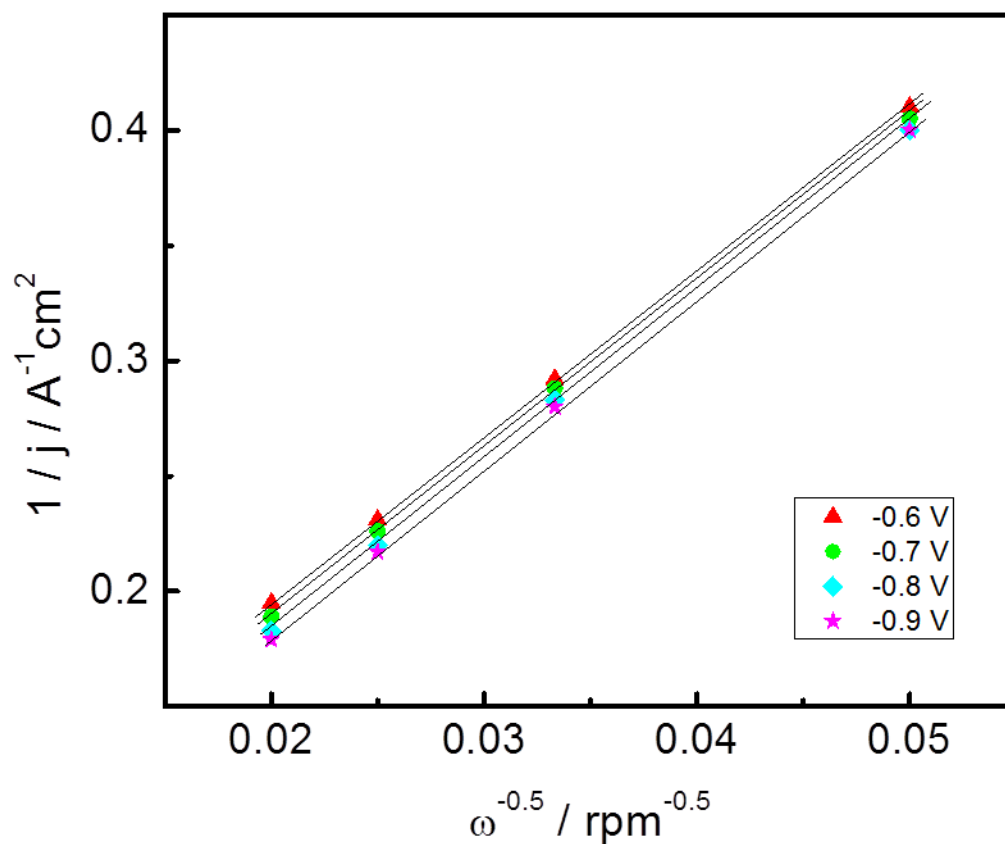
The half-cell test began with activation of the catalyst by cyclic voltammetry (CV) and thus the electrolyte was saturated with nitrogen ( $\text{N}_2$ ) gas which pumped through the electrolyte for 30 minutes. When the cycling achieves equilibrium the test switched to linear sweep voltammetry (LSV) to record the data for background which will be later be removed from the ORR data. After recording this background the gas was switched to oxygen ( $\text{O}_2$ ) gas and bubbled for 30 minutes to both remove  $\text{N}_2$  from the electrolyte and saturate it with nitrogen. The ORR test was performed at different rotating speeds using the LSV method. When all the data for ORR was collected, the gas switched back to  $\text{N}_2$  again and was left saturating for 30 minutes. At the end of this period of time the OER test was performed by using CV technique at a speed of 900 rpm. Sample ORR results for the performance of  $\text{LaMnO}_3$  at 100 rpm, 400 rpm, 900 rpm and 1600 rpm is shown in Figure 32.





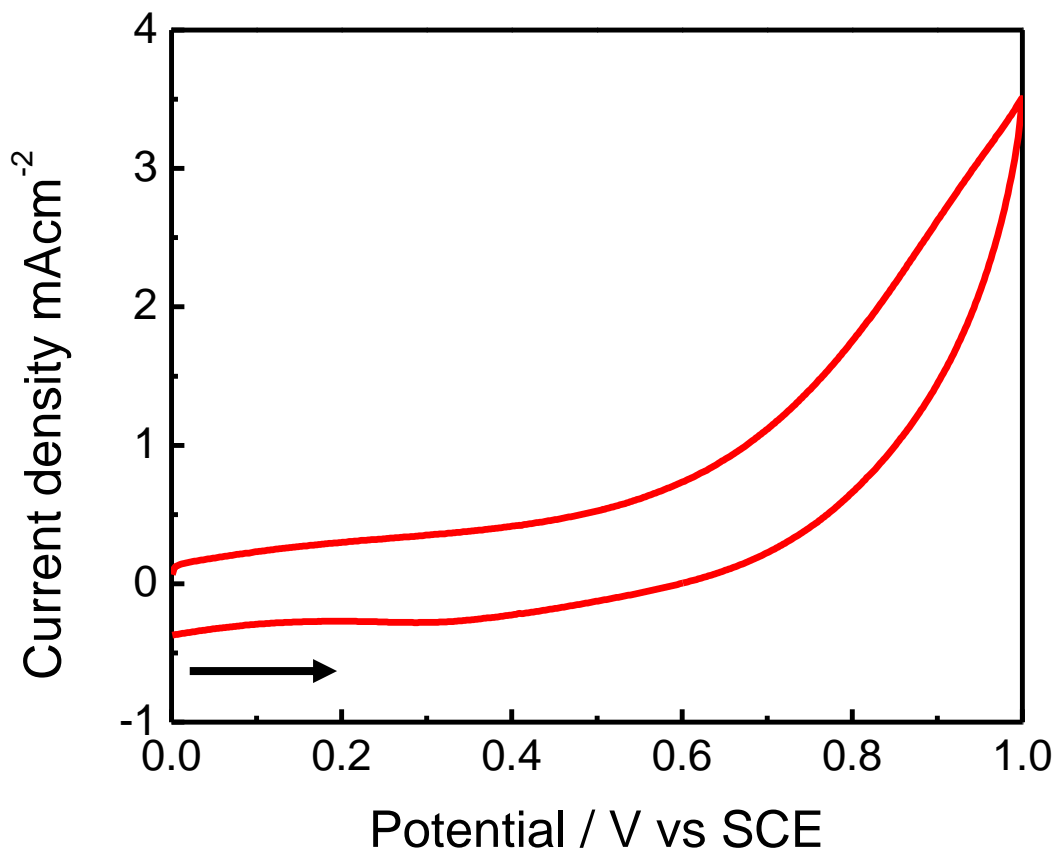
**Figure 32.** ORR performance for LaMnO<sub>3</sub>

Based on ORR results at different rotating speed a Koutecky-Levich (KL) plot was calculated to confirm the number of electron involved in the reaction. The results show in figure 33, for -0.6, -0.7, -0.8 and -0.9 voltages. The results of these calculations show that the number of electrons transferred is 3.6, 3.6, 3.6 and 3.7 respectively which indicating the ORR catalytic activity based on ORR reaction equation ( $O_2 + 2H_2O + 4e^- \rightarrow 4OH^-$ ).



**Figure 33.** Koutecky - Levich plot for LaMnO<sub>3</sub>

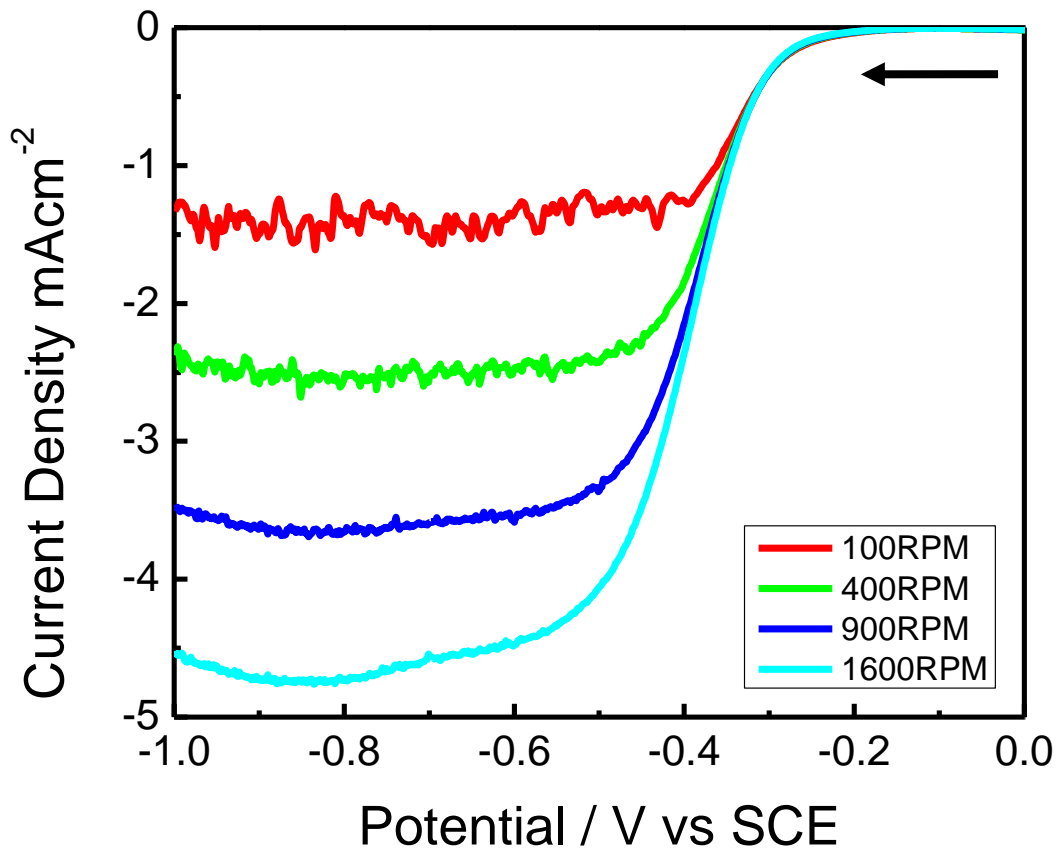
The OER test was performed in N<sub>2</sub>-saturated 0.1M KOH electrolyte in 0 V ~ 1.0 V (vs. SCE) of potential range and monitored anodic current density change as shown in Figure 34. The current density was measured at 3.5 mAcm<sup>-2</sup> which is negligible OER activity.



**Figure 34.** OER performance for LaMnO<sub>3</sub>

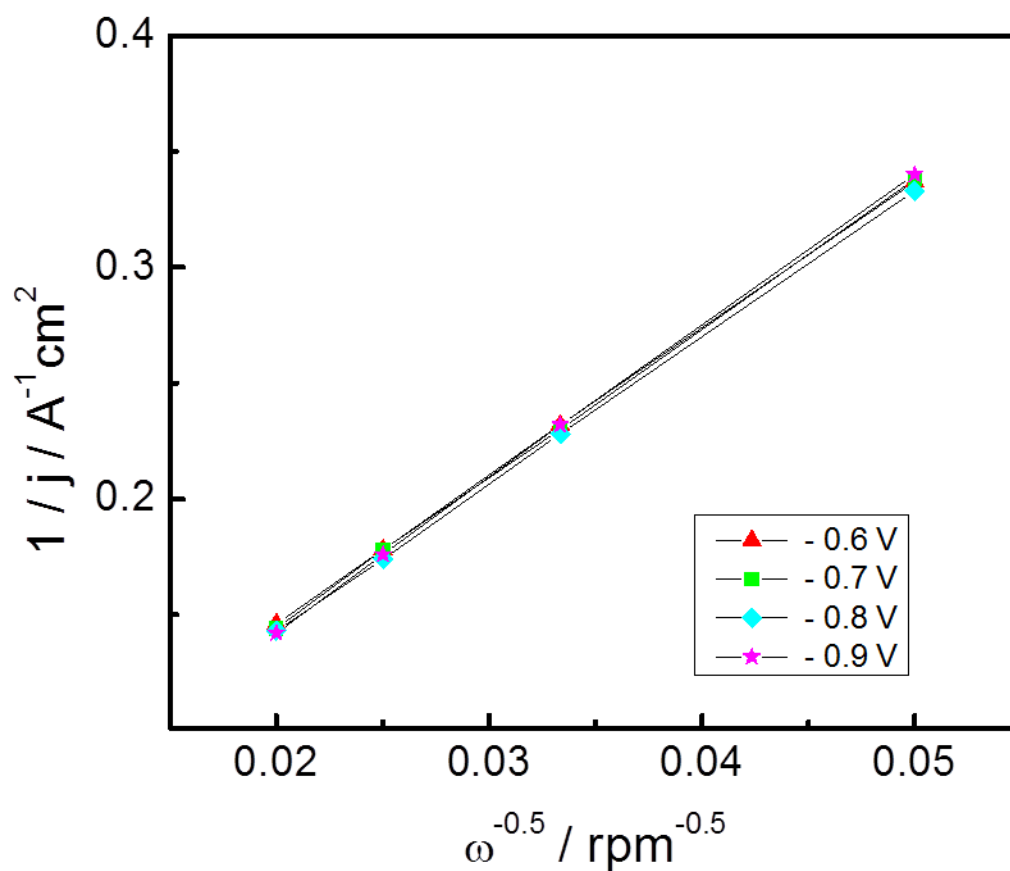
The electrochemical performance of LaMn<sub>0.9</sub>Co<sub>0.1</sub>O<sub>3</sub> was similarly tested by CV and LSV techniques. Preparation for the RDE test was the same as described for LaMnO<sub>3</sub>. Briefly, 4 mg of LaMn<sub>0.9</sub>Co<sub>0.1</sub>O<sub>3</sub> powder was mixed with 0.3 w% of Nafion and the solvent was sonicated for 2 hours. Then 20  $\mu$ L of ink (loading 0.408 mgcm<sup>-2</sup>) was coated on the glassy carbon surface of the working electrode. When the ink was dried the working electrode was immersed into 0.1 M KOH electrolyte with other two reference and counter electrodes. The half-cell test activation is done in N<sub>2</sub>, therefore the electrolyte solution was saturated with pumped N<sub>2</sub> for 30 minutes. When the cycling achieves equilibrium, the test switched to LSV to record the data for back

ground which will be later removed from the ORR data. After recording back ground the gas was switched to O<sub>2</sub> and bubbled for 30 minutes to both remove N<sub>2</sub> from the electrolyte and saturate it with O<sub>2</sub>. The ORR test was performed at different rotating speeds using the LSV method. When all the data for ORR was collected, the gas switched back to N<sub>2</sub> again and was left saturating for 30 minutes. At the end of this period of time the OER test was performed by using CV technique at a speed of 900 rpm. The ORR results for the performance of LaMn<sub>0.9</sub>Co<sub>0.1</sub>O<sub>3</sub> at 100 rpm, 400 rpm, 900 rpm and 1600 rpm is shown in Figure 35.



**Figure 35.** ORR performance for LaMn<sub>0.9</sub>Co<sub>0.1</sub>O<sub>3</sub>

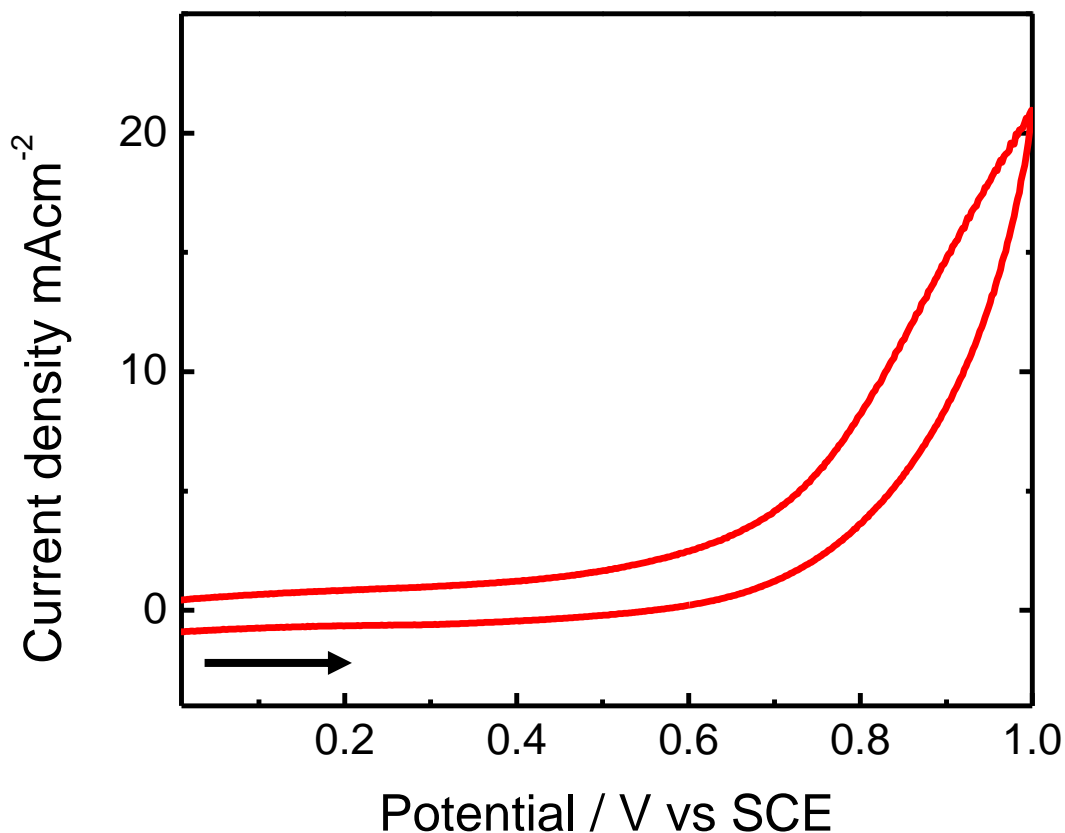
Based on ORR results at different rotating speed a KL plot was calculated. The results shown in figure 36, for -0.6, -0.7, -0.8 and -0.9 voltages. The results of these calculations show that the number of electrons transferred is 3.7, 3.8, 3.8 and 3.9 respectively. Compared to the performance of  $\text{LaMnO}_3$ , it is suggested that the Co-doped  $\text{LaMnO}_3$  slightly improves ORR activity.



**Figure 36.** Koutecky - Levich plot for  $\text{LaMn}_{0.9}\text{Co}_{0.1}\text{O}_3$

The OER test was performed in  $\text{N}_2$ -saturated 0.1M KOH electrolyte in 0 V ~ 1.0 V (vs. SCE) of potential range and monitored anodic current density change as shown in Figure 37. The current

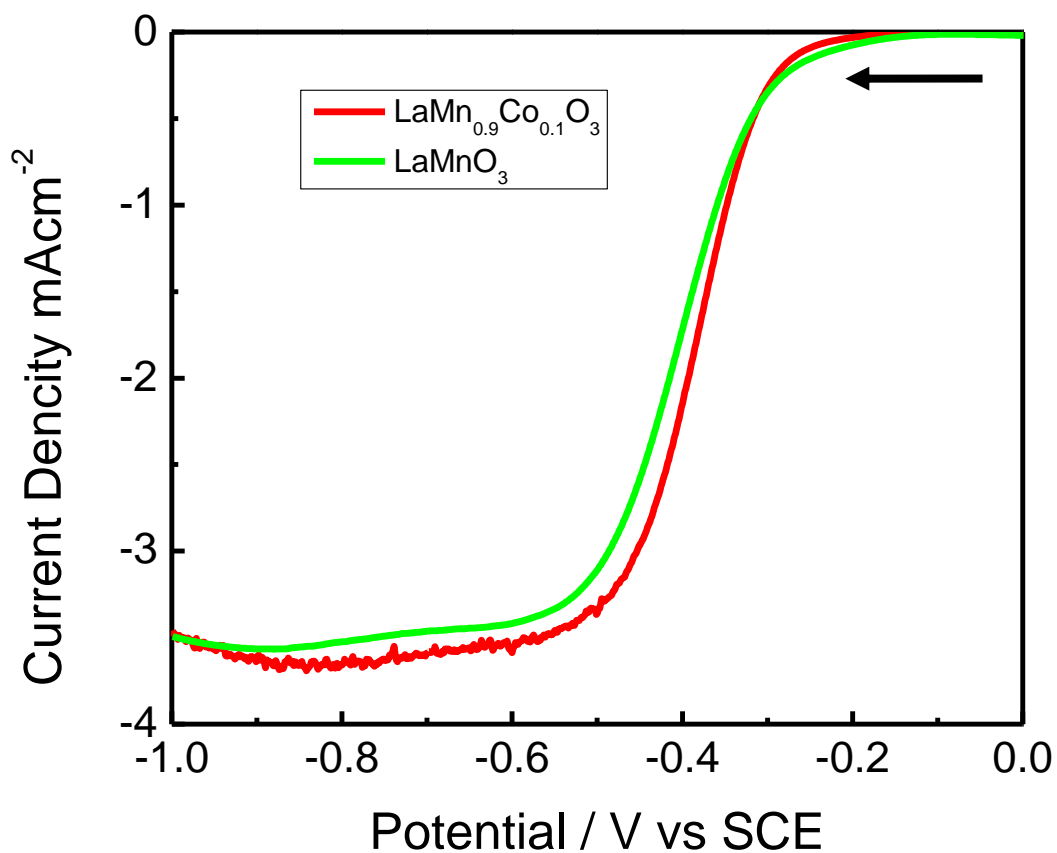
density of  $\text{LaMn}_{0.9}\text{Co}_{0.1}\text{O}_3$  was  $21.5 \text{ mAcm}^{-2}$  at  $1.0 \text{ V}$  indicating the OER activity after Co doping dramatically improves compare to that of  $\text{LaMnO}_3$ ..



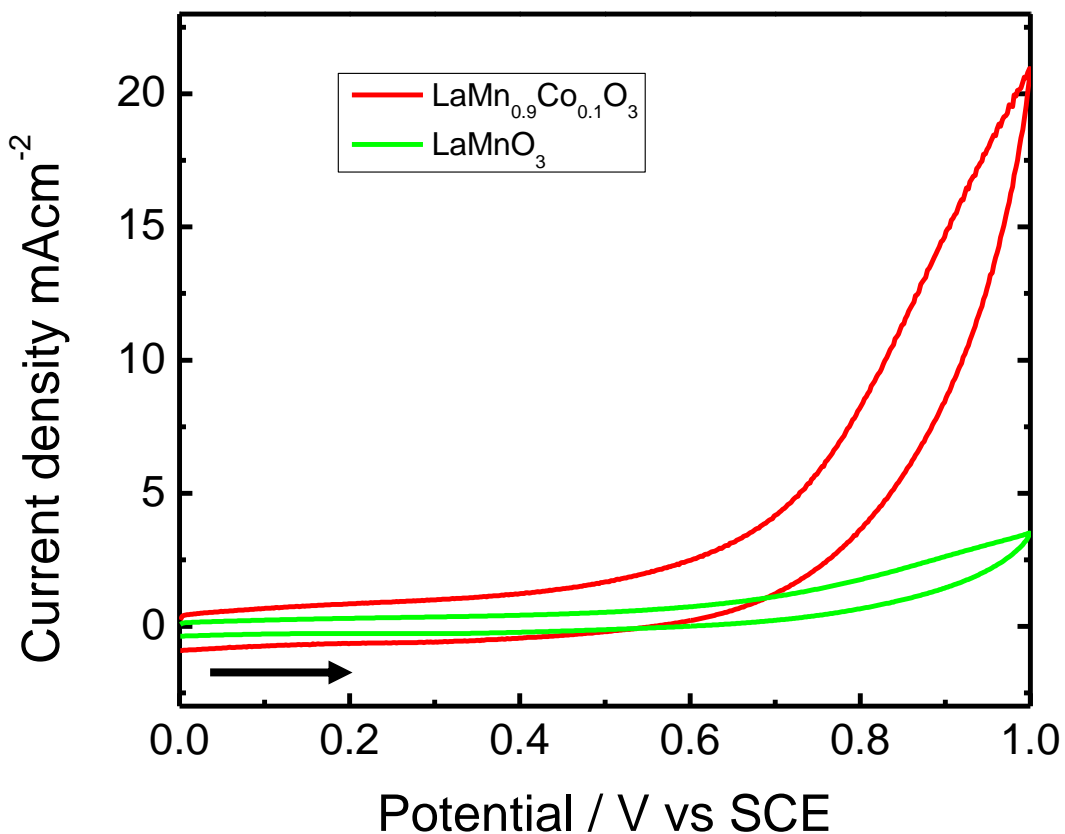
**Figure 37.** OER performance for  $\text{LaMn}_{0.9}\text{Co}_{0.1}\text{O}_3$

ORR and OER performances of  $\text{LaMnO}_3$  and  $\text{LaMn}_{0.9}\text{Co}_{0.1}\text{O}_3$  were directly compared to see the improvement in the performance in figure 38. The 900 rpm rotating ORR results are shown in the figure for the both catalysts. The half-wave potential for  $\text{LaMn}_{0.9}\text{Co}_{0.1}\text{O}_3$  and  $\text{LaMnO}_3$  is  $-0.37 \text{ mAcm}^{-2}$  and  $-0.39 \text{ mAcm}^{-2}$ , respectively. While this shows a small increase in catalytic performance due to Co doping, the activity seems still low to be applied for metal air battery

applications. A comparison of the results for OER performance of  $\text{LaMnO}_3$  and  $\text{LaMn}_{0.9}\text{Co}_{0.1}\text{O}_3$  is shown in Figure 29 demonstrating excellent improvement from Co-doping. It is anticipated that  $\text{LaMn}_{0.9}\text{Co}_{0.1}\text{O}_3$  can be a good catalyst for OER performance. In future research this type of oxides combined with other ORR catalysts should increase the overall performance of the battery as a bifunctional catalyst.



**Figure 38.** ORR performance of  $\text{LaMnO}_3$  vs.  $\text{LaMn}_{0.9}\text{Co}_{0.1}\text{O}_3$  at 900 rpm



**Figure 39.** OER performance of  $\text{LaMnO}_3$  vs.  $\text{LaMn}_{0.9}\text{Co}_{0.1}\text{O}_3$

### 3.4 Conclusion

In this section a simple technique has been provided for synthesizing perovskite oxides nanoparticles and improving their electrochemical performance by doping with other metals in small amounts. By using different morphology analysis techniques it is shown that perovskite oxides are able to retain their morphology even after doping with metals. Further electrochemical analyses of  $\text{LaMnO}_3$  and  $\text{LaMn}_{0.9}\text{Co}_{0.1}\text{O}_3$  show that Co doping provides no significant improvement in ORR performance. However, OER performance was changed greatly. Primarily, the current density was notably increased from  $3.5 \text{ mAcm}^{-2}$  to  $21.5 \text{ mAcm}^{-2}$ . This means that the



performance of the battery will be improved by using  $\text{LaMn}_{0.9}\text{Co}_{0.1}\text{O}_3$  in comparison to  $\text{LaMnO}_3$ . Furthermore, it is expected once the catalyst combines with ORR catalyst, it will be an excellent bifunctional catalyst.

## 4.0 Combining Co Doped Oxides with NCNT

### 4.1 Introduction

Tremendous efforts have been made towards the development of non-noble metal catalysts to replace the expensive platinum catalysts for the ORR critical reaction for metal-air batteries. Nitrogen doping of carbon nano tubes (CNTs) has shown great promise as a contender to platinum based catalysts for ORR catalysis based on several computational and experimental studies (73,81). It has been demonstrated that nitrogen doping on the surface of the carbon was an essential requirement to obtain non-noble metallic-based catalytic sites. One notable paper proposed that the catalytic activity observed on NCNT is attributed to two different active sites. A second research group attributes the source of the ORR activity in NCNT to surface nitrogen in the form of pyridinic and pyrrolic/pyridone-type nitrogen groups (89,90). Regardless of the mechanism, both confirmed a heightened level of ORR activity when integrating nitrogen.

Zhu Chen et al. reported a novel class of core-corona bifunctional catalyst (CCBC) (81). This catalyst consists of highly ORR active nitrogen doped carbon nanotubes (NCNT) combined with highly OER active  $\text{LaNiO}_3$  perovskite oxide to form a chemically and mechanically stable composite. NCNT is observed as the corona of this bifunctional catalyst while  $\text{LaNiO}_3$  is the core material. This work cumulatively was an in-depth study on improvements of the bi-functional catalytic activities, clearly demonstrating the effectiveness of directly growing NCNT on the surface of  $\text{LaNiO}_3$  in order to create a highly active and durable cathode material for rechargeable applications (91).

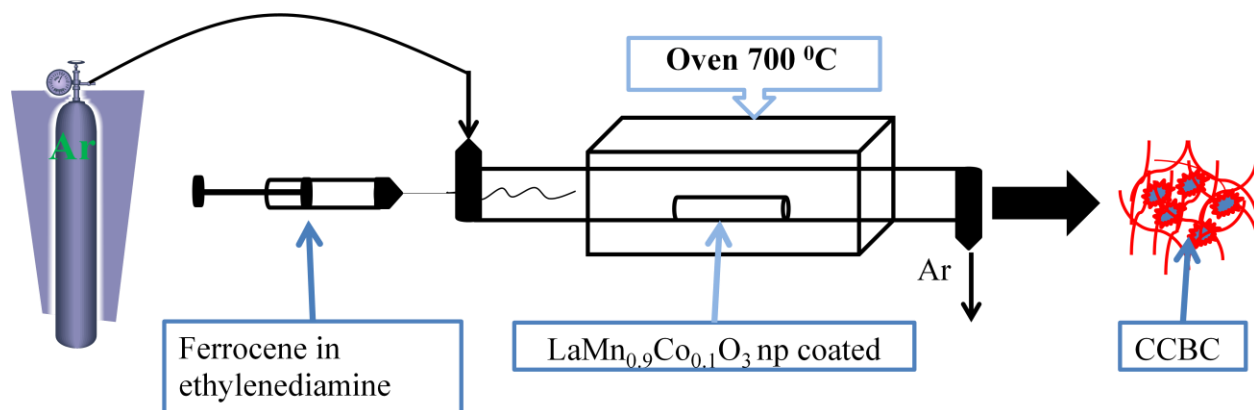
Based on all this information it was decided that the combination of NCNT with synthesized  $\text{LaMn}_{0.9}\text{Co}_{0.1}\text{O}_3$  oxide had the potential to outperform previously synthesized bi-functional catalysts. While this novel oxide has the same perovskite type structure as  $\text{LaNiO}_3$ , the developed

perovskite oxide in this study is prepared by hydrothermal reaction to obtain nano-sized particles. Based on this material similarity it has been proposed that combining NCNT with  $\text{LaMn}_{0.9}\text{Co}_{0.1}\text{O}_3$  will increase the both of electrochemical performance for ORR and OER while remaining mechanically stable.

## **4.2 Experimental for Synthesis of CCBC bifunctional catalyst**

### **4.2.1 Synthesis**

A chemical vapour deposition (CVD) method was used in preparation of the core-corona structure. Thus, in preparation to produce our new variant of CCBC, obtained ns- $\text{LaMn}_{0.9}\text{Co}_{0.1}\text{O}_3$  was incorporated with NCNT by using an injection CVD method. 20 mg ns- $\text{LaMn}_{0.9}\text{Co}_{0.1}\text{O}_3$  was dispersed in 0.3 wt% ferrocene ( $\text{C}_{10}\text{H}_{10}\text{Fe}$ , Aldrich) in ethanol by sonication and the mixture was casted on the inside wall of a small quartz tube (18 mm O.D., 100 mm length). The small tube with the coated mixture was placed into a horizontal tube furnace. In order to synthesize NCNT in this injection CVD, 2.5 wt% ferrocene in ethylenediamine ( $\text{C}_2\text{H}_8\text{N}_2$ , Aldrich) solution was prepared as a precursor and 2 ml of the precursor solution was loaded into a syringe. The precursor solution was injected into the tube furnace at  $0.05 \text{ mLmin}^{-1}$  at  $700 \text{ }^\circ\text{C}$  in an Ar atmosphere at a flow rate of 100 sccm. After injection, the furnace was cooled down to room temperature, followed by collecting final product ns-CCBC.



**Figure 40.** Synthesis of CCBC

#### 4.2.2 Material characterization

The morphology and surface structure of  $\text{LaMnO}_3$  and  $\text{LaMn}_{0.9}\text{Co}_{0.1}\text{O}_3$  oxides were analysed by scanning electron microscopy (LEO FESEM 1530) and transmission electron microscopy (Philips CM300). The chemical composition of synthesized oxides was determined by an EDAX analyses technique. To investigate the surface of CCBC and the design of surface nitrogen groups, x-ray photoelectron spectroscopy (Thermal scientific K-Alpha XPS spectrometer) was applied. To determine the stability of and the ratio of organic and inorganic compounds in CCBC thermogravimetric analysis (TA Instrument, Q500) was used.

#### 4.2.3 Half-cell test

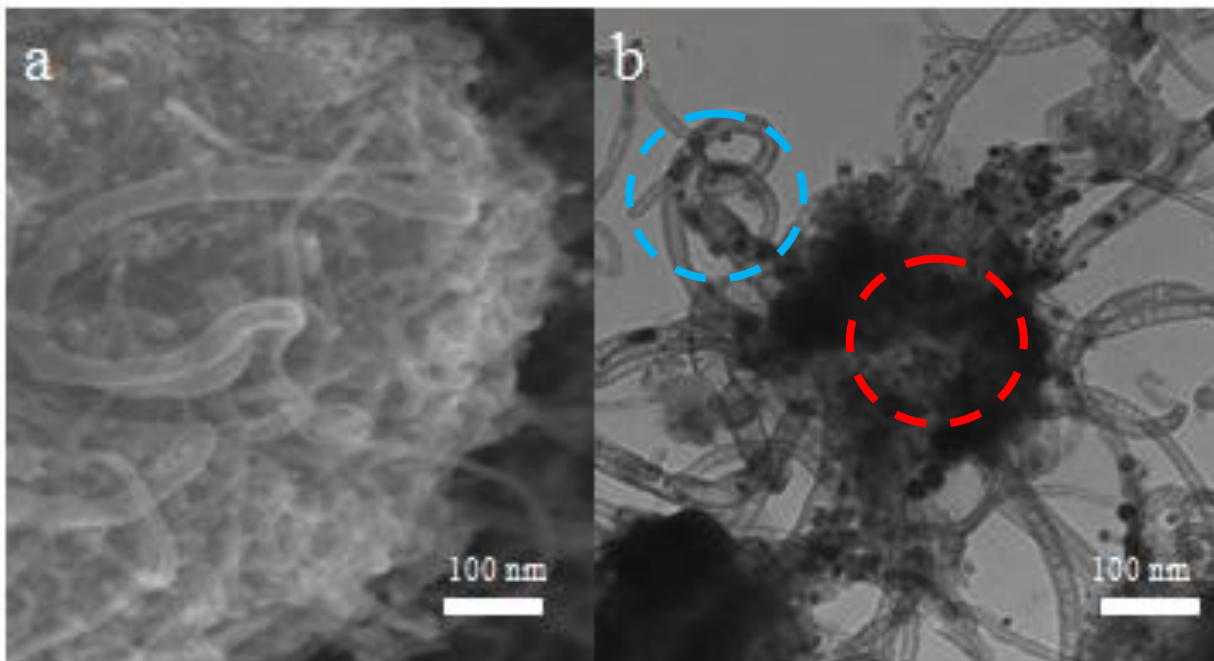
Rotating disk electrode (RDE) half cell reactions were used to evaluate the electrochemical performance of these perovskite oxides. A typical RDE setup consists of a potentiostat ( Pine Instrument Co, AFCBP - 1) and rotational speed controller ( Pine Instrument Co, AFMSRCE). RDE was used as a working electrode in these half-cell tests, which consist of a glassy carbon 5 mm OD. For this electrochemical test the catalyst must be coated on the working electrode. Thus

before the test, 4 mg of catalyst was mixed with 0.3 wt% Nafion solution. The resulting mixture or "catalyst ink" was sonicated to achieve excellent dispersion. For each test 20  $\mu\text{l}$  of ink was coated onto the working electrode, where the loading was determined to be  $0.408 \text{ mgcm}^{-2}$ . The resulting coat was inspected visually and then immersed into a 0.1 M KOH solution. The KOH solution provided the electrolytic environment. The RDE reference and counter electrodes were submerged into the KOH solution as well. Electrochemical activity towards the oxygen reduction reaction was evaluated from 0.2 V to -1 V vs Ag/AgCl. Before the ORR test the KOH electrolyte was saturated with  $\text{O}_2$ . Different rotating speeds at 100, 400, 900, and 1600 rpm were used at a scan rate of  $10 \text{ mVs}^{-1}$ . The stability of the catalysts was investigated by OER test in a voltage range 0 V to 1 V with a scan rate of  $50 \text{ mVs}^{-1}$ . Before the OER test a 900 rpm rotating speed was maintained and the electrolyte was saturated with  $\text{N}_2$ .

## **4.3 Results and Discussion**

### **4.3.1 SEM and TEM**

The morphology of  $\text{LaMn}_{0.9}\text{Co}_{0.1}\text{O}_3$  CCBC was investigated by SEM. The Figure 41 shows a lot of nanotubes which are formed around the metal oxides. The observed length of the nitrogen-doped carbon nanotubes were several hundred nanometers while the size of the perovskite oxides were found to be similar to 100 nm. Unfortunately, SEM can't give clear view of the CCBC composite due to its 3D structure. The main purpose for combining NCNT with the metal oxide is to maintain the natural high surface area of metal oxides by preventing them from agglomeration. This means that in the final composite, CCBC should be a metal oxide core surrounded by nanotubes. In this circumstance SEM was unable to clearly expose the expected porous CCBC structure.

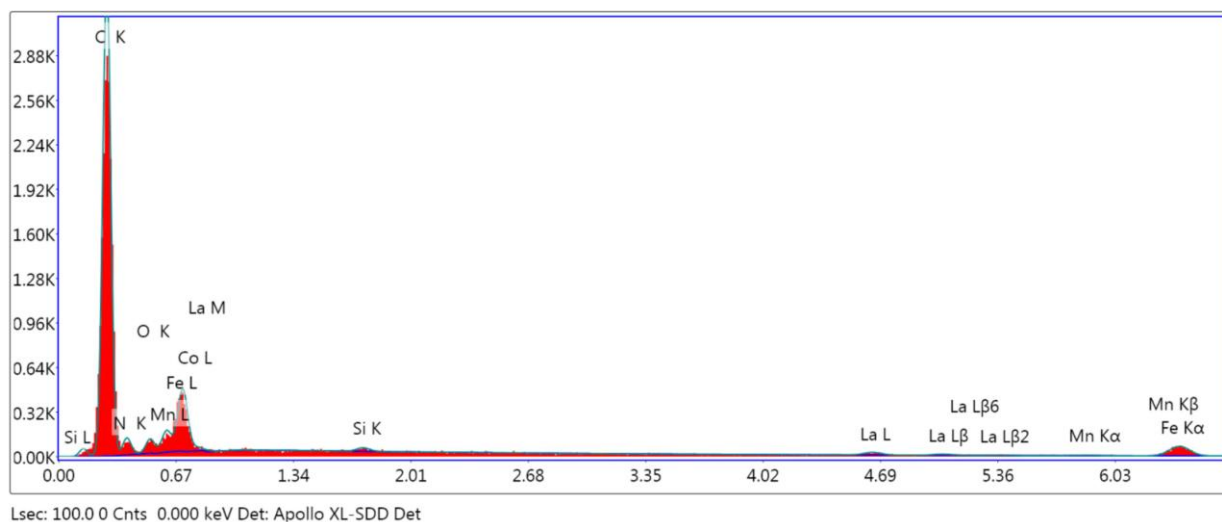


**Figure 41.** a) SEM image for CCBC, b) TEM image for CCBC

Through use of TEM to investigate CCBC it was possible to generate a clearer depiction of its internal morphology. As TEM has a more powerful beam than SEM, the TEM images are able to penetrate the surface of the sample and provide an image that is helpful for investigating the true morphology. As assumed, the metal oxide  $\text{LaMn}_{0.9}\text{Co}_{0.1}\text{O}_3$  was found to be covered with nanotubes. The size of nanoparticles was determined to be around 100-150 nm while the nanotube's size was measurable in microns. The size of the oxide nanoparticles remained the same after synthesis of CCBC, which means the NCNT helped to achieve higher surface area and prevented the oxide particles from agglomeration (81).

### 4.3.2 EDAX

The chemical composition of synthesized CCBC was analysed by using EDAX. The results are shown in Figure 42.



**Figure 42.** EDX analyses for CCBC

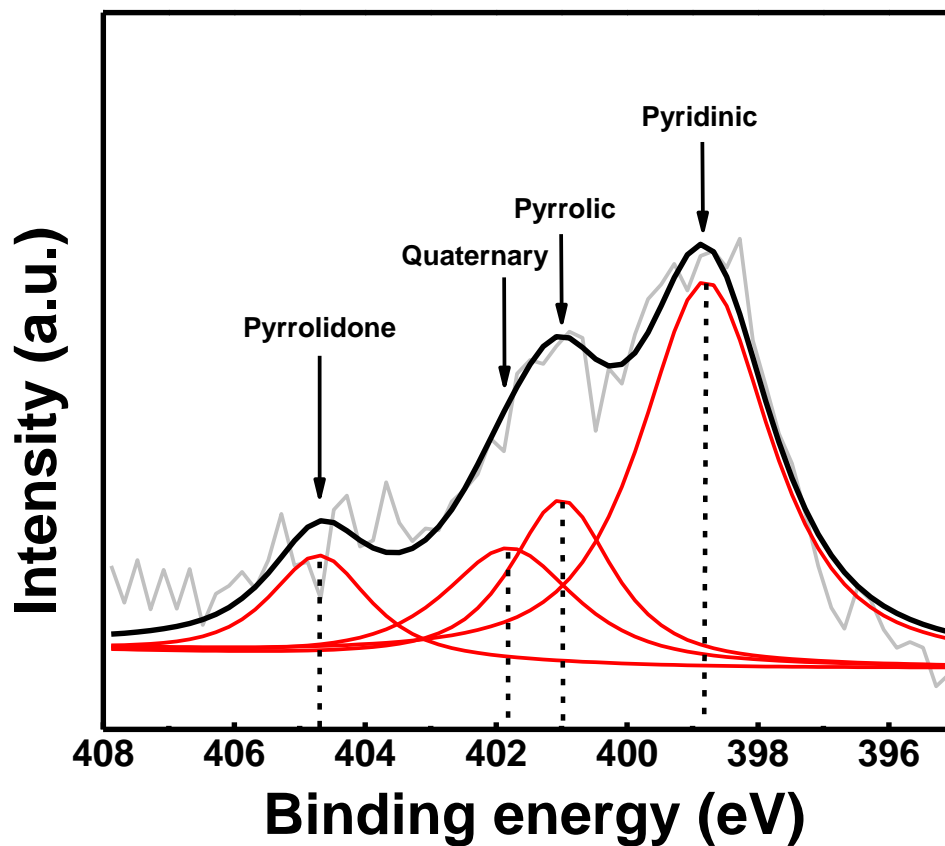
Comparing with the results for oxides, CCBC had a very sharp peak for carbon, due to the introduction of carbon nanotubes. The nanotubes which are observed in TEM are the same carbon nanotubes. Moreover, these results also showed peaks for La, Mn, Co and O due to the presence of the metal oxide when used as a precursor. During the CVD processes the use of ferrocene can be correlated with the small observed Fe peak.

### 4.3.3 X-ray photoelectron spectroscopy (XPS) analysis

X-ray photoelectron spectroscopy (XPS) analysis was done to investigate the surface compositions of CCBC and prove the doping perovskite oxide with NCNT. The results for XPS analyses shown in figure 43. Red lines which is shown in image are the peak which related to different nitrogen groups on the surface and the black line is the original signal. The results show 4 different nitrogen groups on the surface. First of all this result proves that the doping  $\text{LaMn}_{0.9}\text{Co}_{0.1}\text{O}_3$  oxide with NCNT was successful. The binding energy of different surface nitrogen groups are shown in table 2 with respective percentage.

**Table 2.** The binding energy and relative percentage of the surface nitrogen groups (92)

Surface N group	Binding energy (eV)	Relative percentage (%)
Pyridinic	398.6	49.5
Pyrrolic	400.7	21.6
Quaternary	401.5	17.1
Pyrrolidone	404.6	11.8

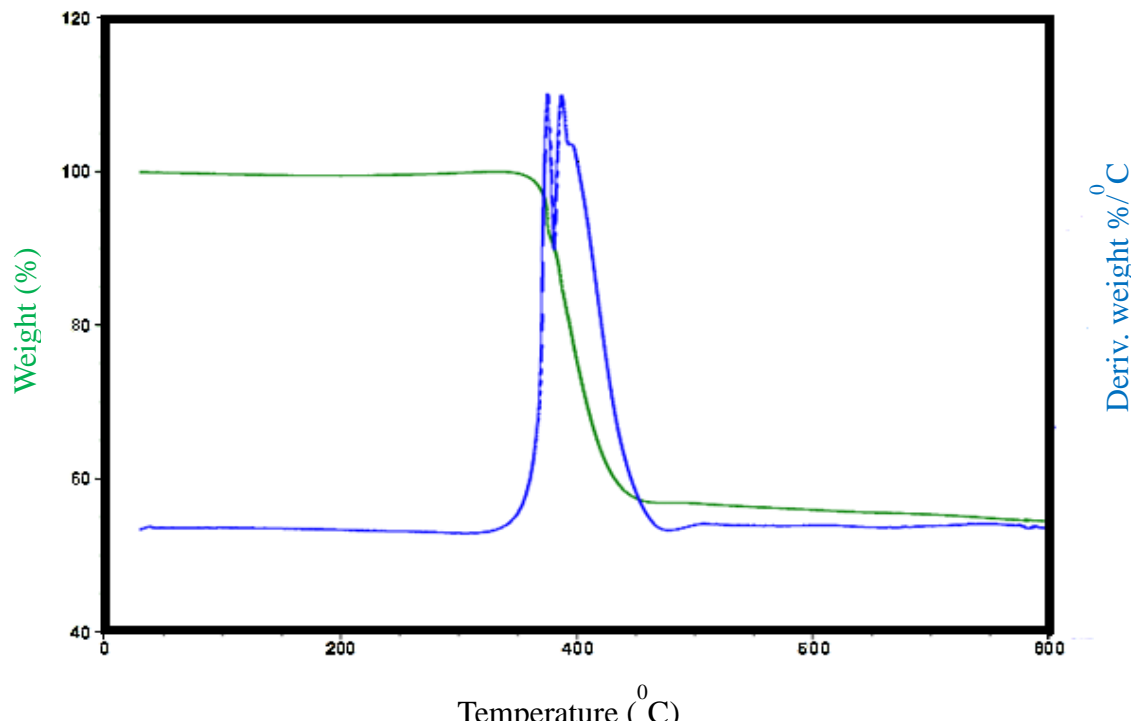


**Figure 43.** XPS analyses for nitrogen species in the CCBC



#### 4.3.4 TGA

By using thermogravimetric analyses techniques it is possible to determine the composition of an organic or inorganic chemical. The left column shows the weight given as a percentile and tracks this change over the time with increasing temperature. The result of the analysis for CCBC is shown in Figure 44. In this case NCNT is considered the organic part and  $\text{LaMn}_{0.9}\text{Co}_{0.1}\text{O}_3$  is the inorganic compound. While the temperature rose to 350 °C there was no observed change on the weight of the sample. At 350 °C the weight began to decrease and the derivative weight plot also showed the beginning of a peak at this peak. As the temperature continues increasing the derivative weight plots demonstrated a second peak. This means there were two different compounds which were oxidised and they had a similar oxidation energy. Previously it was mentioned that the inorganic part of this sample was synthesised at 850 °C by calcination in air, thus during the TGA between 350 - 450 °C there will not be any associated oxidation. However, NCNT has nitrogen and carbon which can easily be oxidised at 400 °C. In NCNT there are two types of bonds: carbon-nitrogen and carbon-carbon bond. Because of the hybrid  $\text{sp}^2$  boundary the strength of the bond between C-C ( $348 \text{ kJmol}^{-1}$ ) is stronger than C-N ( $293 \text{ kJmol}^{-1}$ ) (64)(93). On derivative weight plots this means that the first peak represents oxidation of nitrogen while the second is oxidation of carbon (94). The energy of these bonds are close to each other which is why the peaks are nearly combined.



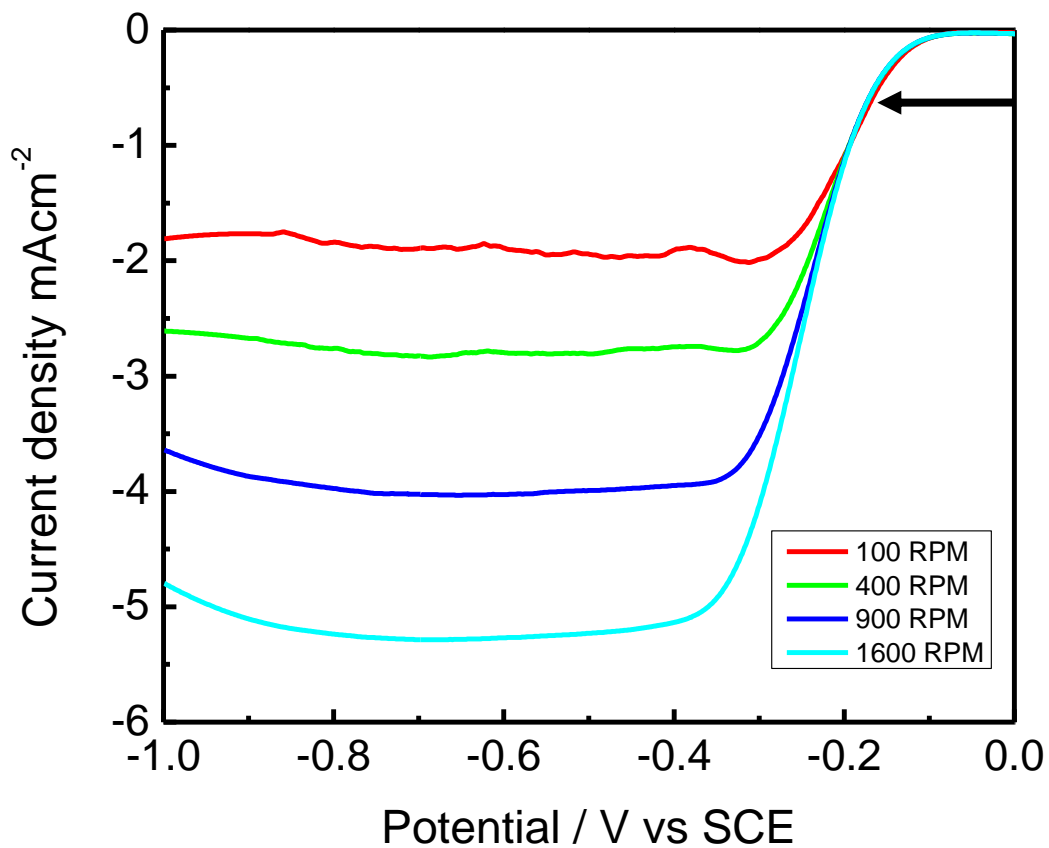
**Figure 44.** TGE analyses CCBC

### 4.3.5 Half-cell test

The electrocatalytic activity and durability of CCBC was analysed by rotating disc electrode (RDE) voltammetry using a potentiostat (CH Instrument 760D) with the test rotation speed controlled by a regulated rotor (Pine Instrument Co., AFMSRCE).

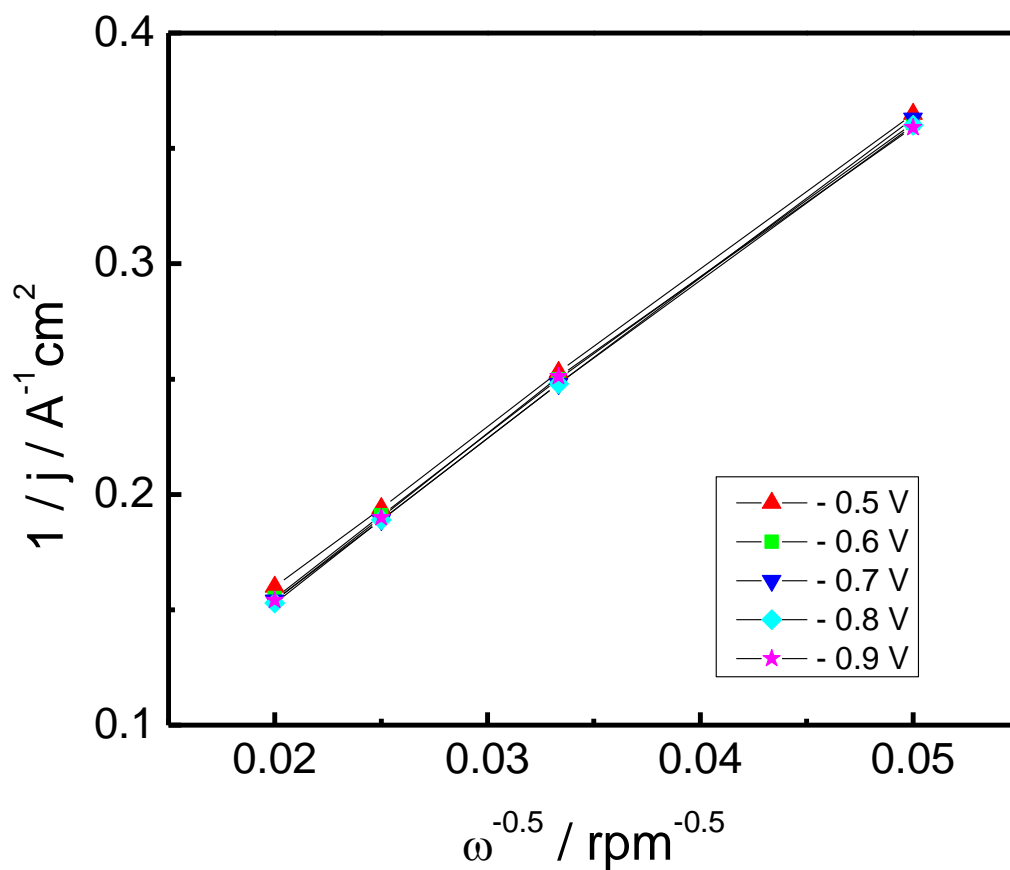
Before starting to investigate the CCBC catalyst's electrochemical performance it is important to prepare the right ink. 4 mg of CCBC powder was mixed with 0.3 w% Nafion and the solvent was sonicated for 2 hours. It is very important that after sonication catalyst was well dispersed in Nafion as the ink's dispersion will affect the coating integrity on the working electrode. 20  $\mu\text{L}$  of ink (loading at  $0.41 \text{ mgcm}^{-2}$ ) was coated on the glassy carbon surface of the working electrode. When the ink was fully dried the working electrode was immersed into the 0.1 M KOH electrolyte along with a reference and counter electrode.

The half-cell test began with activation of the catalyst by CV and thus the electrolyte was saturated with N<sub>2</sub> which pumped through the electrolyte for 30 minutes. When the cycling reaches equilibrium the test switched to LSV to record the data for back ground which will be later removed from the ORR data. After recording this background the gas was switched to O<sub>2</sub> and left for 30 minutes to both remove the N<sub>2</sub> from the electrolyte and saturate it with O<sub>2</sub>. The ORR test was performed at different rotating speeds using the LSV method. When all the data for ORR was collected the gas switched back to N<sub>2</sub> again and was left saturating for 30 minutes. At the end of this period of time the OER test was performed by using CV technique at a speed of 900 rpm. The ORR results for the performance of CCBC at 100 rpm, 400 rpm, 900 rpm and 1600 rpm is shown in Figure 45.



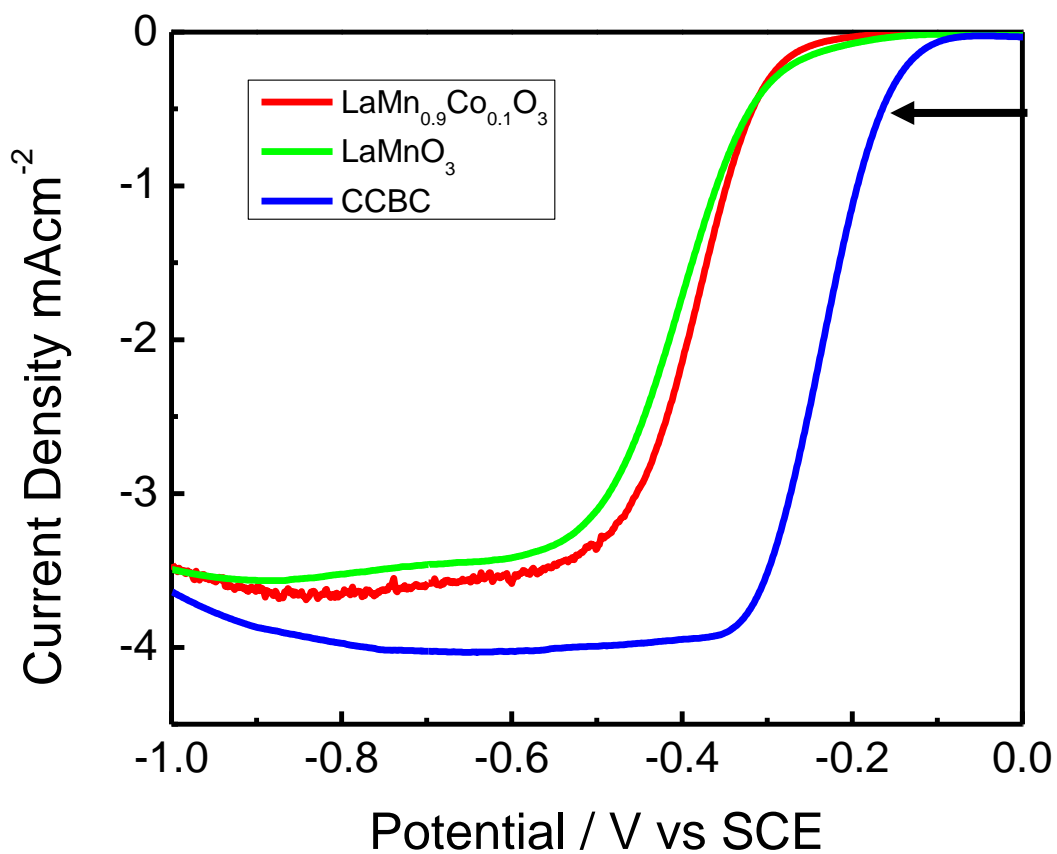
**Figure 45.** ORR performance for CCBC

Based on the ORR results at different rotating speed, KL plots were calculated as shown in figure 46. The result of the calculations shows that the number of electrons transferred were 3.9, 3.9, 4.0, 4.0 and 4.0 for -0.5, -0.6, -0.7, -0.8 and -0.9 V, respectively. The number of electron is almost matched with ideal reaction equation for oxygen reduction reaction.



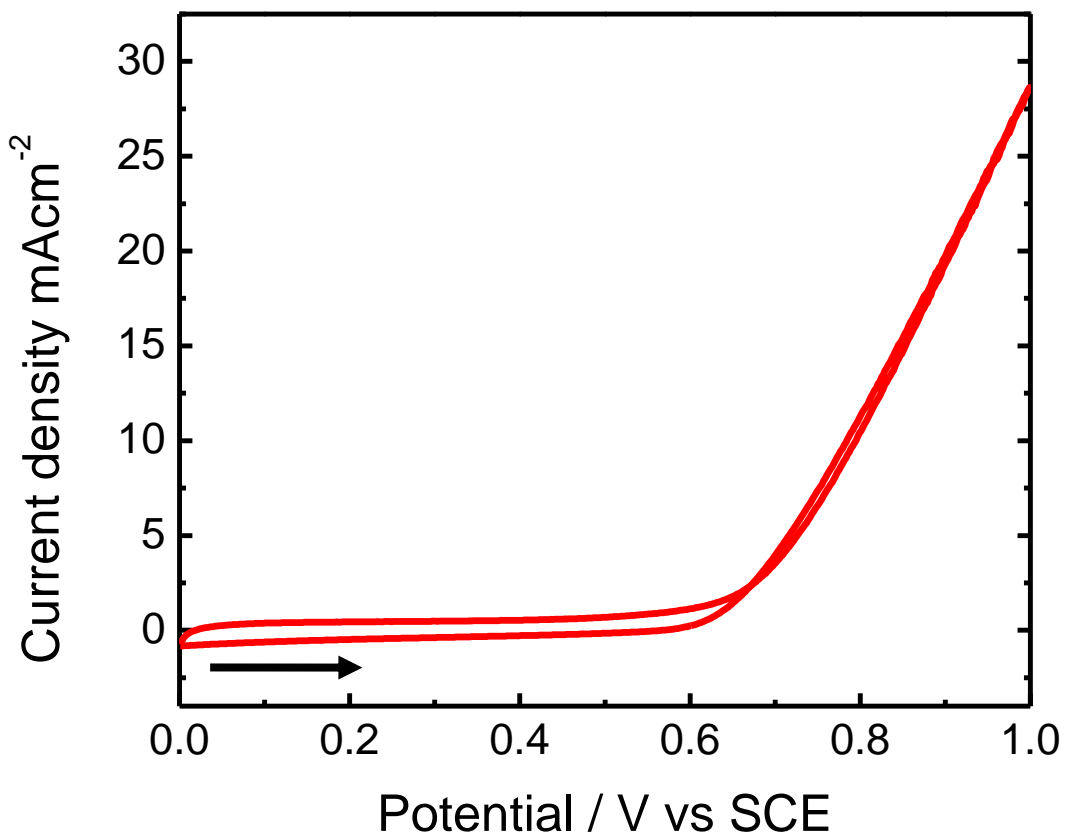
**Figure 46.** Koutecky - Levich plot for CCBC

The ORR results for  $LaMnO_3$ ,  $LaMn_{0.9}Co_{0.1}O_3$  and CCBC were compared in Figure 47 to ascertain the degree of improvement in electrochemical performance achieved during this research. The first main characterization for ORR performance is the onset potential which indicates the beginning of the electrochemical reaction. The onset potential was improved from -0.2 V (in  $LaMnO_3$  and  $LaMn_{0.9}Co_{0.1}O_3$ ) to -0.09 V (in CCBC). This means that the activation energy for the reaction onset of CCBC is more than 220% better. The second main ORR parameter is the half wave potential. After adding NCNT to  $LaMn_{0.9}Co_{0.1}O_3$  the half wave potential was improved from -0.38 V to -0.19 V.



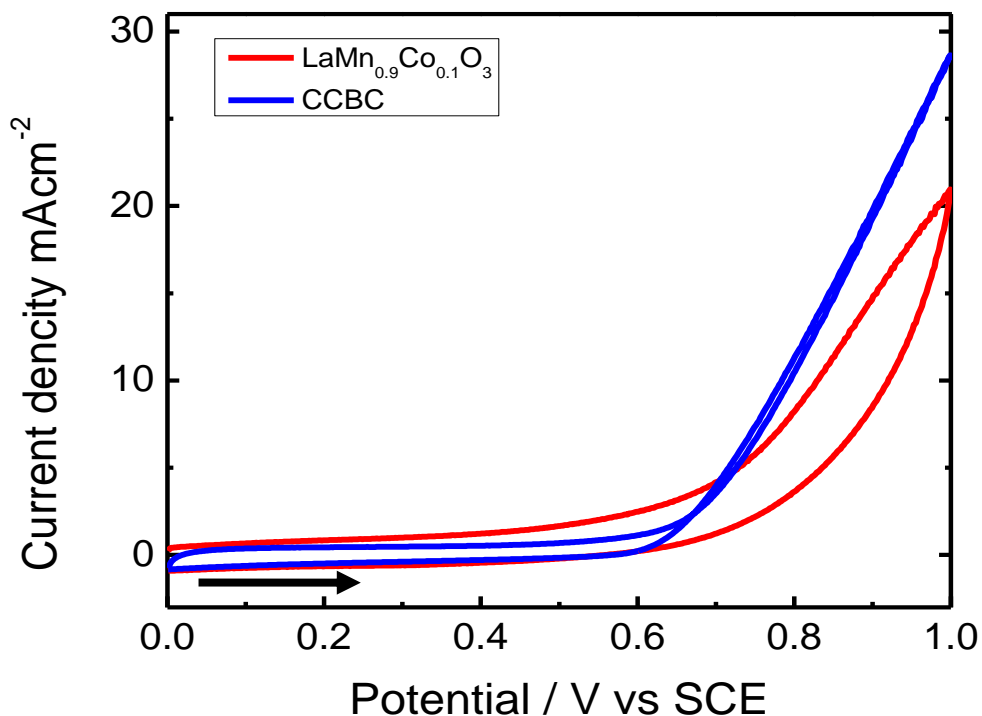
**Figure 47.** ORR performance of LaMnO<sub>3</sub> vs. LaMn<sub>0.9</sub>Co<sub>0.1</sub>O<sub>3</sub> vs. CCBC at 900 rpm

The OER test was performed by same procedure as the metal oxide catalysts were done before and shown in Figure 48. The current density of CCBC at 1.0 V was 28.5 mAcm<sup>-2</sup> which is the highest current value, compared with previous two metal oxide catalysts.



**Figure 48.** OER performance for CCBC

The OER results for  $\text{LaMnO}_3$ ,  $\text{LaMn}_{0.9}\text{Co}_{0.1}\text{O}_3$  and CCBC were compared in Figure 49 to determine the improvement in electrochemical performance achieved during this research. The results show that the capacity of CCBC is higher than both  $\text{LaMnO}_3$  and  $\text{LaMn}_{0.9}\text{Co}_{0.1}\text{O}_3$ . The density of CCBC is  $28.5 \text{ mAcm}^{-2}$  which is 132% higher than  $\text{LaMn}_{0.9}\text{Co}_{0.1}\text{O}_3$ . During the OER performance NCNT along has very high current density. However, because of the very fast degradation overall OER performance of NCNT is very poor (95). On the other hand,  $\text{LaMn}_{0.9}\text{Co}_{0.1}\text{O}_3$  has low current density during OER test and very high durability. Therefore, synthesized CCBC has very high current density and good durability



**Figure 49.** OER performance of  $\text{LaMn}_{0.9}\text{Co}_{0.1}\text{O}_3$  vs. CCBC

#### 4.4 Conclusion

In this section was described synthesis techniques for a bifunctional catalyst made of an NCNT and  $\text{LaMn}_{0.9}\text{Co}_{0.1}\text{O}_3$  composite intended for application in secondary zinc-air batteries. Through using different morphology analyses techniques it was shown that oxide particles were surrounded with NCNT while an RDE test demonstrated acceptable electrochemical performance of this novel catalyst. ORR performance showed that CCBC had a better half-wave and onset potential when compared with  $\text{LaMn}_{0.9}\text{Co}_{0.1}\text{O}_3$ . Moreover, OER test results showed that the capacity of CCBC is more than 600% as high as  $\text{LaMnO}_3$ . These results proved once again that a combination of perovskite oxide with NCNT increased electrochemical performance of the catalyst greatly.



## **5.0 Zinc Air Cell Performance**

### **5.1 Introduction**

Bifunctional catalyst is one of the main components which is needed during the making of secondary zinc-air battery. The challenge with the catalyst is one the main factors which prevent secondary zinc-air batteries from commercialization. In the previous section it has been reported that  $\text{LaMn}_{0.9}\text{Co}_{0.1}\text{O}_3$  CCBC shows good ORR and OER performance and the catalyst is stable in alkaline solution. As a bifunctional catalyst CCBC answers to all requirements for good metal-air battery. There for CCBC has been chosen as a primary catalyst for single cell battery test.

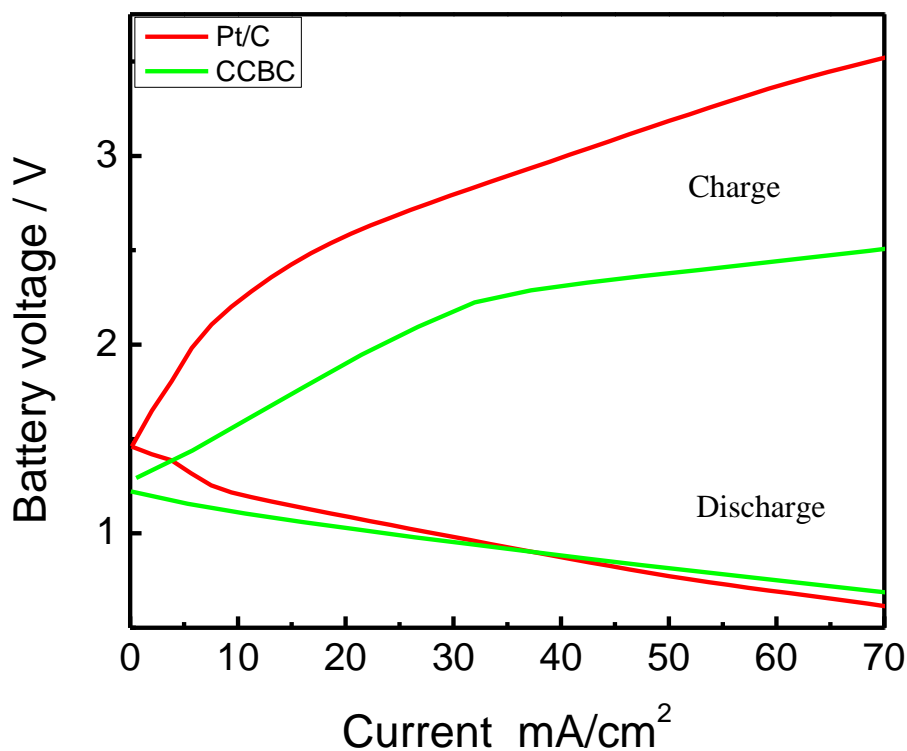
### **5.2 Preparation to Test**

Zinc-air battery test was performed using multichannel potentiostat which will help to understand the performance of the CCBC catalyst in battery. The battery design was used the same which is discussed in section 2.3.8. CCBC catalyst was coated on gas diffusion layer. Synthesis of CCBC was done in a same way as it is mentioned above where the CVD method was used to synthesis CCBC from  $\text{LaMn}_{0.9}\text{Co}_{0.1}\text{O}_3$  and CNT at  $700^\circ\text{C}$ . The synthesized powder was grinded until fine particles was formed. The ink was made from CCBC for coating on gas diffusion layer. 9.4 mg of CCBC was mixed with 1 ml isopropanol by vortex and the sonicated for half hour. After sonication 67  $\mu\text{l}$  5 wt% Nafion solution was added and sonicated for 3 hours. The final solvent after sonication was coated on GDL by spraying. All pieces of the battery were combined together and as electrolyte 6M KOH was added before starting the test.

### **5.3 Battery Performance**

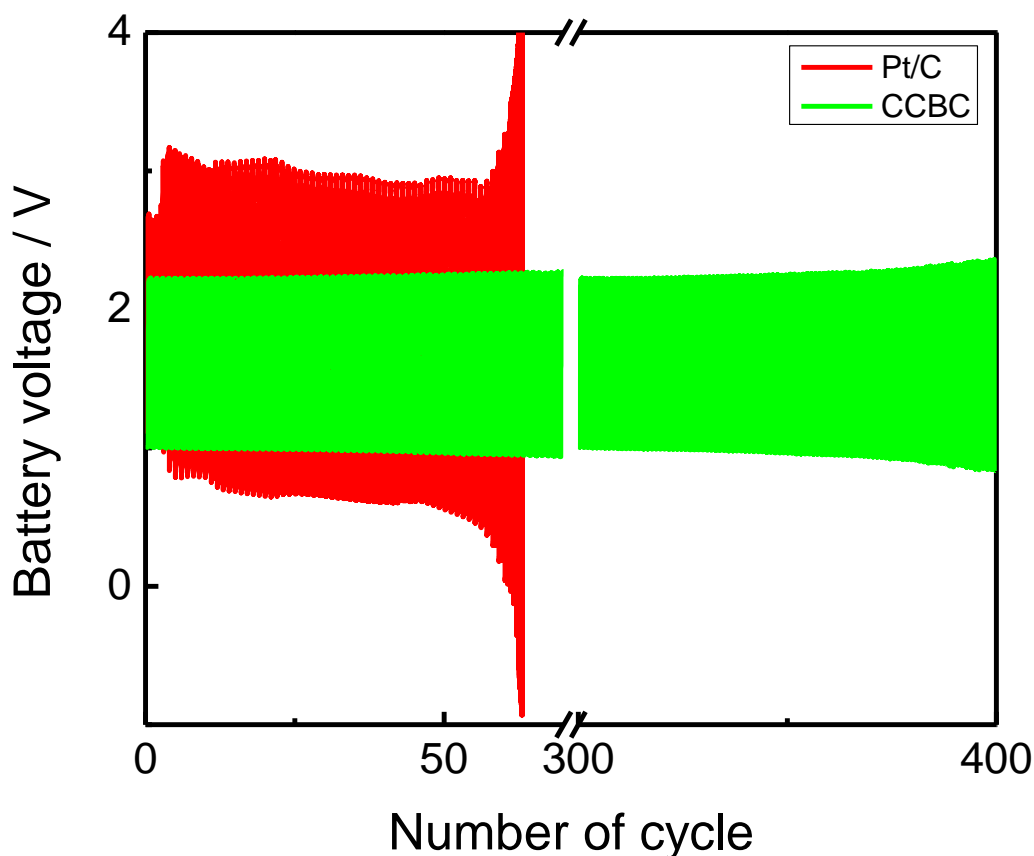
Charge/discharge rate capabilities was tested using multichannel potentiostat. Galvanodynamic test which was conducted from 0-100 mA and the voltage was recorded from the range (Figure

50). The nominal voltage of the cell is 1.65 V and based on the actual discharge/charge voltage at a specific current, one can calculate the energy efficiency by taking the ratio of the charge and discharge voltages (discharge voltage/charge voltage). A low discharge voltage means high overpotential needed for ORR and a high charge voltage means high overpotential needed for OER regarding the reactions on cathode from the cell. Both the phenomena need to be reduced to effectively improve the efficiency of the cell. From the galvanodynamic curve, it can be clearly seen that CCBC has better charge and discharge voltages in comparison with those of the Pt/C catalyst and it is more noticeable at higher current rates. This proves that CCBC has better reaction kinetics leading to higher current rate capability.



**Figure 50.** Charge/discharge rate for Pt/C vs. CCBC

The cell is cycled at constant current of  $10 \text{ mAcm}^{-2}$  at 10 min/cycle. The cell is tested for durability to see how many charge/discharge cycles it can last for until its performance degrades or the cell starts leaking from the cathode and the performances were plotted between 300 to 400 cycles in Figure 51. Like the galvanodynamic test, the comparison is made by looking at the lowest discharge voltage and highest charge voltage. For CCBC, we see a drop in efficiency from 44.64% to 35.65%. For Pt/C, we see a drop from 24.59% to 21.67% and rapidly goes to 0% after 50 cycles. Even though the drop in efficiency for CCBC after 400 cycles was lower, overall efficiency is higher. It is not practical to use Pt/C for rechargeable zinc-air cells as the efficiency is too low for it to compete with other rechargeable batteries. Therefore, CCBC makes a perfect candidate for low cost zinc-air cells with acceptable efficiency.



**Figure 51.** Durability test for Pt/C vs. CCBC

## 5.4 Conclusion

In this section, catalytic performance of CCBC was tested in a single cell zinc-air battery. The results were compared with a baseline of state-of-the-art Pt/C catalyst. Charge/discharge rates showed that lower energy was required in order to charge the battery using CCBC catalyst, compared with Pt/C. Durability tests were performed and comparisons were drawn against Pt/C. The cycling data showed how many times the battery was able to be charged and discharged while maintaining good performance. After 400 cycles the efficiency of CCBC dropped from 44.64% to 35.65%. However, Pt/C started with an initial efficiency of 24.59%, stabilizes at 21.67% but loses its efficiency very quickly after only 50 cycles. Even though the differential in efficiency for CCBC after 400 cycles was lower, the overall efficiency was maintained at a higher level. Thus CCBC was valued as a more suitable catalyst for rechargeable zinc-air battery applications than Pt/C.

## 6.0 Summary and Future Directions

In summary, electrochemical performance of perovskite type oxides as a bifunctional catalyst and possible ways of increasing catalytic performance was investigated.

First technique of increasing the catalytic performance of perovskite type oxides is doping with different metals.  $\text{LaMnO}_3$  was a perovskite type oxide and as a doping metal, cobalt was chosen. For secondary zinc-air battery it is important to synthesize highly active bifunctional catalyst which will be stable in electrolyte and strong against degradation or agglomeration during the charge and discharge processes. Moreover, the catalyst has to be cost efficient and environmentally friendly. Chosen metal oxide and Co correspond to these requirements. RDE test results show that catalytic performance of  $\text{LaMnO}_3$  was improved by doping Co in 10 wt % of Mn.

Second method, which was used, is combining  $\text{LaMn}_{0.9}\text{Co}_{0.1}\text{O}_3$  oxide with NCNT. NCNT shows very good catalytic performance during ORR reaction.  $\text{LaMn}_{0.9}\text{Co}_{0.1}\text{O}_3$  has a relatively good OER comparing to ORR. Thus, combining NCNT with  $\text{LaMn}_{0.9}\text{Co}_{0.1}\text{O}_3$  gave a better bifunctional catalyst. This is the main reason which resulted in high RDE performance in changes in surface area. Surface area is one of the main parameters of nanoparticles because, by increasing the surface area the activation energy for the reaction decreases. NCNT prevented  $\text{LaMn}_{0.9}\text{Co}_{0.1}\text{O}_3$  nanoparticles from agglomeration and the surface area was increased greatly. This is the main reason why OER performance of CCBC was higher than  $\text{LaMn}_{0.9}\text{Co}_{0.1}\text{O}_3$ .

Synthesized CCBC shows very high catalytic activity, thus, it is tested in single cell zinc-air battery. While the results were comparable with Pt/C during discharge, CCBC showed much

better charge performance and durability than Pt/C. So the CCBC developed in this study will be a promising bifunctional catalyst for rechargeable metal air battery.

### 6.1 Recommendations for Future Work

After study all experimental results with some possible aspects of future improvements was identified for CCBC.

- Doping with Co in a different Mn / Co weight ratio to find best composition;
- Use different metals than Co as doping to improve the catalytic performance;
- Develop new synthesis technique which will allow to decrease the particle size for perovskite oxides; and,
- Optimize the synthesis technique for CCBC to increase surface area.

## References

- (1) Sivakumar N, Das D, Padhy N, Senthil Kumar A, Bisoyi N. Status of pumped hydro-storage schemes and its future in India. *Renewable and Sustainable Energy Reviews* 2013;19:208-213.
- (2) Armaroli N, Balzani V. Towards an electricity-powered world. *Energy & Environmental Science* 2011;4(9):3193-3222.
- (3) Vetter J, Novak P, Wagner M, Veit C, Möller K, Besenhard J, et al. Ageing mechanisms in lithium-ion batteries. *J Power Sources* 2005;147(1):269-281.
- (4) Ji L, Lin Z, Alcoutlabi M, Zhang X. Recent developments in nanostructured anode materials for rechargeable lithium-ion batteries. *Energy & Environmental Science* 2011;4(8):2682-2699.
- (5) Fergus JW. Recent developments in cathode materials for lithium ion batteries. *J Power Sources* 2010;195(4):939-954.
- (6) Wakihara M. Recent developments in lithium ion batteries. *Materials Science and Engineering: R: Reports* 2001;33(4):109-134.
- (7) Boqiang R, Chuanwen J. A review on the economic dispatch and risk management considering wind power in the power market. *Renewable and Sustainable Energy Reviews* 2009;13(8):2169-2174.
- (8) Scolah H, Sopinka A, van Kooten GC. The economics of storage, transmission and drought: integrating variable wind power into spatially separated electricity grids. *Energy Econ* 2012;34(2):536-541.
- (9) Dunn B, Kamath H, Tarascon JM. Electrical energy storage for the grid: a battery of choices. *Science* 2011 Nov 18;334(6058):928-935.
- (10) Skyllas-Kazacos M, Chakrabarti M, Hajimolana S, Mjalli F, Saleem M. Progress in flow battery research and development. *J Electrochem Soc* 2011;158(8):R55-R79.
- (11) Armand M, Tarascon J. Building better batteries. *Nature* 2008;451(7179):652-657.
- (12) Broussely M, Planchat J, Rigobert G, Virey D, Sarre G. Lithium-ion batteries for electric vehicles: performances of 100 Ah cells. *J Power Sources* 1997;68(1):8-12.
- (13) Kennedy B, Patterson D, Camilleri S. Use of lithium-ion batteries in electric vehicles. *J Power Sources* 2000;90(2):156-162.
- (14) Nikolić Z, Živanović Z. The Contribution and Prospects of the Technical Development on Implementation of Electric and Hybrid Vehicles. 2012.

- (15) Zhu W, Poole B, Cahela D, Tatarchuk B. New structures of thin air cathodes for zinc–air batteries. *J Appl Electrochem* 2003;33(1):29-36.
- (16) Dirkse T, Kroon D. Effect of ionic strength on the passivation of zinc electrodes in KOH solutions. *J Appl Electrochem* 1971;1(4):293-296.
- (17) Sapkota P, Kim H. Zinc–air fuel cell, a potential candidate for alternative energy. *Journal of Industrial and Engineering Chemistry* 2009;15(4):445-450.
- (18) Lee J, Tai Kim S, Cao R, Choi N, Liu M, Lee KT, et al. Metal–air batteries with high energy density: Li–air versus Zn–air. *Advanced Energy Materials* 2011;1(1):34-50.
- (19) Lee J, Tai Kim S, Cao R, Choi N, Liu M, Lee KT, et al. Metal–air batteries with high energy density: Li–air versus Zn–air. *Advanced Energy Materials* 2011;1(1):34-50.
- (20) Jin C, Yang Z, Cao X, Lu F, Yang R. A novel bifunctional catalyst of  $\text{Ba}_{0.9}\text{Co}_{0.5}\text{Fe}_{0.4}\text{Nb}_{0.1}\text{O}_{3-\delta}$  perovskite for lithium–air battery. *Int J Hydrogen Energy* 2014 2/14;39(6):2526-2530.
- (21) Rodriguez JA, Fernández-García M. *Synthesis, properties, and applications of oxide nanomaterials.* : John Wiley & Sons; 2007.
- (22) Uskoković V, Drofenik M. Synthesis of materials within reverse micelles. *Surface Review and Letters* 2005;12(02):239-277.
- (23) Sanaeishoar T, Tavakkoli H, Mohave F. A facile and eco-friendly synthesis of imidazo[1,2-a]pyridines using nano-sized  $\text{LaMnO}_3$  perovskite-type oxide as an efficient catalyst under solvent-free conditions. *Applied Catalysis A: General* 2014 1/30;470(0):56-62.
- (24) Ichikawa N, Uchida S, Tranquada J, Niemöller T, Gehring P, Lee S, et al. Local magnetic order vs superconductivity in a layered cuprate. *Phys Rev Lett* 2000;85(8):1738.
- (25) Uhlenbruck S, Teipen R, Klingeler R, Büchner B, Friedt O, Hücker M, et al. Interplay between charge order, magnetism, and structure in  $\text{La}_{0.875}\text{Sr}_{0.125}\text{MnO}_3$ . *Phys Rev Lett* 1999;82(1):185.
- (26) Dabrowski B, Xiong X, Bukowski Z, Dybzinski R, Klamut P, Siewenie J, et al. Structure-properties phase diagram for  $\text{La}_{1-x}\text{Sr}_x\text{MnO}_3$  ( $0.1 < x < 0.2$ ). *Physical Review B* 1999;60(10):7006.
- (27) Yamada Y, Hino O, Nohdo S, Kanao R, Inami T, Katano S. Polaron Ordering in Low-Doping  $\text{La}_{1-x}\text{Sr}_x\text{MnO}_3$ . *Phys Rev Lett* 1996;77(5):904.
- (28) Inami T, Ikeda N, Murakami Y, Koyama I, Wakabayashi Y, Yamada Y. Charge Ordering in  $\text{La}_{1-x}\text{Sr}_x\text{MnO}_3$  ( $x = 0.12$ ). *Japanese Journal of Applied Physics Supplement* 1999;38:212-214.



- (29) Yamada Y, Suzuki J, Oikawa K, Katano S, Fernandez-Baca J. Neutron diffraction of hole polaron ordering in  $\text{La}_{1-x}\text{Sr}_x\text{MnO}_3$  ( $x \approx 1/8$ ). *Physical Review B* 2000;62(17):11600.
- (30) Endoh Y, Hirota K, Ishihara S, Okamoto S, Murakami Y, Nishizawa A, et al. Transition between two ferromagnetic states driven by orbital ordering in  $\text{La}_{0.88}\text{Sr}_{0.12}\text{MnO}_3$ . *Phys Rev Lett* 1999;82(21):4328.
- (31) Mizokawa T, Khomskii D, Sawatzky G. Charge and orbital ordering in underdoped  $\text{La}_{1-x}\text{Sr}_x\text{MnO}_3$ . *Physical Review B* 2000;61(6):R3776.
- (32) Korotin M, Fujiwara T, Anisimov V. Long-period orbital order with hole stripes in  $\text{La}_{7/8}\text{Sr}_{1/8}\text{MnO}_3$ . *Physical Review B* 2000;62(9):5696.
- (33) Ayyub P, Palkar V, Chattopadhyay S, Multani M. Effect of crystal size reduction on lattice symmetry and cooperative properties. *Physical Review B* 1995;51(9):6135.
- (34) McHale J, Auroux A, Perrotta A, Navrotsky A. Surface energies and thermodynamic phase stability in nanocrystalline aluminas. *Science* 1997;277(5327):788-791.
- (35) Banfield J. Thermodynamic analysis of phase stability of nanocrystalline titania. *Journal of Materials Chemistry* 1998;8(9):2073-2076.
- (36) Samsonov V, Sdobnyakov NY, Bazulev A. On thermodynamic stability conditions for nanosized particles. *Surf Sci* 2003;532:526-530.
- (37) Moriarty P. Nanostructured materials. *Reports on Progress in Physics* 2001;64(3):297.
- (38) Rodriguez JA, Maiti A. Adsorption and decomposition of  $\text{H}_2\text{S}$  on  $\text{MgO}$  (100),  $\text{NiMgO}$  (100), and  $\text{ZnO}$  (0001) surfaces: a first-principles density functional study. *The Journal of Physical Chemistry B* 2000;104(15):3630-3638.
- (39) Bredow T, Apra E, Catti M, Pacchioni G. Cluster and periodic ab-initio calculations on  $\text{K/TiO}_2(110)$ . *Surf Sci* 1998;418(1):150-165.
- (40) Casarin M, Maccato C, Vittadini A. An LCAO-LDF study of the chemisorption of  $\text{H}_2\text{O}$  and  $\text{H}_2\text{S}$  on  $\text{ZnO}$  (0001) and  $\text{ZnO}$  (1010). *Surf Sci* 1997;377:587-591.
- (41) Rodriguez JA. Orbital-band interactions and the reactivity of molecules on oxide surfaces: from explanations to predictions. *Theoretical Chemistry Accounts* 2002;107(3):117-129.
- (42) Rodriguez JA, Chaturvedi S, Kuhn M, Hrbek J. Reaction of  $\text{H}_2\text{S}$  and  $\text{S}_2$  with metal/oxide surfaces: Band-gap size and chemical reactivity. *The Journal of Physical Chemistry B* 1998;102(28):5511-5519.
- (43) Kelly G, King F, Kett M. Waste elimination in condensation reactions of industrial importance. *Green Chem* 2002;4(4):392-399.

- (44) Valkenberg M, DeCastro C, Hölderich W. Friedel-Crafts acylation of aromatics catalysed by supported ionic liquids. *Applied Catalysis A: General* 2001;215(1):185-190.
- (45) Bahr JL, Yang J, Kosynkin DV, Bronikowski MJ, Smalley RE, Tour JM. Functionalization of carbon nanotubes by electrochemical reduction of aryl diazonium salts: a bucky paper electrode. *J Am Chem Soc* 2001;123(27):6536-6542.
- (46) Yu M, Lourie O, Dyer MJ, Moloni K, Kelly TF, Ruoff RS. Strength and breaking mechanism of multiwalled carbon nanotubes under tensile load. *Science* 2000;287(5453):637-640.
- (47) Zheng M, Huang X. Nanoparticles comprising a mixed monolayer for specific bindings with biomolecules. *J Am Chem Soc* 2004;126(38):12047-12054.
- (48) Hong S, Myung S. Nanotube Electronics: A flexible approach to mobility. *Nature Nanotechnology* 2007;2(4):207-208.
- (49) Ogata S, Shibutani Y. Ideal tensile strength and band gap of single-walled carbon nanotubes. *Physical Review B* 2003;68(16):165409.
- (50) Jana D, Sun C, Chen L, Chen K. Effect of chemical doping of boron and nitrogen on the electronic, optical, and electrochemical properties of carbon nanotubes. *Progress in Materials Science* 2013 6;58(5):565-635.
- (51) Liu H, Song C, Tang Y, Zhang J, Zhang J. High-surface-area CoTMPP/C synthesized by ultrasonic spray pyrolysis for PEM fuel cell electrocatalysts. *Electrochim Acta* 2007;52(13):4532-4538.
- (52) Lee K, Zhang L, Lui H, Hui R, Shi Z, Zhang J. Oxygen reduction reaction (ORR) catalyzed by carbon-supported cobalt polypyrrole (Co-PPy/C) electrocatalysts. *Electrochim Acta* 2009;54(20):4704-4711.
- (53) Qu L, Liu Y, Baek J, Dai L. Nitrogen-doped graphene as efficient metal-free electrocatalyst for oxygen reduction in fuel cells. *ACS nano* 2010;4(3):1321-1326.
- (54) Li J, Vergne MJ, Mowles ED, Zhong W, Hercules DM, Lukehart CM. Surface functionalization and characterization of graphitic carbon nanofibers (GCNFs). *Carbon* 2005;43(14):2883-2893.
- (55) Konyushenko EN, Stejskal J, Trchová M, Hradil J, Kovářová J, Prokeš J, et al. Multi-wall carbon nanotubes coated with polyaniline. *Polymer* 2006;47(16):5715-5723.
- (56) Ramanathan T, Fisher F, Ruoff R, Brinson L. Amino-functionalized carbon nanotubes for binding to polymers and biological systems. *Chemistry of Materials* 2005;17(6):1290-1295.

- (57) Terrones M, Redlich P, Grobert N, Trasobares S, Hsu W, Terrones H, et al. Carbon nitride nanocomposites: Formation of aligned C<sub>x</sub>N<sub>y</sub> nanofibers. *Adv Mater* 1999;11(8):655-658.
- (58) Choi HC, Park J, Kim B. Distribution and structure of N atoms in multiwalled carbon nanotubes using variable-energy X-ray photoelectron spectroscopy. *The Journal of Physical Chemistry B* 2005;109(10):4333-4340.
- (59) Lee YT, Kim NS, Park J, Han JB, Choi YS, Ryu H, et al. Temperature-dependent growth of carbon nanotubes by pyrolysis of ferrocene and acetylene in the range between 700 and 1000 C. *Chemical physics letters* 2003;372(5):853-859.
- (60) Terrones M, Benito A, Manteca-Diego C, Hsu W, Osman O, Hare J, et al. Pyrolytically grown B<sub>x</sub>C<sub>y</sub>N<sub>z</sub> nanomaterials: nanofibres and nanotubes. *Chemical physics letters* 1996;257(5):576-582.
- (61) Hellgren N, Johansson MP, Broitman E, Hultman L, Sundgren J. Role of nitrogen in the formation of hard and elastic CN<sub>x</sub> thin films by reactive magnetron sputtering. *Physical Review B* 1999;59(7):5162.
- (62) Rodil S, Milne W, Robertson J, Brown L. Maximized  $sp^3$  bonding in carbon nitride phases. *Appl Phys Lett* 2000;77(10):1458-1460.
- (63) Bao J, Kishi N, Khatri I, Soga T. Nitrogen-doped carbon nanotubes synthesized on metal substrates from a single precursor. *Mater Lett* 2013 12/15;113(0):114-117.
- (64) Somanathan T, Pandurangan A. Multiwalled carbon nanotubes synthesis with high yield utilizing Pt/Al-MCM-41 via catalytic chemical vapour deposition technique. *Journal of Porous Materials* 2009;16(4):459-464.
- (65) Chizari K, Vena A, Laurentius L, Sundararaj U. The effect of temperature on the morphology and chemical surface properties of nitrogen-doped carbon nanotubes. *Carbon* 2014 3;68(0):369-379.
- (66) Seiler H. Secondary electron emission in the scanning electron microscope. *J Appl Phys* 1983;54(11):R1-R18.
- (67) Wischnitzer S. *Introduction to electron microscopy*. : Pergamon Press; 1981.
- (68) Kim B. *Non-Precious Cathode Electrocatalytic Materials for Zinc-Air Battery*. 2013.
- (69) Saito Y, Yoshikawa T, Bandow S, Tomita M, Hayashi T. Interlayer spacings in carbon nanotubes. *Physical Review B* 1993;48:1907-1909.
- (70) Hollander JM, Jolly WL. X-ray photoelectron spectroscopy. *Acc Chem Res* 1970;3(6):193-200.

- (71) Kim B. Non-Precious Cathode Electrocatalytic Materials for Zinc-Air Battery. 2013.
- (72) Reimer L, Kohl H. Transmission electron microscopy: physics of image formation. : Springer; 2008.
- (73) Chen Z. Nitrogen-Doped Carbon Materials as Oxygen Reduction Reaction Catalysts for Metal-Air Fuel Cells and Batteries. 2012.
- (74) Seiler H. Secondary electron emission in the scanning electron microscope. J Appl Phys 1983;54(11):R1-R18.
- (75) Matter PH, Zhang L, Ozkan US. The role of nanostructure in nitrogen-containing carbon catalysts for the oxygen reduction reaction. Journal of Catalysis 2006;239(1):83-96.
- (76) Wu J, Park HW, Yu A, Higgins D, Chen Z. Facile Synthesis and Evaluation of Nanofibrous Iron–Carbon Based Non-Precious Oxygen Reduction Reaction Catalysts for Li–O<sub>2</sub> Battery Applications. The Journal of Physical Chemistry C 2012;116(17):9427-9432.
- (77) Park HW, Lee DU, Liu Y, Wu J, Nazar LF, Chen Z. Bi-Functional N-Doped CNT/Graphene Composite as Highly Active and Durable Electrocatalyst for Metal Air Battery Applications. J Electrochem Soc 2013;160(11):A2244-A2250.
- (78) Yu T, Kim DY, Zhang H, Xia Y. Platinum Concave Nanocubes with High-Index Facets and Their Enhanced Activity for Oxygen Reduction Reaction. Angewandte Chemie International Edition 2011;50(12):2773-2777.
- (79) Lu Y, Xu Z, Gasteiger HA, Chen S, Hamad-Schifferli K, Shao-Horn Y. Platinum– gold nanoparticles: A highly active bifunctional electrocatalyst for rechargeable lithium– air batteries. J Am Chem Soc 2010;132(35):12170-12171.
- (80) Lim B, Jiang M, Camargo PH, Cho EC, Tao J, Lu X, et al. Pd-Pt bimetallic nanodendrites with high activity for oxygen reduction. Science 2009 Jun 5;324(5932):1302-1305.
- (81) Chen Z, Yu A, Higgins D, Li H, Wang H, Chen Z. Highly Active and Durable Core–Corona Structured Bifunctional Catalyst for Rechargeable Metal–Air Battery Application. Nano letters 2012;12(4):1946-1952.
- (82) Blum LC, van Deursen R, Reymond J. Visualisation and subsets of the chemical universe database GDB-13 for virtual screening. J Comput Aided Mol Des 2011;25(7):637-647.
- (83) Suntivich J, May KJ, Gasteiger HA, Goodenough JB, Shao-Horn Y. A perovskite oxide optimized for oxygen evolution catalysis from molecular orbital principles. Science 2011 Dec 9;334(6061):1383-1385.

- (84) Yang W, Salim J, Li S, Sun C, Chen L, Goodenough JB, et al. Perovskite Sr<sub>0.95</sub>Ce<sub>0.05</sub>CoO<sub>3-δ</sub> loaded with copper nanoparticles as a bifunctional catalyst for lithium-air batteries. *Journal of Materials Chemistry* 2012;22(36):18902-18907.
- (85) Dandia A, Parewa V, Gupta SL, Rathore KS. Cobalt doped ZnS nanoparticles as a recyclable catalyst for solvent-free synthesis of heterocyclic privileged medicinal scaffolds under infrared irradiation. *Journal of Molecular Catalysis A: Chemical* 2013 7;373(0):61-71.
- (86) Ungváry F. Application of transition metals in hydroformylation: Annual survey covering the year 2006. *Coord Chem Rev* 2007;251(15):2087-2102.
- (87) Safari J, Banitaba SH, DEHGHAN KHALILI S. Cobalt Nanoparticles Promoted Highly Efficient One Pot Four-Component Synthesis of 1, 4-Dihydropyridines under Solvent-Free Conditions. *Chinese journal of catalysis* 2011;32(11):1850-1855.
- (88) He W, Zhang Y, Liang Q, Jiang W, Sun H. Hydrothermal synthesis and characterization of nano-petal nickel hydroxide. *Rare Metals* :1-6.
- (89) Matter PH, Wang E, Arias M, Biddinger EJ, Ozkan US. Oxygen reduction reaction catalysts prepared from acetonitrile pyrolysis over alumina-supported metal particles. *The Journal of Physical Chemistry B* 2006;110(37):18374-18384.
- (90) Maldonado S, Stevenson KJ. Direct preparation of carbon nanofiber electrodes via pyrolysis of iron (II) phthalocyanine: electrocatalytic aspects for oxygen reduction. *The Journal of Physical Chemistry B* 2004;108(31):11375-11383.
- (91) Chen Z, Choi J, Wang H, Li H, Chen Z. Highly durable and active non-precious air cathode catalyst for zinc air battery. *J Power Sources* 2011;196(7):3673-3677.
- (92) Kundu S, Xia W, Busser W, Becker M, Schmidt DA, Havenith M, et al. The formation of nitrogen-containing functional groups on carbon nanotube surfaces: a quantitative XPS and TPD study. *Physical Chemistry Chemical Physics* 2010;12(17):4351-4359.
- (93) Scaccia S, Carewska M, Prosini PP. Study of purification process of single-walled carbon nanotubes by thermoanalytical techniques. *Thermochimica acta* 2005;435(2):209-212.
- (94) Chen C, Dai Y, Huang JG, Jehng J. Intermetallic catalyst for carbon nanotubes (CNTs) growth by thermal chemical vapor deposition method. *Carbon* 2006;44(9):1808-1820.
- (95) Chen Z, Yu A, Ahmed R, Wang H, Li H, Chen Z. Manganese dioxide nanotube and nitrogen-doped carbon nanotube based composite bifunctional catalyst for rechargeable zinc-air battery. *Electrochim Acta* 2012 5/1;69(0):295-300.